A MULTISCALE FRAMEWORK FOR SIMULATING LARGE-CURVATURE BENDING RESPONSE OF THIN FIBRE COMPOSITE STRUCTURES WITH INCREMENTAL SHELL STIFFNESS UPDATING

K. G. N. S. S. SILVA

248065F

Master of Science (Major Component Research)

Department of Civil Engineering
Faculty of Engineering

University of Moratuwa
Sri Lanka

January 2026

A MULTISCALE FRAMEWORK FOR SIMULATING LARGE-CURVATURE BENDING RESPONSE OF THIN FIBRE COMPOSITE STRUCTURES WITH INCREMENTAL SHELL STIFFNESS UPDATING

K. G. N. S. S. SILVA

248065F

Master of Science (Major Component Research)

Department of Civil Engineering

Faculty of Engineering

University of Moratuwa

Sri Lanka

January 2026

DECLARATION

I declare that this is my own work and this thesis/dissertation does not incorporate without acknowledgement any material previously submitted for a degree or diploma in any other University or Institute of higher learning and to the best of my knowledge and belief it does not contain any material previously published or written by another person except where the acknowledgement is made in the text. I retain the right to use this content in whole or part in future works (such as articles or books).

Signature: Date: 18/01/2026

The above candidate has carried out research for the ~~PhD/MPhil/~~Masters thesis/dissertation under my supervision. I confirm that the declaration made above by the student is true and correct.

Name of Supervisor: Prof. Chinthaka Mallikarachchi

Signature of the Supervisor: Date: 21/01/2026

Name of Supervisor: Dr. Sumudu Herath

Signature of the Supervisor: Date: 21/01/2026

DEDICATION

To every young researcher who stays up late, driven by wonder and hope, in search of the truths the world has yet to see…

ACKNOWLEDGEMENT

First and foremost, I would like to express my heartfelt gratitude to my research supervisors, Prof. Chinthaka Mallikarachchi and Dr. Sumudu Herath, for giving me the invaluable opportunity to carry out this research under their guidance. Their unwavering support, encouragement, and insightful mentorship were instrumental in shaping the direction and quality of this work. I am truly fortunate to have had such inspiring advisors.

I also extend my sincere thanks to Prof. Priyan Dias for his thought-provoking feedback during the progress reviews, which challenged me to think beyond conventional boundaries and approach problems with a broader perspective.

I am deeply appreciative of the support and constructive feedback provided by Lasantha Weerasekara and Chamika Wanasinghe, whose thoughtful discussions and critical insights contributed significantly to this study.

My appreciation also goes to the academic staff of the Department of Civil Engineering, University of Moratuwa, for their continuous support and for providing a stimulating research environment.

Further, I am profoundly grateful to my family and friends for being a constant source of strength, inspiration, and moral support throughout this journey.

Lastly, I would like to thank Indo-Sri Lankan Joint Research Project (Grant no. MSVRI/RES/03/07-08/2021) for the financial support provided through-out the research project.

ABSTRACT

The nonlinear bending stiffness of thin carbon-fibre woven composites is critical in the design of deployable space structures, yet it is not represented in conventional analytical or numerical design frameworks. Although this nonlinear bending response has been experimentally observed and characterised, a generalised modelling strategy that can systematically incorporate it into structural-scale simulations remains limited. This thesis proposes a multi-scale numerical framework, supported by user-defined subroutines, to embed bending stiffness nonlinearity into finite element models and to predict the response of thin woven composite structures undergoing large deformations. At the meso-scale, the curvature-dependent bending stiffness was extracted from a previously developed and experimentally validated in-house representative unit-cell model, incorporating material plasticity and progressive damage. Building on this input, a macro-scale modelling approach was developed in this thesis using a UGENS user-defined subroutine to embed the curvature-dependent stiffness into structural simulations. The framework was applied to flat coupons and singly curved configurations, including tape springs, to assess the influence of bending stiffness degradation on global structural behaviour. Numerical predictions were validated against analytical solutions and experimental results reported in the literature. The proposed approach accurately reproduced the nonlinear bending moment response and the global deformation behaviour of both flat and curved structures, including complex response features such as bifurcations. Overall, the thesis demonstrates a practical and reliable modelling route for incorporating bending stiffness degradation in thin woven composite structures, enabling improved analysis and design of advanced space structures.

Keywords: Multiscale modelling, nonlinear bending response, stiffness reduction, subroutines, tape-springs, woven composites

TABLE OF CONTENTS

LIST OF FIGURES

LIST OF TABLES

LIST OF ABBREVIATIONS

Abbreviation	Description
CBT	Column Bending Test
DoF	Degree of Freedom
EE	Embedded Element
FEA	Finite Element Analysis
FEM	Finite Element Modelling
GPR	Gaussian Process Regression
RP	Reference Point
RUC	Representative Unit Cell
RVE	Representative Volume Element
UD	Uni-Directional
UGENS	User-Defined General Section
UMAT	User-Defined Material
USDFLD	User Defined Field
XRCT	X-ray Computed Tomography

LIST OF APPENDICES

CHAPTER 1

1. INTRODUCTION

Modelling and understanding the nonlinear behaviour of composites remains challenging because their response is governed by interacting mechanisms across multiple length scales. Composites are anisotropic and heterogeneous, and their behaviour depends on fibre architecture, matrix and interface properties, and manufacturing variability. Under loading, several nonlinear and damage processes can occur simultaneously, such as matrix plasticity/cracking, fibre-matrix debonding, delamination, and fibre kinking, often in a progressive and history-dependent manner. This makes the global response highly sensitive to loading path and difficult to capture with a single constitutive model. Since structural integrity is critical in industries such as aerospace, reliable models of composite nonlinearity are essential for accurate prediction and safe, efficient design.

1.1. Role of Carbon-fibre Composites in Aerospace Structures

Thin woven fibre composites are well suited to morphing aerospace structures because their high in-plane stiffness and strength can be achieved alongside relatively low bending stiffness, enabling large, reversible deformations while still carrying operational loads [1]. Many morphing and deployable concepts rely on elastic strain energy stored during packaging to transition from one stable equilibrium shape to another and self-deploy into the required operational configuration [2]. The woven architecture can store and release this elastic strain energy during snap-through between stable configurations, while the stiffness response can be tailored through fibre orientation and lay-up, making woven carbon-fibre composites particularly beneficial. Deployable reflectors [3] (see Fig. 1.1), booms [4], energy harvesting systems [5] and solar sails [6] (see Fig. 1.2) are examples of such applications in the aerospace industry.

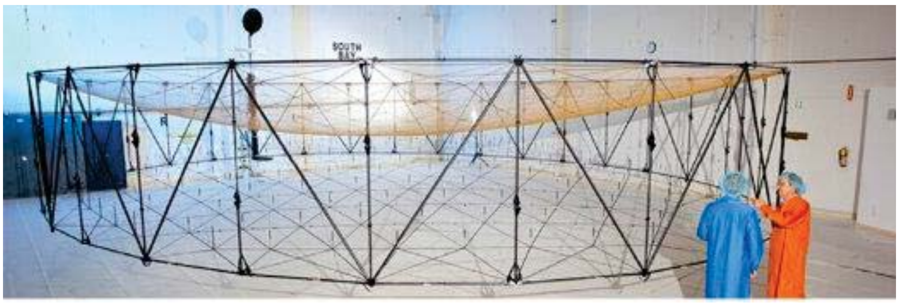

Fig. 1.1: Astro-Mesh Ò mesh reflector. Adapted from [3]

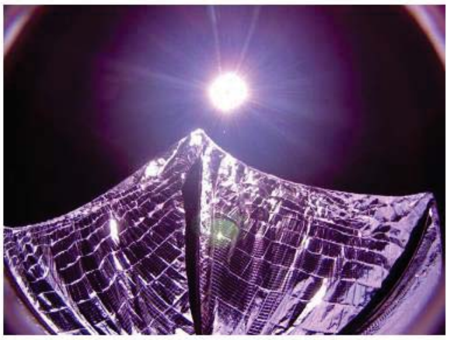

Fig. 1.3: LightSail 2 sail deployment image. Adapted from [6]

These aerospace structures are often large in their deployed state and cannot be launched at full scale. Therefore, they must be compactly stowed within the limited volume available in the launch vehicle (see Fig. 1.3) [7]. To improve the adaptivity and packaging efficiency of fibre composite structures, various methodologies have been explored, including origami- and kirigami-inspired packaging mechanisms (see Fig. 1.4) [8].

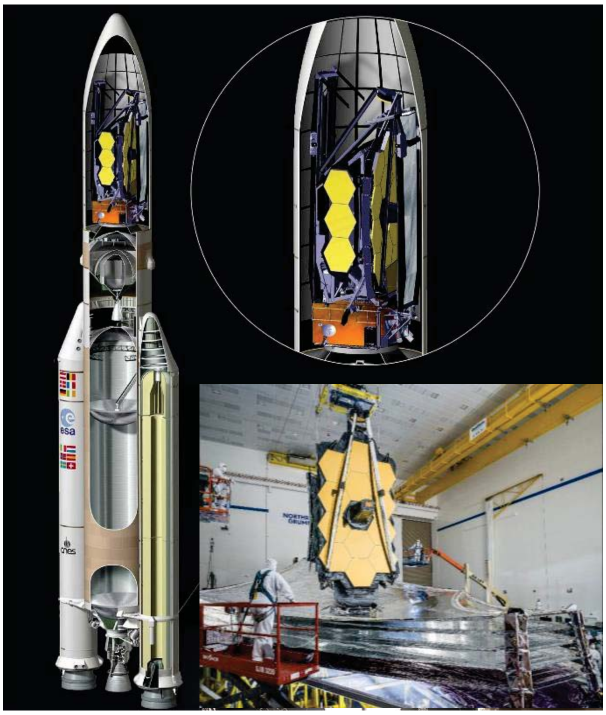

Fig. 1.2: Packaging of James Webb Space Telescope. Adapted from [7]

During stowage and deployment, thin composite structures experience significant strains and curvatures (see Fig. 1.5). Since the maximum strain or curvature the material can withstand ultimately limits packaging efficiency, it is essential to understand the structural mechanics of thin composite materials up to failure. Accordingly, recent studies have focused on improving the material performance and functionality of composite structures to enable novel, more efficient aerospace systems.

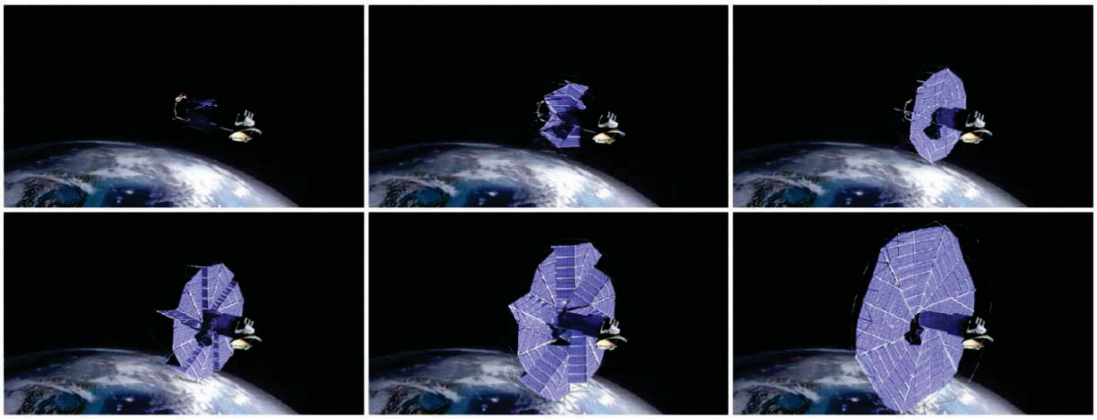

Fig. 1.4: Origami inspired deployment mechanism. Adapted from [8]

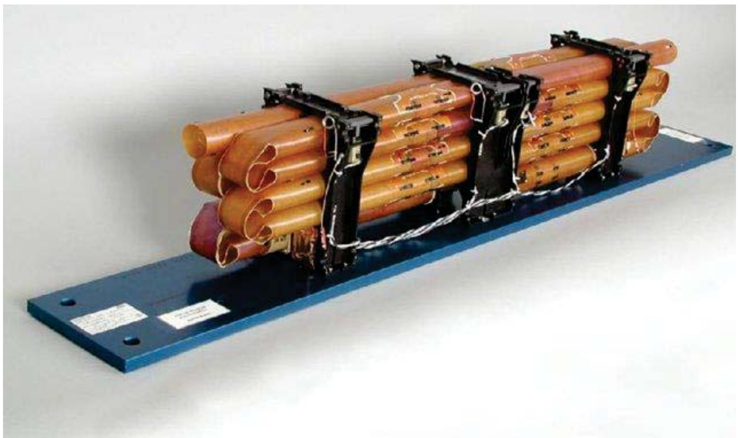

Fig. 1.5: Flattenable foldable tubes with large curvatures used on MARSIS

1.2. Non-linear Behaviour of Carbon-fibre Composites

Experimental studies have been conducted focusing on the mechanical properties of composites under tensile forces (see Fig. 1.6 and Fig. 1.7) [9], [10] and flexural forces (see Fig. 1.8) [11]. These experimental results show that in-plane and out-of-the plane material properties of thin-walled composites exhibit initially elastic behaviour but become nonlinear at large strains and curvatures. This nonlinear behaviour highlights the importance of understanding the constitutive relationships of thin composites under large deformations in order to accurately characterise their mechanical behaviour up to failure.

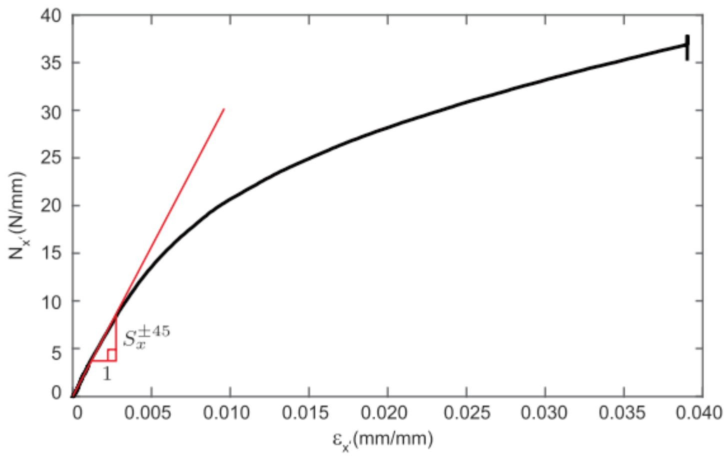

Fig. 1.6: Typical tensile response of a two-ply (± 45) thin woven carbon-fibre laminate. Adapted from [9].

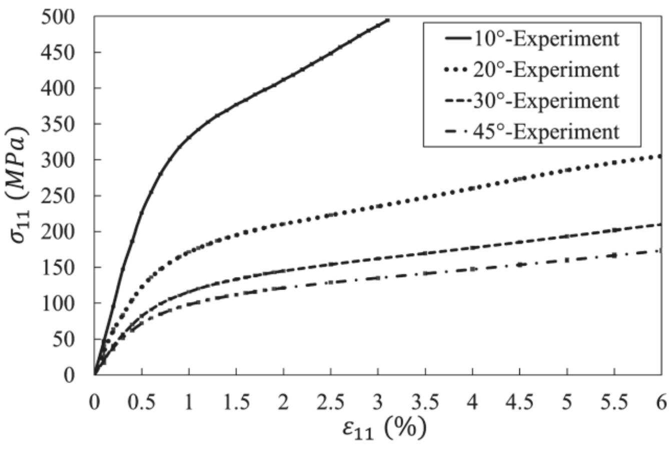

Fig. 1.7: Stress–strain curves of the plain carbon-fibre woven composite under off-axis tensile loads. Adapted from [10].

This nonlinearity of the mechanical properties of composites can be broadly categorised into two types: geometric nonlinearity and material nonlinearity. Geometric nonlinearity arises from the deformation of the material under applied stresses and moments. Large deformations and displacements, changes in load distribution, and distortions of cross-section and thickness can alter stresses and bending stiffness, contributing significantly to nonlinear structural behaviour [12], [13], [14], [15].

Material nonlinearity, on the other hand, results from intrinsic material behaviours such as matrix plasticity, fibre reorientation (rotation and kinking), fibre-matrix debonding, interlaminar failures, and microfractures (see Fig. 1.9) [10], [16], [17], [18]. These phenomena affect the load-bearing capacity and progressive failure mechanisms of composite structures.

To account for these effects in numerical models, reduced stiffness values can be used to represent the deformed or partially damaged state of the material. However, since deformations and micro-failures evolve progressively over time, assuming a constant stiffness throughout a simulation may not accurately capture the full nonlinear behaviour of composites.

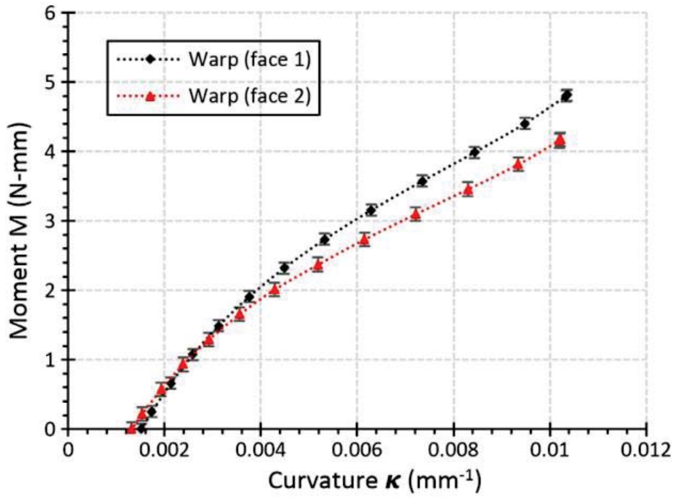

Fig. 1.9: Bending moment versus curvature of carbon-fibre prepreg sample in warp direction at room temperature. Adapted from [11].

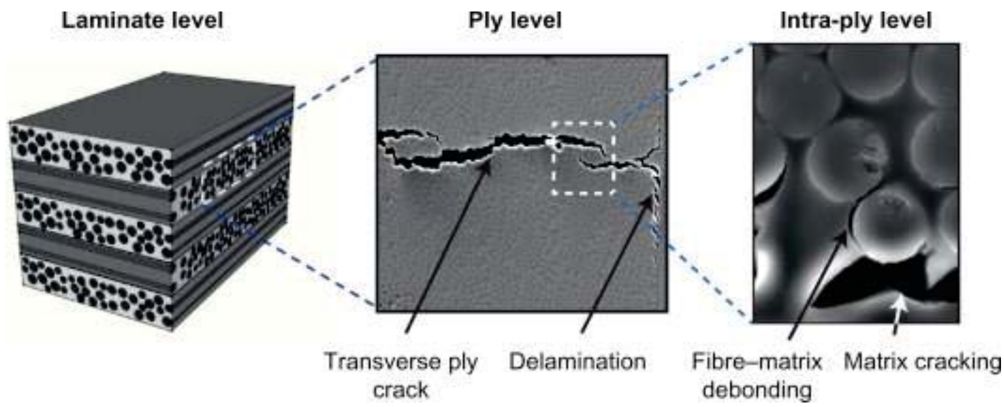

Fig. 1.8: Hierarchical nature of material damages in a composite. Adapted from [18].

1.3. Previous Studies Conducted on Nonlinear Behaviour of Carbon-fibre Composites

Numerous studies have investigated the nonlinear behaviour of composites using both analytical and numerical approaches. These studies encompass a range of composite types, from unidirectional to woven composites. While most research has focused on the nonlinearity of in-plane properties, relatively few studies have explored out-of-plane behaviours such as flexure and pure bending. Furthermore, investigations considering material nonlinearity, including matrix and fibre plasticity, fibre-matrix debonding, and micro-cracking, remain limited.

A summary of past studies on the nonlinear behaviour of thin composites is presented in the table below (see Table 1.1).

Table 1.1: Summary of previous studies conducted to investigate the nonlinear material properties of composite

	Category	**Analytical Studies**	**Numerical Studies**
In-plane properties	Unidirectional composites without material nonlinearity	van Dreumel and Kamp (1977), Northolt et al. (1991), Xie and Adams (1995), Shioya et al. (1996), Vyas et al. (2011), Hahn and Tsai (1973), Goldberg et al. (2014)	Tabatabaei et al. (2014), Leclerc and Pellegrino (2020)
	Unidirectional composites with material nonlinearity	Ju et al. (2008), Vogler et al. (2013), Wu & Ju (2017), Chen et al. (2020), Puck and Mannigel (2007), Wang et al. (2020)	Erice and Thomson (2023), Tan and Falzon (2021)
	Woven composites without material nonlinearity	Rasin et al. (2015), Chatterjee et al. (2021), Tan and Falzon (2021)	
	Woven composites with material nonlinearity	Ishikawa and Chou (1983), Huang (2000), Ogihara and Reifsnider (2002), Murphey et al. (2015), Mohamadipoor et al. (2018), Wang et al. (2022)	Muc (2020), Tabiei and Jiang (1999), Bogetti et al. (2004), Tabiei and Ivanov (2004), Cousigné et al. (2013), Madke and Chowdhury (2019), Zhou et al. (2024), Zscheyge et al. (2020), Xu et al. (2020)

Out-of-the-plane properties	Unidirectional composites without material nonlinearity	Sanford et al. (2010), Okereke (2016)	
	Unidirectional composites with material nonlinearity	Sharma et al (2024)	
	Woven composites without material nonlinearity		Ryou et al. (2007), Liu et al. (2021)
	Woven composites with material nonlinearity		Le et al. (2022)

Among the studies considered, those that explicitly incorporate stiffness degradation arising from micro-fractures and progressive failure mechanisms (e.g., matrix cracking, fibre-matrix debonding, delamination, fibre kinking) provide more reliable and realistic predictions of both the nonlinear load-deformation response and the onset of instability. The reason is, models that consider only geometric nonlinearity typically assume constant material stiffness and therefore tend to under- or over-estimate structural capacity and deformation behaviour, especially as damage accumulates and the response approaches failure.

Because composite stiffness evolves with strain and damage, this effect is commonly captured in finite element analyses by updating the effective stiffness incrementally throughout the simulation [19], [20]. For this purpose, Fortran-based subroutines are commonly employed, allowing the dynamic update of material properties during the simulation. The User-Defined Material (UMAT) subroutine is widely used for this task [21], [22], [23], [24] However, other subroutines, such as User-Defined Field (USDFLD) and User-Defined General Shell Section (UGENS), can also be utilised , depending on the modelling framework

Beyond subroutines, alternative numerical techniques have been implemented. The superposition of piecewise linear segments, which updates the effective stiffness of laminates at each load increment, has been explored for nonlinear response of shear of composite laminates [25]. Additionally, elastic-perfectly plastic flow rules have been incorporated in numerical models to study nonlinearity of in-plane properties of both unidirectional and woven composites [16]. These numerical methodologies are discussed in Section 2.

Analytical models have also been developed to capture material nonlinearity. Some approaches modify representative unit cell properties to account for nonlinear behaviour [13]. The Ramberg-Osgood nonlinear equation, known for its ability to model smooth elastic-plastic transitions, has been applied in both analytical and numerical studies [26], [27]. Other notable models include bimodal constitutive models [28], the nonlinear three-phase micromechanical bridging model [10], probabilistic fibre debonding predictions [29], and the two-dimensional inter-fibre fracture criterion [30]. Furthermore, modifying stress-strain relationships by introducing a quadratic coefficient has been proposed and successfully implemented in finite element codes, including subroutines [17]. Please refer to Section 2 for detail information about the methodologies of above-mentioned studies. Further details of these methodologies are provided in Section 2.

1.4. Research Gap and Scope of the Study

Despite significant efforts to understand the behaviour of composites under high tension, compression, and shear, numerical and analytical models for predicting their nonlinear bending behaviour under large deformations remain limited (see Table 1.1) [17]. In particular, studies on the bending behaviour of ultra-thin woven composites are scarce.

Therefore, this study focuses to develop a multi-scale modelling approach capable of capturing the nonlinear bending behaviour of ultra-thin woven composites under large curvatures. Furthermore, the study seeks to extend this approach to real-world aerospace structures to investigate their nonlinear characteristics.

1.5. Aim, Objectives and Methodology

The aim of this thesis is to develop a multiscale numerical framework to accurately capture the nonlinear bending response of ultra-thin woven carbon-fibre composite structures undergoing large deformations. The framework is designed to remain robust for complex geometries and response mechanisms, enabling reliable structural-scale simulations.

To achieve the focus, the following objectives were formulated:

- Formulate a homogenised macro-scale stiffness model for thin-woven composite shell sections which varies with curvatures and validate the constitutive response against experimental data
- Apply the proposed methodology to analyse the structural behaviour of complex mechanisms of singly curved thin-walled woven composite structures under large curvatures

The methodology for achieving each objective is outlined as follows.

- Conduct a thorough literature review on multi-scale modelling of ultra-thin woven fibre composites and analytical models describing the material nonlinear behaviour
- Develop a macro-scale modelling framework that maps curvature to bending stiffness (D_{11} and D_{12} of the ABD matrix) obtained from a meso-scale representative unit-cell model, and updates the homogenised bending stiffness during deformation via a Fortran user subroutine
- Verify the implementation and validate the framework against pure-bending experimental results available in the literature
- Select a representative singly curved ultra-thin woven carbon-fibre composite structure (e.g., a tape spring) and develop its macro-scale finite element model
- Simulate the structure with deformation-dependent stiffness updating using the validated subroutine to incorporate stiffness degradation
- Validate the predicted moment–rotation response using established analytical formulations
- Perform a parametric study to quantify the influence of stiffness reduction and key geometric parameters on the global structural response and stability

1.6. Outline of the Thesis

Following the introduction, Chapter 2 presents a detailed literature review, covering parallel studies on the nonlinear structural behaviour of carbon-fibre composites, tape-spring mechanics, and the nonlinear properties of thin woven carbon-fibre composites.

Chapter 3 introduces the multiscale modelling approach, incorporating a user-defined general field subroutine, and presents its validation on a macro-scale flat plate model. Chapter 4 explores the effects of stiffness degradation on the macro-scale structural behaviour of woven composite structures.

Chapter 5 outlines the conclusions drawn from the study and suggests potential directions for future work.

CHAPTER 2

2. LITERATURE REVIEW

The studies which have been done so far on the nonlinearity of the stress-strain curve of composites can be categorised under main three topics [31]. They are, macro-scale experimental investigations and phenomenological models, multi-scale analytical models, and multi-scale modelling numerical models. See Fig. 2.1. Unidirectional (UD) fibre composites were first investigated under above mentioned categories. Later, plain woven composites and 3D composites were taken into consideration. In this literature review, the evolution of studies conducted on multi-scale modelling of both the UD as well and woven composites will be discussed.

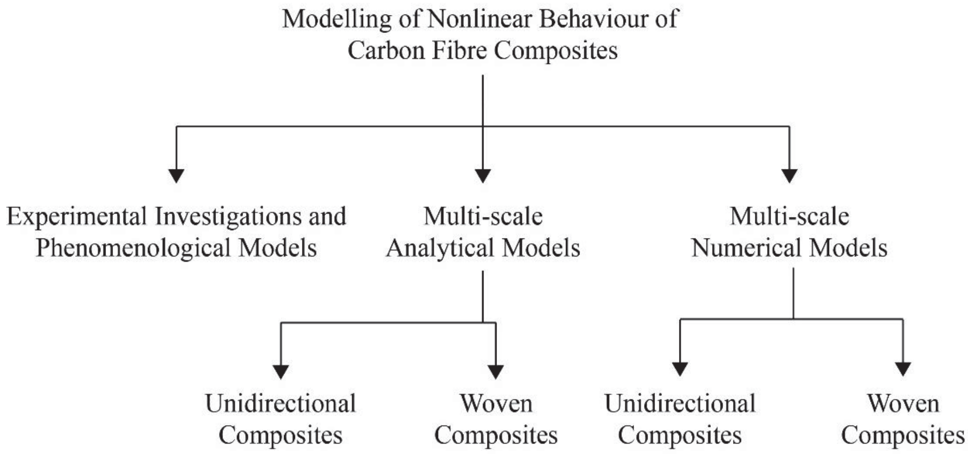

Fig. 2.1: Categories of models

2.1. Investigations on Nonlinear Behaviour of Unidirectional Fibre Composites

Unidirectional composites are being widely used in aerospace and automobile industries because of their promising advantages of strength-to-weight ratio. Unidirectional fibre composites are more suitable for applications with limited transverse force, where the strength provided by cross fibres, which are absent in unidirectional composites, is not required.

2.1.1. Analytical Investigations

Researchers found that the strass-strain response of unidirectional composites is not linear throughout the deformation, which is a crucial understanding for optimising composites. Literature classifies studies on nonlinearity into two categories, those that account for damage mechanisms and those that do not.

2.1.1.1. *Nonlinearity Studies Excluding Fracture Mechanisms*

By the 1970's it was assumed that the tensile behaviour of unidirectional fibre composites follows Hooke's Law with two separated Young's Moduli. However, an empirical relation between Young's modulus and the tensile stress is derived and the influence of fibre misalignment on this relation is examined by van Dreumel and Kamp [32] to prove non-Hookean behaviour of unidirectional fibre.

Research was continued to examine the nonlinearity of composites under axial forces and stresses. Northolt et al. [33] studied the factors that influence the tensile curve of carbon fibres and found in-plane modulus of the graphite plane e_1, the modulus for shear between the graphitic layer planes g, and the orientation distribution of these planes have an impact on the tensile curve. In 1995, Xie and Adams [34] developed an analytical model which offers a way, to generate stress-strain data using micromechanics simulations, to develop the plastic behaviour of unidirectional composites efficiently. The study used Hill's anisotropic yield function to model compression and short-beam shear tests of composite materials.

Then, studies have been conducted to investigate the influence of crystallites on the tensile non-linearity of carbon fibre composites. Shioya et al. [35] found that the mosaic model, which allows to transfer of stresses of the crystallites in both the transverse and axial directions, showed a quantitative agreement with the increases in the tensile modulus, rather than one-dimensional array models (see Fig. 2.2). Further, a traditional 3D formulation where the Raghava pressure-dependent yield function is combined with a null plastic flow in the fibre direction is utilised by Vyas et al. [36]. This captures the effect of hydrostatic pressure on both the elastic and non-elastic material response and the effect of multiaxial loading, which are often neglected in the constitutive modelling of unidirectional composites.

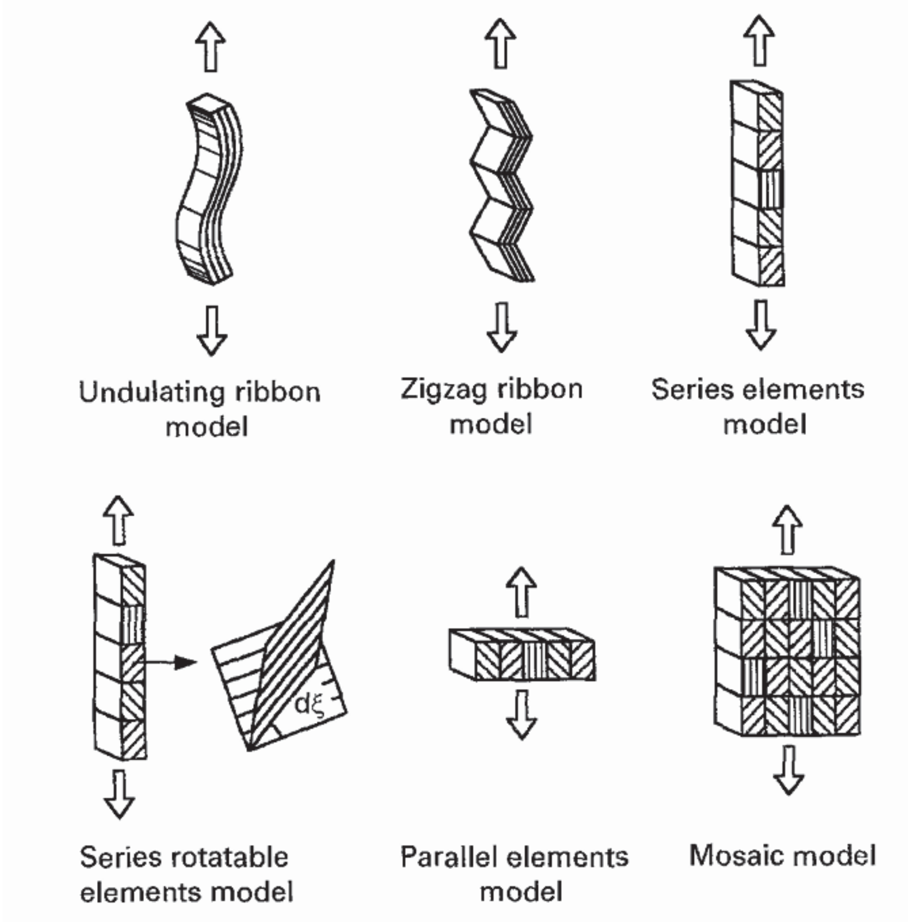

Fig. 2.2: Schematic representation of one-dimensional array models and Mosaic Model. Adopted from [35].

Then, research has been conducted considering the shear modulus and its nonlinearity. In 1973, Hahn and Tsai [12] identified a non-linear shear stress-strain relationship using elastic energy density. However, the linear behaviour remained the same under uniaxial loading. Then Goldberg et al. [37] proposed a one-dimensional, component-by-component, shear plasticity model, which allowed the input of piecewise stress-strain curves. Tsai-Wu composite failure model was utilised in the yield function, and a non-associative flow rule was used to calculate how the material deforms under stress.

A bimodal constitutive model is assumed by Murphey et al. [38] and that model assumes stress is a quadratic function of strain in tension and compression with the same slope at zero strain. This model successfully predicts the flexure behaviour for moderate strains of unidirectional fibre composites, however, does not accurately predict the behaviour for large strains. Nevertheless, the modification of reducing the fibre modulus to zero at a critical compressive help better capture the large strains.

Meanwhile, the test methods were developed in the scientific world, to capture the curvature and bending moment until the failure. Column Bending Test was introduced to capture the entire curvature from the initiation to the failure, of composites [39].

Previously, the Four Point Bending Test and Platen Folding Test lacked demonstrating the entire bending behaviour due to their own drawbacks [40], [41].

Because of that, analytical and numerical models were developed to understand the nonlinear bending response under curvatures. Sanford et al. [14] developed analytical equations to simulate the experimental test. The equations were developed utilising a geometrically nonlinear elastica approach, paired with a two-parameter nonlinear elastic material model that incorporates graphite crystallite reorientation.

In addition to that, Sharma et al. [17] investigated the error in predicting the curvatures using a closed-form equation and elastica theory, described through ξ, which measures the ratio between the total size of the rigid arms and the specimen free length. They observed that errors in the closed-form solution (i.e., the relative difference between the closed-form solution and its corresponding elastica solution) reduce as ξ is increased (see Fig. 2.3).

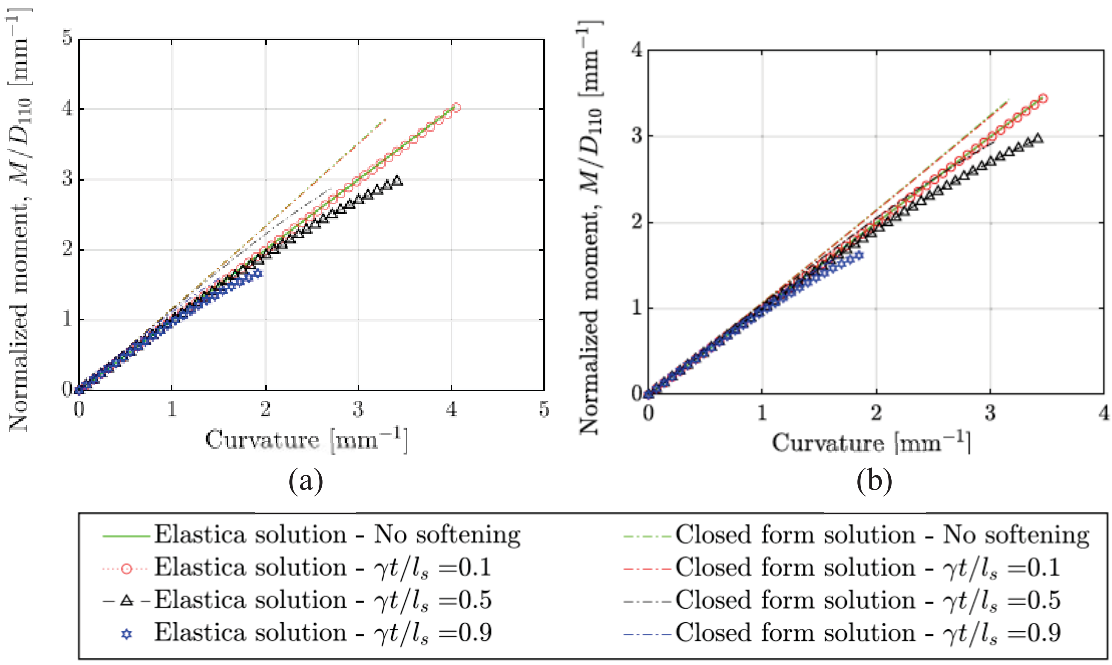

Fig. 2.3: Maximum moment predicted by the elastica for $(a)\varepsilon = 0.5, (b)\varepsilon = 2$, and the closed-form solution, as a function of the maximum curvature on the specimen (γ is the nonlinear material parameter, l_s is the free length of specimen, t is the specimen thickness and D_{110} is the initial bending stiffness). Adopted from [17].

2.1.1.2. *Nonlinearity Studies Including Fracture Mechanisms*

Elastoplastic damage models were developed for unidirectional composites under different load conditions. Then, investigations were carried out to find the influence of failures of components (such as fibre and matrix) of composites on the nonlinearity of constitutive models.

Initially, researchers paid attention to numerical models which account for axial forces. In 2008, a two-level elastoplastic evolutionary damage model, specified on fibre debonding, was proposed by Ju et al. [29] (see Fig. 2.4). The probability of fibre debonding is predicted using the Weibull function (a statical method) and tested under both the uniaxial and biaxial stresses. In addition to that, an orthotropic invariant-based plasticity along with a non-associated flow rule, which predicts volume changes during plastic deformation correctly, was introduced to unidirectional composites by Vogler et al. [42]. Their model simulated plasticity-related non-linearity under triaxial compressive stresses.

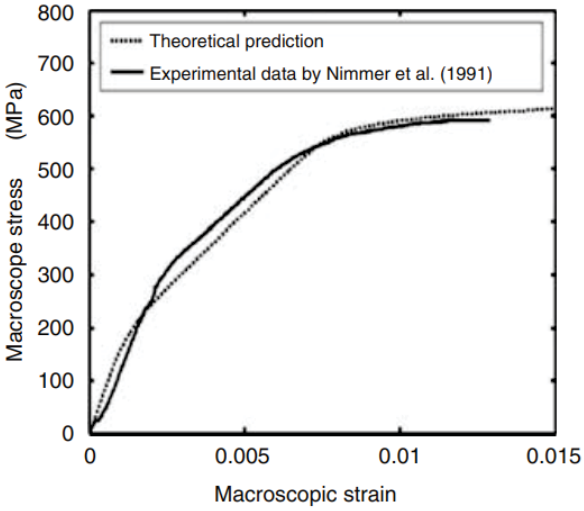

Fig. 2.4: Comparison of predicted and measured uniaxial transverse stress–strain behaviour. Adopted from [29].

Wu & Ju [43] showed the nonlinear behaviour of a composite under uniaxial and axisymmetric load is primarily influenced by the plastic deformation in the matrix as well as the damage evolution due to fibre breakage, investigating behaviours of matrix and fibres using mathematical rules and statistical approaches respectively. Moreover, Chen et al. [44] have considered both the plastic-hardening and damage-softening processes and proposed a plastic yield criterion with four parameters.

Puck and Mannigel [30] took the shear nonlinearity into account by scaling the non-linear shear stress-strain curves according to their own physically-based two-dimensional inter-fibre fracture criterion. Further, the model used a variable called the stress exposure ratio (f_E), which measures the risk of inter-fibre fractures. The ratio is calculated using fracture criteria based on realistic material behaviour. In addition, Wang et al. [45] evaluated the nonlinear behaviour of a composite from properties of fibre, matrix plasticity and interphase damage using a three-phase micromechanics bridging model (see Fig. 2.5), which links this damage stress to the stiffness loss in the interphase.

Moreover, the material nonlinearity, the stress-strain relationship in the direction of bending, is described by γ (a parameter that determines the level of nonlinearity), the coefficient for a quadratic term in the stress-strain relationship of the laminate by

Sharma et al [17] (see Fig. 2.6). Strains where the instantaneous modulus becomes zero, that is where $\varepsilon = -1/\gamma$, are marked with a star symbol in Fig. 2.6

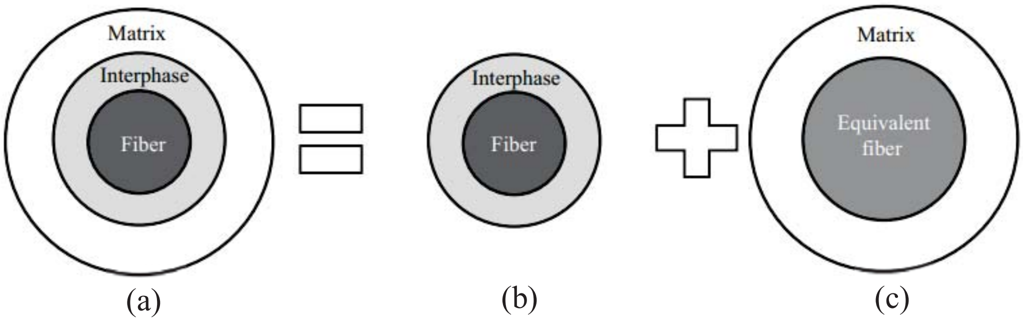

Fig. 2.5: Equivalent fibre method for a three-phase composite. (a) Three-phase composite (b) Inner two-phase composite (c) Global two-phase composite. Adapted from [44].

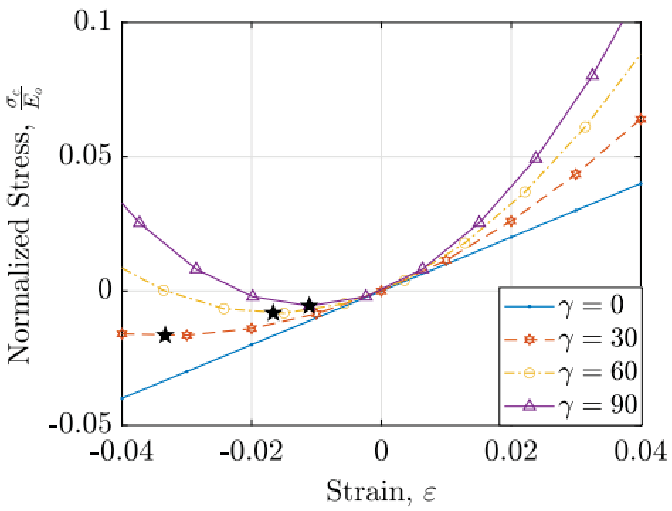

Fig. 2.6: Normalised stress vs strain for four different values of the parameter γ describing fibre nonlinearity. Adapted from [17].

2.1.2. Numerical Investigation

Numerical models offer certain advantages over experimental investigations, such as, they are flexible to modify, cost-effective and can be utilised for parametric studies. Even though numerical models need computational power, the precision can be higher than analytical models, as the finite element modelling (FEM) software is highly accurate and provides facilities to model real phenomena.

2.1.2.1. *Nonlinearity Studies Excluding Fracture Mechanisms*

There were several alternative methods considered in modelling unidirectional composites numerically. Tabatabaei et al. [46] used Embedded Element (EE) technique, which models fibres and matrix separately, for single fibre problems, unidirectional reinforcements and 5-harness satin woven composites. The EE model matches the continuous mesh model in predicting elastic properties, stress distributions, and critical stress locations, while offering a simpler and potentially faster way. On the other hand, a method was proposed by Leclerc and Pellegrino [47] to model nonlinear compressive behaviour using a linear analysis. They reduced the applied load until a linear buckling analysis can be performed successfully in the deformed configuration. This method allowed predict non-linear buckling.

2.1.2.2. *Nonlinearity Studies Including Fracture Mechanisms*

Studies have been conducted to capture the material nonlinearity, incorporating the failure mechanism in micro as well as meso scale. In models, authors used different methods to update the stiffness variations of materials and interactions due to failures.

Fortran language subroutine also facilitates updating the stiffness of the model with the strain. Erice and Thomson [22] proposed a model which implemented the developed constitutive equations in a Fortran language subroutine as a user-defined material model in LS-DYNA non-linear explicit time integration finite element solver to introduce the plasticity in both fibre- and matrix-dominated directions. This model mainly investigated the axial forces.

The shear nonlinear response was successfully captured Tan and Falzon [15] by introducing a phenomenological model based on the assumption, epoxy matrix is perfectly plastic, to capture the nonlinearities of the unidirectional fibre reinforced composites. Simple shear and transverse compression were considered in the validation of the model.

2.2. Investigations on Nonlinear Behaviour of Woven Fibre Composites

2.2.1. Analytical Investigations

Textile composites offer several advantages over unidirectional composites, making them highly desirable in various engineering applications. One key benefit is their superior static and impact strength, allowing them to endure higher loads and absorb energy more effectively under sudden impacts. Additionally, textile composites exhibit enhanced delamination resistance due to their interwoven structure, which provides better cohesion between layers and reduces the likelihood of separation under stress [48]. Their improved drapability makes them suitable for forming complex shapes, a critical requirement in industries like aerospace and automotive engineering. These combined benefits make textile composites a versatile and practical alternative to unidirectional composites in demanding applications. Therefore, studies have been conducted to investigate the stress-strain response of woven composites until failure.

2.2.1.1. Nonlinearity Studies Including Fracture Mechanisms

Nonlinear constitutive model combining the Hahn and Tsai equations and the one dimensional fibre undulation model and bridging model for satin composites were utilised by Ishikawa and Chou [13] (see Fig. 2.7). The model mainly accounts geometrical nonlinearity and the shear deformation of fill threads by considering the extensional deformation of the pure matrix regions and transverse cracking of the warp regions.

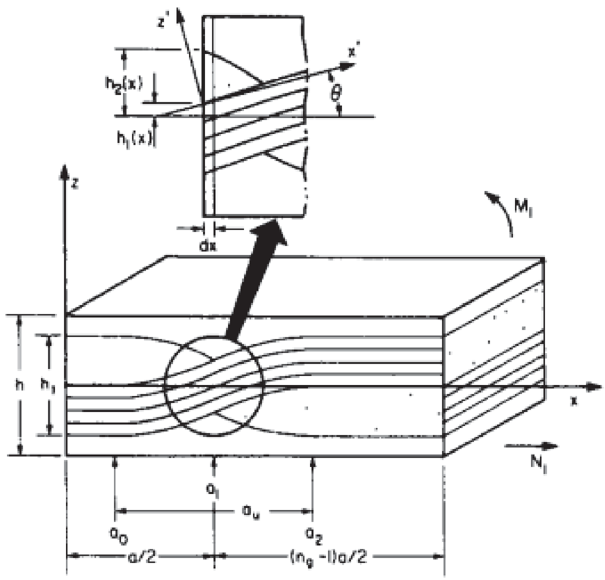

Fig. 2.7: The one-dimensional fibre undulation model. Adapted from [13].

In 2000, Huang [49] developed a micromechanics-based model which the elastoplastic behaviour of warp yarns, fill yarns, and matrix are calculated utilising the bridging model are involved. However, the damage of the interface between the fibre and matrix is not involved in the study. Furthermore, the nonlinear behaviour of woven composite was approximated as a cross-ply laminate by Ogihara and Reifsnider [50], assuming it behaves like a combination of unidirectional composites. Then unidirectional laminate is assumed to be described by the one-parameter plasticity model and validated with the experimental results.

Moreover, Mohamadipoor et al. [51] have proposed a two-dimensional analytical model for investigating the nonlinear ballistic impact (high-velocity impact) behaviour of nanocomposite laminates. A new deformation function was introduced to investigate normal and shear strains with the plate stretches and shears and energy absorption in different regions during impact. In 2022, Wang et al. [10] have developed an analytical model by combining a discrete method to divide a woven composite into smaller parts (representative volume element (RVE) cub-cells) and a novel nonlinear three-phase micromechanical bridging model to simulate the behaviour of unidirectional composite (see Fig. 2.8). Sub-cells are modelled with two unidirectional composite layers and pure matrix layers. The nonlinearity incorporated through matrix behaviour and interface damage.

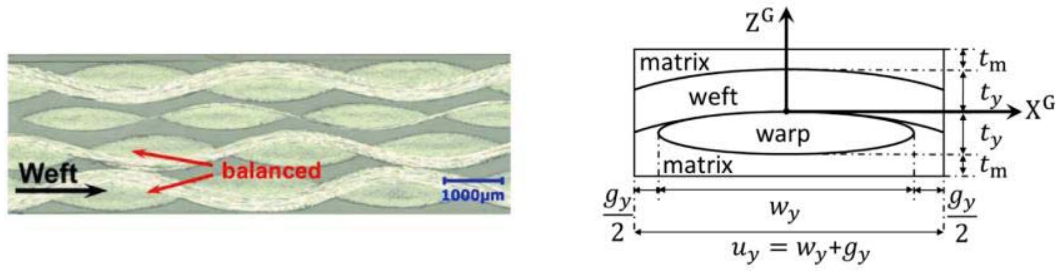

(a) Experimental image[37]　　(b) Geometrical model

Fig. 2.8: Cross section of a plan woven composite. Adapted from [10].

2.2.2. Numerical Investigations

In the past, modelling woven composites has been difficult because of their complex microstructure, which involves interlacing fibres in multiple directions to create mechanical interactions, capturing the nonlinear stress-strain behaviour, damage initiation, and progression within this structure requires detailed representation at both the macro and micro scales. Early modelling approaches often oversimplified these materials, resulting in inaccurate predictions. However, advances in computational power and numerical methods, such as FEM and multi-scale analysis, have greatly improved the accuracy of woven composite modelling.

Methods such as RVEs and advanced constitutive models make it possible to precisely simulate fibre-matrix interactions and damage mechanisms. Superposition techniques were also utilised to generate periodic meshes to minimise the complexity of finite element analysis (FEA) [52]. Additionally, machine learning and experimental validations have improved predictive capabilities, overcoming previously woven composite modelling limitations.

2.2.2.1. *Nonlinearity Studies Excluding Fracture Mechanisms*

It can be found some studies tried to capture the nonlinear behaviour of composites using geometric changes and plasticity of materials, without incorporating continuum fracture mechanisms. These studies also depicted a significant match to the experimental data. However, to obtain the actual stress-strain curve until the failure, micro-cracks and failures should be included in the models.

The uniaxially compressed stability of triaxially woven fabric composites has been investigated by Rasin et al. [53]. Authors have performed a geometrically nonlinear FE formulation for the composites plate firstly, adopting Kirchhoff's hypothesis. The Newton–Rhapson method has been employed to perform an iterative linearisation of the formulated nonlinear equation (see Fig. 2.9).

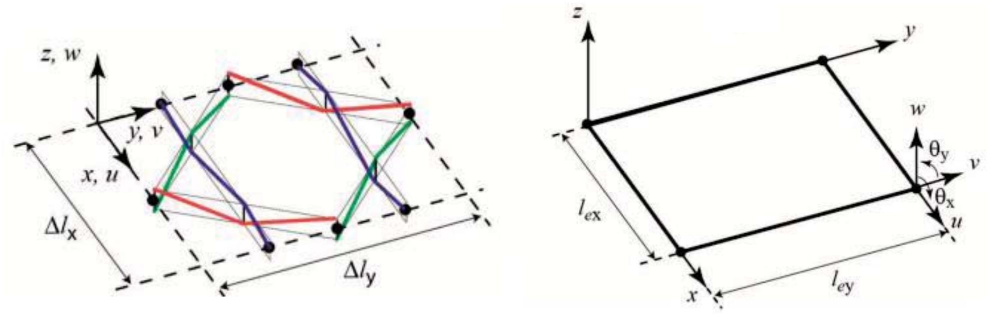

Fig. 2.9: Single plate element and associated degrees of freedom modelled on the basis of one unit cell. Adapted from [53].

Chatterjee et al. [54] have investigated skewed hypar shells considering their geometry. The geometric nonlinearity is obtained by minimising the residue to approximately zero ($\psi \approx 0$) which was achieved by Newton-Raphson's scheme of incremental iterative approach (see Fig. 2.10).

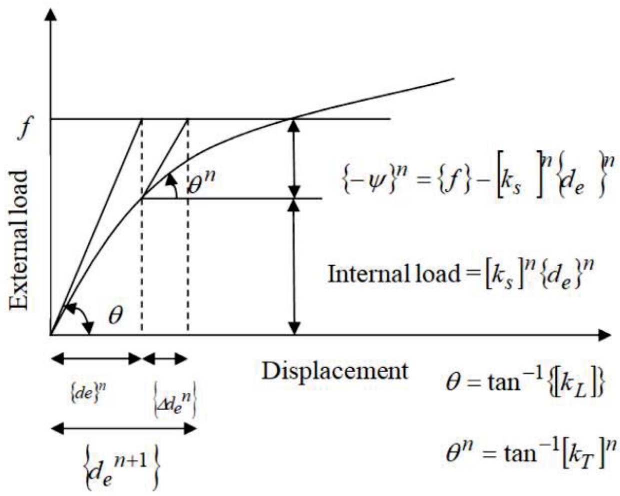

Fig. 2.10: Newton–Raphson iterative scheme. Adapted from [54].

Residue ψ is calculated as Equation 2.1 where f means external force and P means internal force.

$$f - P = \psi \tag{2.1}$$

In addition, in the same study Tan and Falzon [15] have done in 2021, they modelled the shear test of $[\pm 90°]_{4s}$ composite laminates, introducing perfect bonding between the neighbouring plies, which enabled the cross-ply coupling effect with neighbouring plies. The methodology is in very good agreement with the initial yield and linear hardening regions (see Fig. 2.11). The reason for the mismatch in the damage is the absence of a composite damage model.

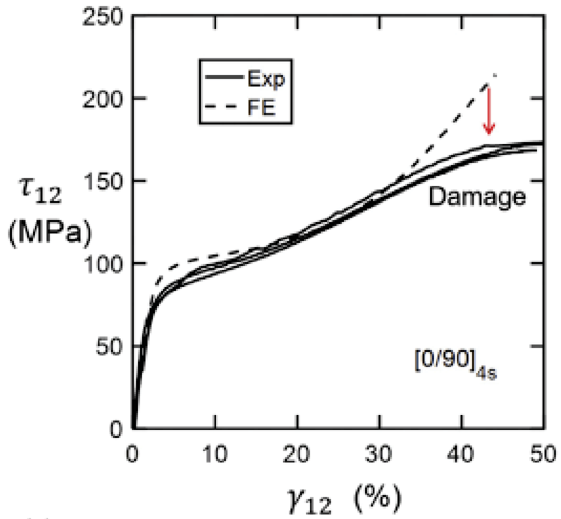

Fig. 2.11: Comparison between the experimental and numerical true shear stress-strain responses of [±90]$_{4s}$ laminates under shear loading. Adapted from [15].

2.2.2.2. *Nonlinearity Studies Including Fracture Mechanisms*

Muc [16] has shown how important accounting for geometrical and physical non-linear effects is in accurately predicting the behaviour and failure of composite structures, particularly in pressure vessel components under axial forces. Yield strength is assumed to be constant during plastic deformation and hence, the elastic-perfectly plastic behaviour is considered. The physical nonlinearity is included in the model using an elastic-perfectly plastic flow rule which is in the same form as for isotropic materials. However, it is not clear how the flow rule is incorporated into the FEM programme. The analysis was carried out to investigate the shear and bending nonlinearity as well.

Tabiei and Jiang [21] have proposed a multi-scale numerical model which updates the stress-strain relationship of representative cell and shell element from the cell model and passes down stress and strains to representative cell and sub-cell from shell element using UMAT subroutines. The axial and shear nonlinearity of 16 and 32 plies cases were modelled here, nevertheless, the study failed to validate the results.

Then, Bogetti et al. [25] used the Ramberg-Osgood relationship, which calculates how the laminate's stress and strain change step by step under axial and shear forces, for predicting the nonlinear stress-strain response and failure behaviour of individual plies of composite laminates. Bogetti et al. achieved the nonlinearity from the superposition of piece-wise linear segments, in which the effective laminate stiffness matrix is updated based on strain-dependent tangent (see Fig. 2.12) ply properties at each load increment. However, the method of updating the stiffness in the FEM software is unclear.

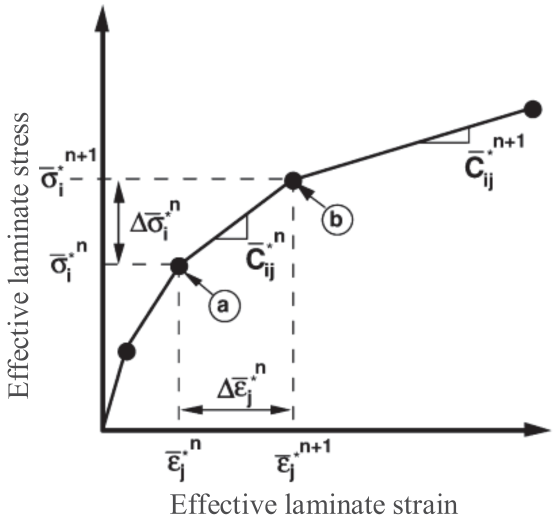

Fig. 2.12: Incremental laminate loading methodology (a) n^{th} increment, (b) $n+1^{th}$ increment. Adapted from [25].

In addition, a computationally efficient model for plain-woven composites based on a four-cell RVE model was developed by Tabiei and Ivanov [27]. The micro-mechanical material model programmed in MATLAB calculates the stress response of the woven fabric composite due to steady strain loading with a constant strain increment in tension and pure shear. The material model with failure is programmed as a user-defined subroutine as well in the LS-DYNA finite element code with explicit time integration. Further, the Ramberg-Osgood nonlinear equation was also used. Cousigné et al. [26] have also utilised the Ramberg-Osgood relationship or a user-defined load curve to account for the nonlinear shear effects in composite materials along with user-defined subroutine (UMAT) in the LS-DYNA finite element code. The maximal stress criterion and Tsai–Wu quadratic failure criterion was used to predict the failure.

Moreover, Madke and Chowdhury [24] have proposed a multi-scale model for both the 2D and 3D woven composites under shear. The model was based on representative unit volumes of two stages which are fibres enclosed embedded in a matrix and mesoscale reinforced inside a matrix. UMAT subroutine is utilised in selecting failure criteria and damage. Further, the model incorporates factors often neglected in other models, such as surface imperfections, residual stresses, and glitches at the microscale, by using a cohesive interphase.

The study carried out by Zhou et al. [19] focused on the shear nonlinearity of plain-woven composites, especially at high temperatures. The in-plane shear nonlinearity machine learning-based constitutive model, developed using Gaussian process regression (GPR), is integrated into the FE program via a user-defined material (UMAT) subroutine (see Fig. 2.13). The subroutine operates differently from typical elastic material models in two keyways. First, the GPR model (Instead of a standard elastic model) directly calculates σ_{12} based on input shear strain (ε_{12}) and temperature, secondly, the shear-related component (C_{44}) is calculated using a numerical differentiation method (forward difference) while the other components of the matrix remain elastic and unchanged.

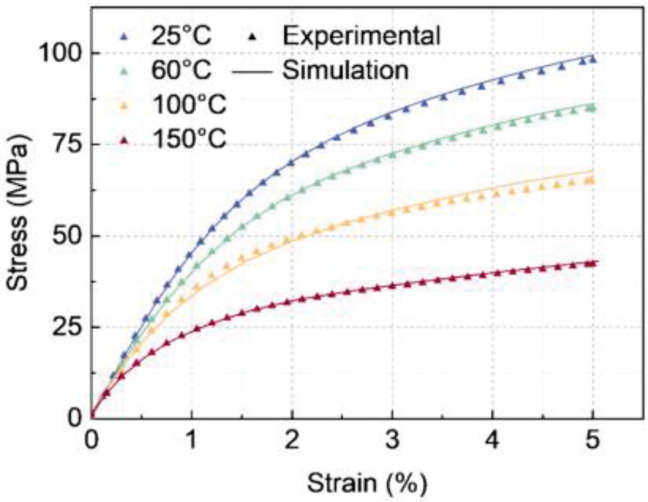

Fig. 2.13: Comparison of actual and predicted stress–strain curves at various temperatures by GPR model. Adapted from [19].

On the other hand, a rate-dependent nonlinear analysis was carried out by Zscheyge et al. [20]. They have developed a viscoelastic-plastic damage model, incorporating spring-dashpot systems to capture viscoelastic over stresses, to describe the behaviour of single ply of a thermoplastic composites laminate, specifically glass fibre-reinforced polypropylene, utilising User-defined material subroutine (VUMAT). Meanwhile, Xu et al. [55] used a multi-scale parametrised visco-plastic unit cell model for plain-woven composites to characterise the nonlinearity and rate-dependency. The material model was implemented with a developed user subroutine.

In 2022, Le et al. [23] has performed a three-dimensional multi-scale modelling approach for a 5-harness satin wave to analyse the viscoelastic behaviour of woven composites. Even though Alshahrani and Hojjati [56] have attempted to capture the viscoelasticity of woven composites without considering material nonlinearity, Le et al. successfully incorporated a UMAT subroutine to account for bending stiffness variations when modelling the nonlinear bending response of a 5-harness satin weave under small curvatures (see the Fig. 2.14 and Fig. 2.15). The method was validated by comparing its results with experimental data from a novel test, which is based on bending of a cantilever beam. This test has been used to characterise the bending behaviour of woven composites [11].

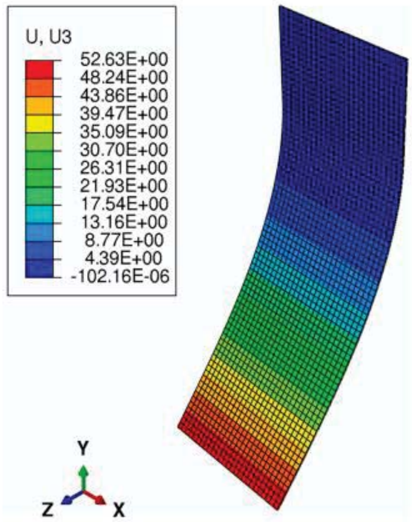

Fig. 2.14: Deformed sample at tip displacement of 50 mm. Adapted from [23].

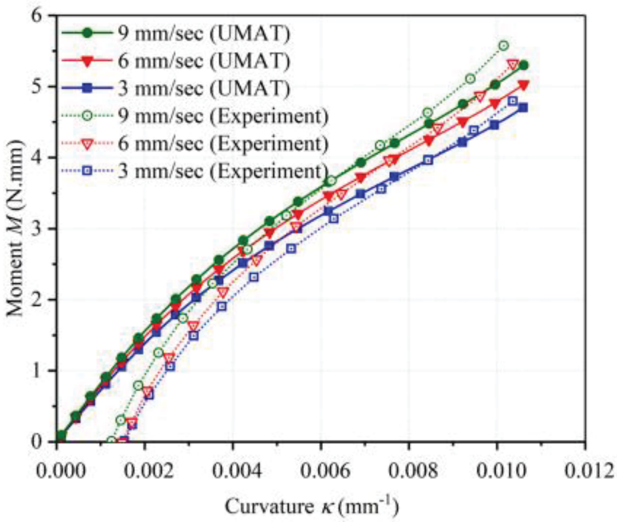

Fig. 2.15: Effect of loading rate on bending moment versus curvature of 5HS prepreg. Longitudinal fibre stiffness is assumed to be 1.5 GPa in all cases. Adapted from [23].

Overall, the literature indicates that while nonlinear behaviour in the in-plane and out-of-plane responses of composites has been widely investigated, analytical and numerical studies focusing specifically on nonlinear bending of woven composites remain scarce. Therefore, there is a clear need for a numerical modelling framework to reliably predict the nonlinear bending response of woven composites, which is the focus of this study.

2.3. Deployable Foldable Carbon-fibre Composite Booms

As outlined in Section 1.5, this study develops a robust numerical framework for modelling the nonlinear bending response of woven composites and extends it to flat and singly curved woven-composite aerospace structures. Accordingly, a brief discussion of the mechanics of deployable booms is warranted, as these systems are commonly realised using thin flat or singly curved woven-composite laminates.

Deployable foldable structures are commonly used in everyday applications such as umbrellas, convertible car roofs, and retractable roofs of large sports stadiums. In the context of aerospace engineering, these structures play a critical role, as they enable the compact storage of large-scale components, such as solar sails and antennas, within the limited space of a launch vehicle.

One of the simplest forms of deployable structures is the stored-energy structure. These systems are held in a compact configuration by constraints, and upon their release, deployment is initiated through the release of elastic strain energy stored within the structure. Examples include Storable Tubular Extendible Membrane (STEM) booms [57], tape-spring booms [58], [59], Triangular Rollable and Collapsible (TRAC) booms [60], and Collapsible Tubular Mast (CTM) booms [61]. While such structures have traditionally been fabricated using isotropic materials like steel, carbon-fibre composites have gained widespread adoption due to their superior mechanical properties, as discussed in Section 1.

2.3.1. Overall Structural Behaviour of Tape-springs

Tape-springs are fundamental components in many deployable booms, particularly in tape-spring hinges. Their structural behaviour is characterised by an initial requirement of a large bending moment to fold the tape-spring up to the point of local buckling,

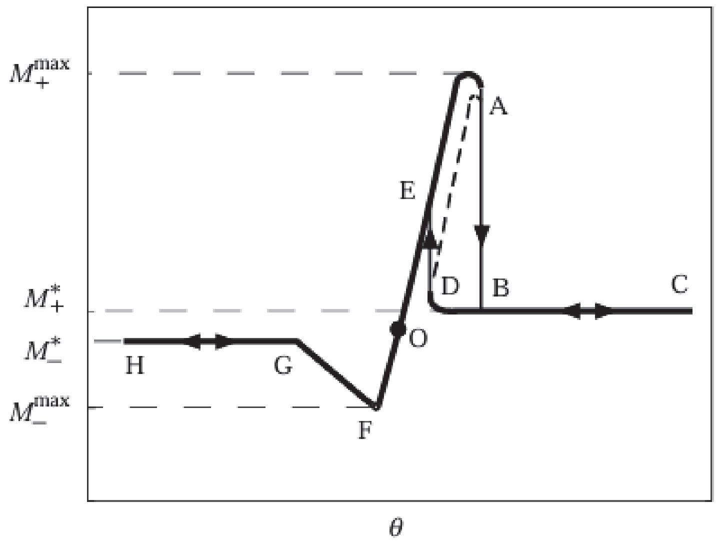

Fig. 2.16: Schematic moment-rotation diagram; the origin is at point O. Arrows show the direction in which each part of the path can be followed. The broken-line path from A to D is unstable. Adapted from [62].

followed by a relatively steady and lower moment for the remainder of the folding process. The deployment behaviour mirrors this pattern; however, the peak moment required during deployment (D to E) is often smaller than that required during folding (A to B) [62] (see Fig. 2.16).

Furthermore, tape-springs exhibit two primary folding directions, commonly referred to as opposite-sense bending and equal-sense bending (see Fig. 2.17). As illustrated in Fig. 2.16, positive θ angles, representing opposite-sense bending, demonstrate a higher peak moment compared to negative θ angles, which correspond to equal-sense bending. Since the peak moment plays a critical role in both folding and deployment, governing the amount of energy required or released, opposite-sense bending has been the focus of most studies in the literature [62], [63], [64], [65], [66], [67], [68], [69]

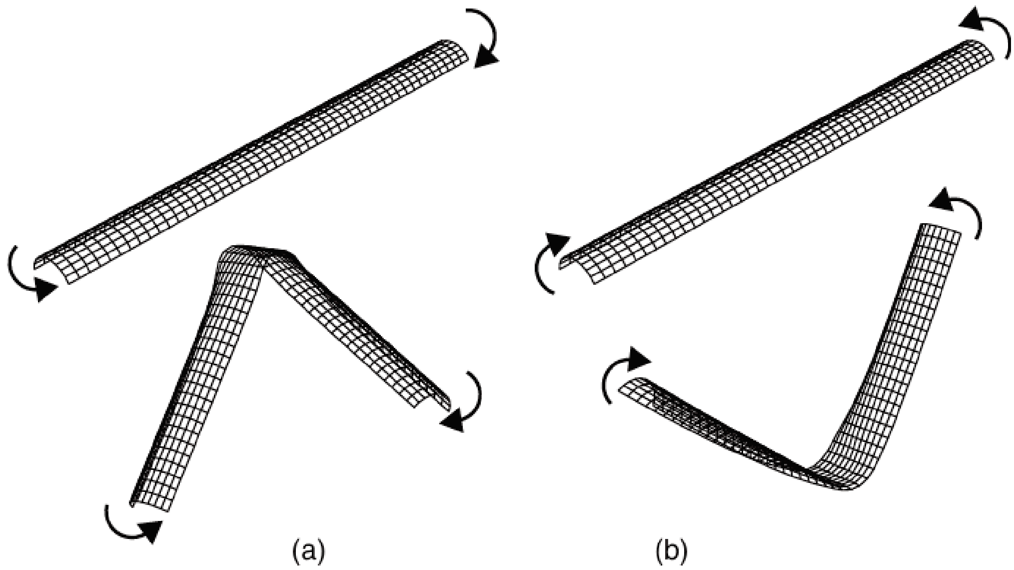

Fig. 2.17: (a) Equal sense bending (b) opposite sense bending of tape-springs. Adapted from [64].

2.3.2. In-plane Stiffness Properties of Woven Composites (ABD Matrix)

The ABD stiffness matrix represents the complete 6 × 6 stiffness properties of a thin woven composite laminate. For a unit element of such a laminate, the applied loads include in-plane forces in-plane forces (N_x, N_y, N_{xy}) bending moments (M_x, M_y), and a twisting moment (M_{xy}). These result in mid-plane strains ($\varepsilon_x, \varepsilon_y, \gamma_{xy}$), bending curvatures ($\kappa_x, \kappa_y$), and twisting curvature (κ_{xy}). The ABD matrix is used to describe the coupling between these loads and the resulting deformations and is fundamental in composite mechanics.

The full matrix is typically expressed as:

$$\begin{Bmatrix} N_x \\ N_y \\ N_{xy} \\ M_x \\ M_y \\ M_{xy} \end{Bmatrix} = \begin{bmatrix} A_{11} & A_{12} & A_{13} & B_{11} & B_{12} & B_{13} \\ A_{21} & A_{22} & A_{23} & B_{21} & B_{22} & B_{23} \\ A_{31} & A_{32} & A_{33} & B_{31} & B_{32} & B_{33} \\ B_{11} & B_{12} & B_{13} & D_{11} & D_{12} & D_{13} \\ B_{21} & B_{22} & B_{23} & D_{21} & D_{22} & D_{23} \\ B_{31} & B_{32} & B_{33} & D_{31} & D_{32} & D_{33} \end{bmatrix} \begin{Bmatrix} \varepsilon_x \\ \varepsilon_y \\ \gamma_{xy} \\ \kappa_x \\ \kappa_y \\ \kappa_{xy} \end{Bmatrix} \tag{2.2}$$

This is often presented in a simplified form for clarity as:

$$\begin{Bmatrix} N \\ M \end{Bmatrix} = \begin{bmatrix} A & B \\ B & D \end{bmatrix} \begin{Bmatrix} \varepsilon \\ \kappa \end{Bmatrix} \tag{2.3}$$

The ABD matrix is symmetric, and each term depends on the laminate geometry, material properties, and the interaction between layers.

The structural behaviour which each stiffness properties characterise is demonstrated in the below illustration (see Fig. 2.18) which is followed by a detailed description of the role of each component [70]:

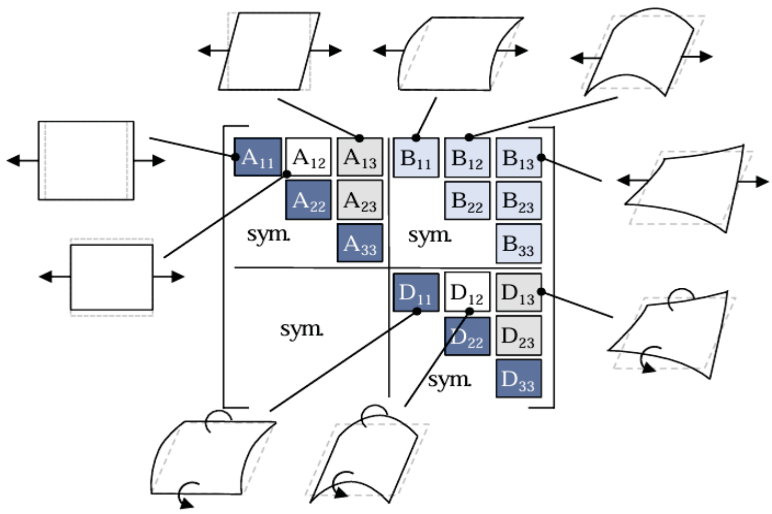

Fig. 2.18: ABD matrix. Adapted from [71].

The $[A]$ matrix, known as the extensional stiffness matrix, describes the in-plane mechanical response of the laminate. It characterises how the laminate resists normal and shear forces within the plane. The terms A_{11} and A_{22} represent the stiffness in the x and y directions, respectively, while A_{12} reflects the influence of the Poisson effect. A_{33} corresponds to in-plane shear stiffness, and the terms A_{13} and A_{13} represent coupling between normal and shear deformation modes. These properties depend on the material layup, ply orientations, and thickness.

The $[B]$ matrix, referred to as the coupling stiffness matrix, captures the interaction between in-plane forces and out-of-plane curvatures, as well as between bending moments and mid-plane strains. The components B_{11}, B_{22}, and B_{12} indicate coupling between membrane extension and bending deformation, while B_{33} represents the coupling between in-plane shear and twist. The terms B_{13} and B_{23} account for the coupling between extension and twist, and shear and bending, respectively. When the

B matrix terms are zero, it implies that in-plane loads do not induce bending or twisting and bending moments do not generate in-plane deformations.

The $[D]$ matrix, known as the bending stiffness matrix, governs the relationship between applied moments and the resulting curvatures in the laminate. D_{11} and D_{12} represent bending stiffness about the x and y axes, respectively, while D_{12} characterises the coupling between bending moments and curvatures in orthogonal directions. D_{33} defines the torsional stiffness, and D_{13} and D_{23} reflect the coupling between bending moments and twist, as well as between twisting moments and bending curvatures. These bending stiffness properties are crucial for predicting the flexural behaviour of composite laminates under various loading conditions.

2.3.3. Mechanics of Composite Tape-springs

The bending moments per unit length, for the curvature changes in both longitudinal and transverse directions, of a tape-spring bends due to a pure bending, can be formulated as:

$$M_x = D_{11} \times \Delta\kappa_x + D_{12} \times \Delta\kappa_y \quad (2.4)$$

$$M_y = D_{22} \times \Delta\kappa_y + D_{12} \times \Delta\kappa_x \quad (2.5)$$

where curvatures are:

$$\Delta\kappa_x = \pm\frac{1}{r} \quad (2.6)$$

$$\Delta\kappa_y = \frac{1}{R} - \frac{d^2w}{dy^2} \quad (2.7)$$

w is the displacement of deformed tape-spring cross section in z direction. κ_{xy} is taken as zero due to the pure bending condition. Here, plus or minus sign of κ_x attribute to the opposite and equal sense bending configurations.

Refer to the Fig. 2.19 for the notations.

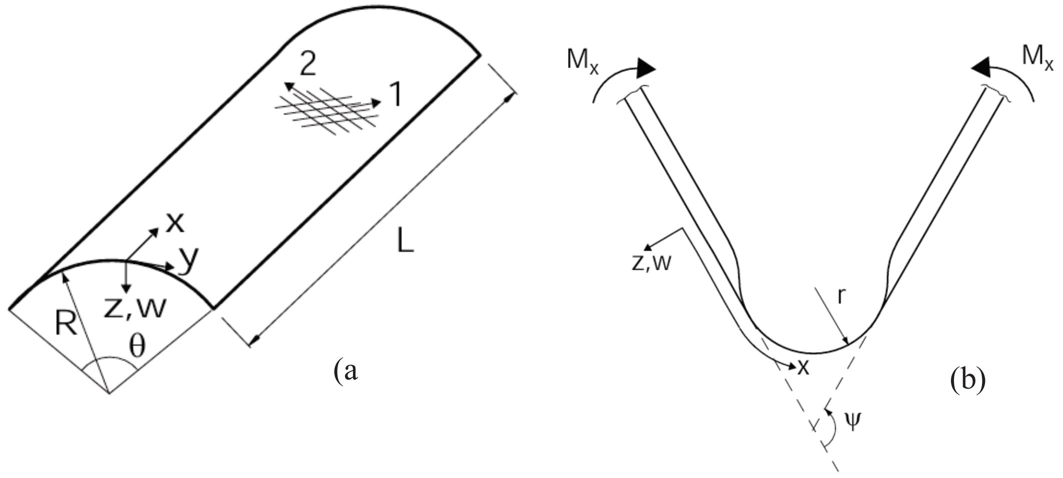

Fig. 2.19: Schematic diagrams of (a) unfolded tape-spring (b) folded tape-spring in equal sense for the understanding of notations. Adapted from [64].

Considering Equations 2.4, 2.5, 2.6 and 2.7, following equations can be formulated for the bending moments per unit width:

$$M_x = \pm D_{11} \times \frac{1}{r} + D_{12} \times \left(\frac{1}{R} - \frac{d^2w}{dy^2}\right) \tag{2.8}$$

$$M_y = D_{11} \times \left(\frac{1}{R} - \frac{d^2w}{dy^2}\right) \pm D_{12} \times \frac{1}{r} \tag{2.9}$$

Considering Equation 2.8 and 2.9, and equilibrium of bending moment per unit width in *y* direction (M_y) and normal force per unit width in *x* direction, following equation for the overall bending moment of the tape-spring is developed [64], [66].

$$M = sD_{11}\left(k_x + \frac{\mu}{R} - \mu\left(\frac{1}{R} + \mu k_x\right)F_1 + \frac{1}{k_x}\left(\frac{1}{R} + \mu k_x\right)^2 F_2\right) \tag{2.10}$$

where,

$$F_1 = \frac{2}{\lambda}\frac{\cosh\lambda - \cos\lambda}{\sinh\lambda - \sin\lambda}$$

$$F_2 = \frac{F_1}{4} - \frac{\sinh\lambda\sin\lambda}{(\sinh\lambda - \sin\lambda)^2}$$

$$\lambda = \frac{fs}{r}$$

$$\mu = \frac{D_{12}}{D_{11}}$$

$$s = 2R\sin{}^{\theta}/_{2}$$

$$f = \sqrt[4]{A_{11}/(4D_{22}r^2)}$$

However, when the fully formed folded region of the tape-spring is concerned, transverse curvature of the folded region can be taken as zero [71]. Therefore, the fully folded region can be idealised to a cylindrical shape.

With that, curvatures can be considered as:

$$\Delta\kappa_y = \frac{1}{R} \tag{2.11}$$

Equation 2.3 can be converted to a mix form for woven composites with symmetric fibres in longitudinal direction of the tape, as follows [64]:

$$\begin{Bmatrix} \varepsilon \\ M \end{Bmatrix} = \begin{bmatrix} A^* & B^* \\ C^* & D^* \end{bmatrix} \begin{Bmatrix} N \\ \kappa \end{Bmatrix} \tag{2.12}$$

where,

$$[A^*] = [A]^{-1}$$

$$[B^*] = -[A]^{-1}[B]$$

$$[C^*] = [B][A]^{-1}$$

$$[D^*] = [D] - [B][A]^{-1}[B]$$

For a 2-ply woven laminate of total thickness $2t$ (thickness of one ply is t) with same fibre orientation for each ply gives zero for the entire $[B]$ matrix of ABD matrix. Therefore, moment-curvature relationship can be given as follows:

$$\begin{Bmatrix} M_x \\ M_y \\ M_{xy} \end{Bmatrix} = \begin{bmatrix} D_{11} & D_{12} & D_{13} \\ D_{21} & D_{22} & D_{23} \\ D_{31} & D_{32} & D_{33} \end{bmatrix} \begin{Bmatrix} \kappa_x \\ \kappa_y \\ \kappa_{xy} \end{Bmatrix} \tag{2.13}$$

Since the considered bending of tape-spring is due to a pure bending, $\kappa_{xy} = M_{xy} = 0$.

Therefore, substituting Equations 2.6 and 2.11 to 2.4 and 2.5, following equations can be derived for the fully folded region.

$$M_x = \pm D_{11} \times \frac{1}{r} + D_{12} \times \frac{1}{R} \tag{2.14}$$

$$M_y = D_{22} \times \frac{1}{R} \pm D_{12} \times \frac{1}{r} \tag{2.15}$$

To simplify the Equations 2.14 and 2.15, a relationship between longitudinal curvature and transverse curvature at the folded region can be obtained. For that purpose, derivation of strain energy over the fully folded area ($R\theta \times r\varphi$) with respect to radius of transverse curvature is considered and taken as zero [64].

$$U = \frac{R\theta \times r\varphi}{2}\left(\Delta\kappa_x M_x + \Delta\kappa_y M_y\right)$$

$$U = \frac{R\theta\varphi}{2}\left(D_{11} \times \frac{1}{r^2} \pm 2D_{12} \times \frac{1}{R^2} + D_{22} \times \frac{r}{R^2}\right) \tag{2.16}$$

$$\frac{dU}{dr} = -D_{11} \times \frac{1}{r^2} + D_{22} \times \frac{1}{R^2} = 0$$

$$r = \sqrt{\frac{D_{11}}{D_{22}}} R \qquad (2.17)$$

By substituting Equation 2.17 to 2.14 and 2.15, bending moment per unit width can be derived as;

$$M_x = \frac{(\pm\sqrt{D_{11}D_{22}} + D_{12})}{R} \qquad (2.18)$$

$$M_y = \frac{\left(D_{11} \pm D_{12}\sqrt{\frac{D_{22}}{D_{11}}}\right)}{R} \qquad (2.19)$$

Considering the entire fully folded region, pure bending moment that should be applied on either side of the tape-spring (M^*) can be derived from Equation 2.18:

$$M^* = M_x \times R\theta$$

$$M^* = \left(\pm\sqrt{D_{11}D_{22}} + D_{12}\right)\theta \qquad (2.20)$$

2.3.4. Experimental Investigations on Composite Tape-springs

Numerous experimental studies have investigated the behaviour of composite tape-springs. Seffen and Pellegrino [62] conducted a comprehensive study on the deployment dynamics of tape-springs, including an experimental campaign using a 200 mm-long tape-spring fabricated from annealed BeCu strip heat-treated in a furnace (see Fig. 2.20). Similarly, Zuo et al. [66] performed an experimental investigation on the moment–rotation behaviour of tape-springs made from carbon fibre composite (M40JB) (see Fig. 2.21). Both studies revealed consistent patterns in the folding behaviour of tape-springs.

In addition, Wang et al. examined the force-displacement relationship [72] and folded strain levels [73] of tape-springs manufactured using glass fibre-reinforced polypropylene. Chen et al. [69] explored the folding stability mechanics of composite tape-spring structures through experimental methods.

Among these studies, Peterson and Murphey [74] identified nonlinearity in the bending stiffness coefficients (D_{11} and D_{12}) of a laminate composed of two plies of Hexcel Hexply IM7 12K/8552 unidirectional prepreg (oriented at 0°) sandwiched between two plies of JPS AstroQuartz II Style 525 plain weave (oriented at 45°) impregnated with Patz PMT-F7 resin (see Fig. 2.22). This finding highlights that nonlinear bending stiffness can manifest in composite structures such as tape-springs as well.

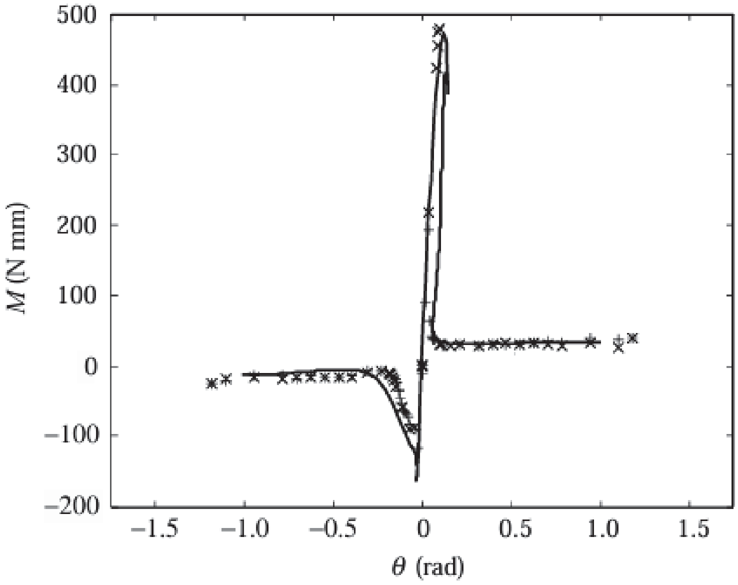

Fig. 2.20: Moment-rotation relationship of a L = 200 mm, R = 13.3 mm and θ = 106° tape-spring. Loading and unloading denoted by × and + respectively. Finite-element predictions shown by a continuous line. Adapted from [62].

2.3.5. Nonlinear Bending Stiffness of T300-1k/PMT-F4 Carbon-fibre Woven Composites

An experimental campaign was carried out by Gamage et al. [75] to quantify the bending response nonlinearity of T300-1k/PMT-F4 carbon-fibre woven composite using Column Bending Test (CBT) apparatus and Digital Image Correlation measuring technique. In the CBT, a flat shell coupon is supported by pin joints at both ends, and one joint is displaced toward the other to impose end shortening, resulting in a pure bending condition along the coupon. The test was conducted on using seven number of thin flat shell coupon with geometric properties mentioned in the Table 2.1. The results obtained from the experimental investigation can be seen in Fig. 2.23

Table 2.1: Geometric properties of thin shell coupon used for the CBT

Average width	20 mm
Average free length (l_s)	10 mm
Thickness	0.24 mm
Volume fraction of fibre (V_f)	0.62

Please note that the volume fraction of fibre (V_f) is the ratio of the volume of fibres to the total volume of the entire composite material

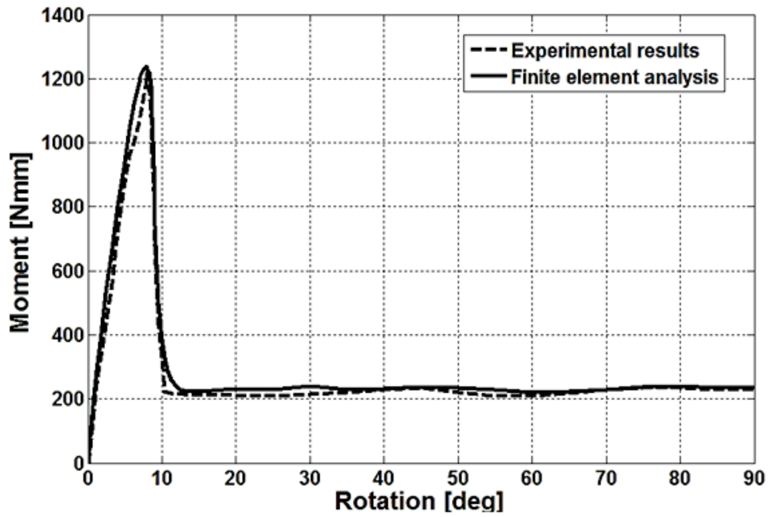

Fig. 2.21: Moment-rotation relationship the CFRP woven composite tape spring (L = 180 mm, R = 20 mm and θ = 90°). Adapted from [66].

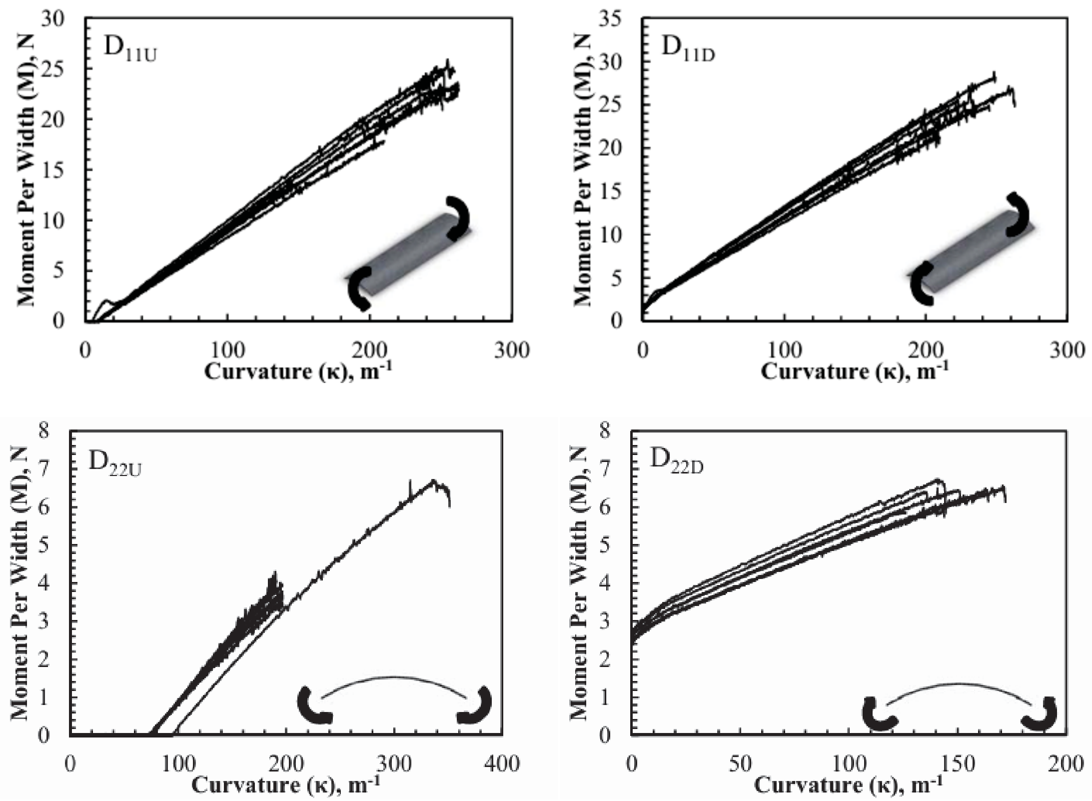

Fig. 2.22: Calculated M-κ curves for all D_{11} and D_{12} using experimental results. U stands for equal sense bending and D stands for opposite sense bending. Adapted from [74].

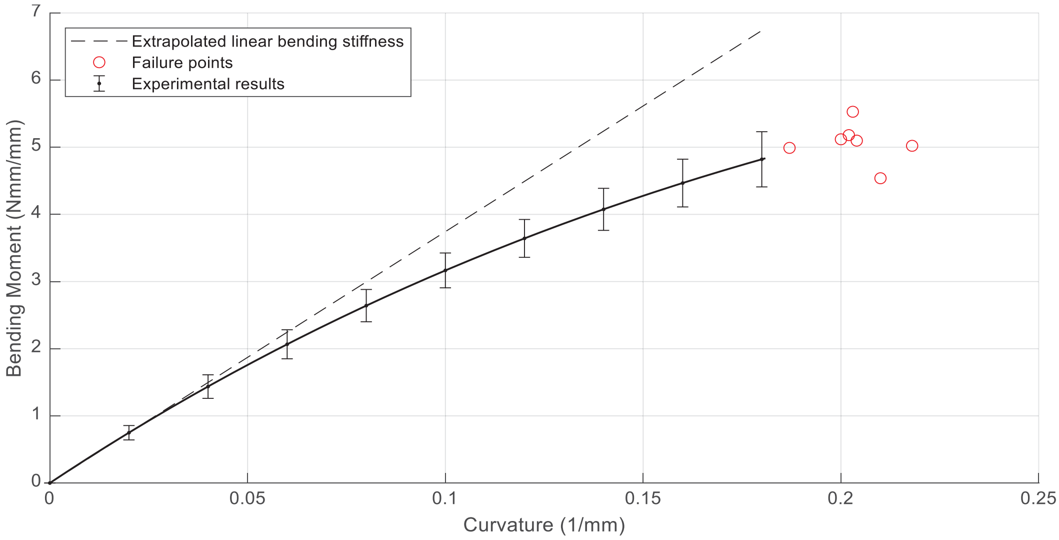

Fig. 2.23: Nonlinearity of CBT results of bending of T300-1k/PMT-F4 carbon-fibre woven composite. Adapted from [76].

CHAPTER 3

3. STIFFNESS REDUCTION MODEL FOR FLAT COMPOSITES STRUCTURES

3.1. Analytical Background of Material Nonlinearity

A nonlinearity in the elastic modulus of carbon fibres used in composite materials has been identified in several studies [32], [35], [76], and nonlinear behaviour in carbon-fibre laminates has also been observed [77]. Although various constitutive models based on analytical expressions have been proposed, as discussed in Section 2.1 and 2.2., this study adopts the empirical approach originally proposed by Van Dreumel and Kamp [32] and later modified in subsequent works [17], [78]. Equation 3.1, used in this study, was developed by these authors under the assumption that the nonlinearity in the material response is identical in both tension and compression, for the sake of simplicity.

$$E_f(\varepsilon) = E_{f,0}(1 + \gamma\varepsilon) \tag{3.1}$$

where, $E_{f,0}$ is the initial modulus of elasticity of carbon fibre and γ is a coefficient representing the nonlinearity of the modulus of elasticity. The variation in modulus of elasticity of carbon fibre, $E_f(\varepsilon)$ can be attributed to several factors, including: relative movements between tows (tow slipping), reduction in ply thickness, micro-buckling of tows, plastic behaviour of the resin, cohesive failure, material separation, and delamination, among others.

Using the above equation, Sharma et al. [17] derived Equations 3.2 and 3.3 to describe the bending moment and the bending stiffness, D_{11} of carbon-fibre unidirectional composite laminates. These equations captured the nonlinear bending response of unidirectional composites successfully.

$$M = \frac{1}{72}E_0\kappa t^3(1 + \gamma\varepsilon)\sqrt{36 - 3t^2\kappa^2\gamma^2} \tag{3.2}$$

$$D_{11} = \frac{E_0 t^3(6 - t^2\gamma^2\kappa^2)}{12\sqrt{36 - 3t^2\kappa^2\gamma^2}} \tag{3.3}$$

Since Equation 3.2 and 3.3 incorporate bending stiffness nonlinearity and have previously shown good agreement for unidirectional composite laminates, these analytical expressions were applied to woven composite laminates to assess the accuracy of a stand-alone analytical approach in predicting the nonlinear bending response. This evaluation was based on the experimental investigation by Gamage et al. [75] on carbon-fibre (T300-1k/PMT-F4) woven composites. The material properties of the T300-1k/PMT-F4 woven composite reported in [75] are summarised in Table 3.1.

Table 3.1: Material properties of T300-1k/PMT-F4 woven composite

Volume fraction *($V_{f,tow}$)*	0.62
Elastic modulus of tows in 1 direction *($E_{1,tow}$)*	145 920 N/mm^2
Elastic modulus of tows in 2 & 3 direction *($E_{2,tow} = E_{3,tow}$)*	11 132 N/mm^2
Elastic modulus of resin *($E_{1,resin} = E_{2,resin} = E_{3,resin}$)*	3833 N/mm^2

The thickness of a single tow is 0.06 mm. One laminate consists of two tows, and the composite is made up of two laminates in total. However, due to manufacturing imperfections and the effect of phase angle, the average thickness of the coupon was assumed to be 0.21 mm. The homogenised initial elastic modulus of the composite was calculated using Equation 3.4, while Equation 3.3 was used to determine the initial bending stiffness, D_{11}.

$$E_0 = \left(E_{1,tow} + E_{2,tow}\right)\frac{V_{f,tow}}{2} + E_{resin}(1 - V_{f,tow}) \qquad (3.4)$$

The calculated values were:

$$E_0 = 50\ 142.7\ \mathrm{N/mm^2}$$

$$D_{11,0} = 38.69\ \mathrm{N/mm^2}$$

Fig. 3.1. illustrates the bending moment responses for different γ coefficients using the above-calculated material properties. As shown, even the curve corresponding to $\gamma = 60$ does not capture the experimentally observed nonlinear bending response. However, values reported in the literature for T300 fibres are $\gamma_T = 13$ in tension [78] and $\gamma_c = 8$ in compression [79]. This demonstrates that analytical approaches alone cannot fully capture the effect of stiffness nonlinearity in carbon-fibre woven composites. Therefore, it is essential to adopt numerical methods for investigating their nonlinear bending response.

3.2. Multi-scale Modelling Approach

As described in Section 2.2.2.2, numerous studies have utilised multi-scale homogenised models to predict the nonlinear behaviour of woven composites [10], [24], [55]. In parallel, several other studies have employed user-defined subroutines with finite element solvers to incorporate material nonlinearities in various forms [19], [20], [21], [23], [24], [26], [55]. However, none of these studies specifically addressed the nonlinear bending response of composite structures. To bridge this gap, the present study adopts a synchronised multi-scale modelling approach in combination with a User-Defined General Section (UGENS) subroutine to accurately capture the nonlinear bending behaviour of woven composite structures.

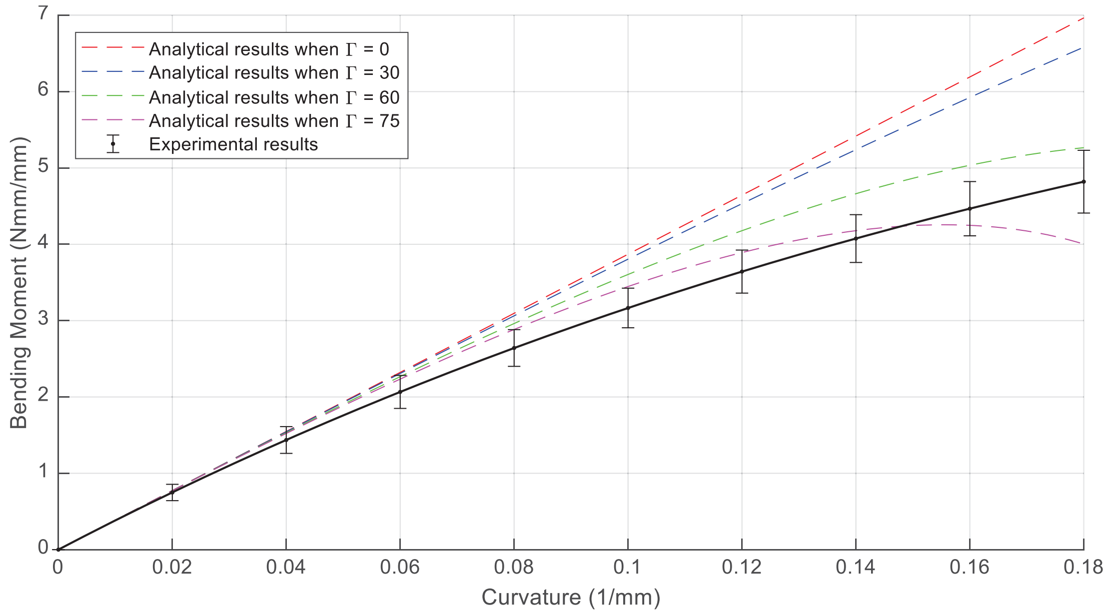

Fig. 3.1: Comparison between experimental and analytical results of the bending moment response for different γ values

3.2.1. Multi-Scale Modelling Framework and Numerical Implementation

Modelling a composite structure from the fibre, matrix, and interfacial (fibre–matrix) levels up to the structural scale can be computationally expensive and difficult to debug, especially for structures undergoing large deformations. Therefore, multi-scale homogenisation is commonly adopted. This approach establishes hierarchical modelling layers, micro-, meso-, and macro-scales, where stiffness properties and stress tensors are transferred upwards (from micro- to macro-scale), while strains and deformations are passed downwards (macro- to micro-scale), a process referred to as localisation [10]. As shown in Fig. 3.2, the framework adopted in this study uses only the meso-scale and macro-scale models for efficiency.

Material properties for the meso-scale model were obtained through analytical and empirical relations presented in Gamage et al. [75]. The macro-scale model, based on Classical Beam Theory, provides the deformation gradient to the meso-scale Representative Unit Cell (RUC), from which the corresponding constitutive tensor is extracted. In this process, the meso-model first computes the local strain tensor from the deformation gradient and then determines the corresponding ABD stiffness matrix incorporating material nonlinearity and progressive damage [75].

The computed constitutive tensor is then passed back to the macro-scale model via the UGENS subroutine. This enables the macro-model to compute stress and force vectors with improved accuracy, thereby capturing the nonlinear bending response. To reduce computational costs, constitutive tensors corresponding to a range of deformation gradients, which is from zero to 0.18 of curvature, are precomputed and stored. During the simulation, the macro-scale model accesses these stored tensors through UGENS, avoiding the need to run the meso-model at every increment.

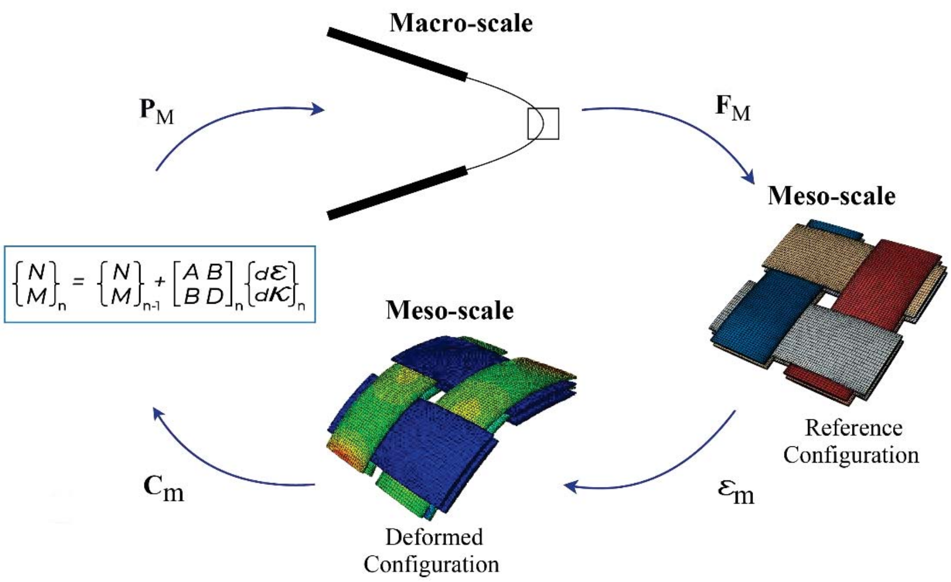

Fig. 3.2: Multi-scale modelling approach framework. FM, ϵm, Cm and PM stand for macro-scale deformation gradient, meso-scale finite strain tensor, meso-scale material constitutive tensor and macro-scale finite stress vector, respectively.

3.2.2. Meso-scale Numerical Model and Validation

A previously developed and experimentally validated in-house RUC model was adopted in this study. The meso-scale model was developed for the carbon-fibre woven composite used in the column bending test (CBT), comprising T300-1k fibres and PMT-F4 epoxy resin. The laminate architecture was characterised using X-ray computed tomography (XRCT) (see Fig. 3.3), and the RUC model was constructed using TexGen, a finite element pre-processor designed for textile composites. Detailed information regarding the geometry, material properties, interfacial cohesion, boundary conditions, and load application can be found in Gamage et al. [75].

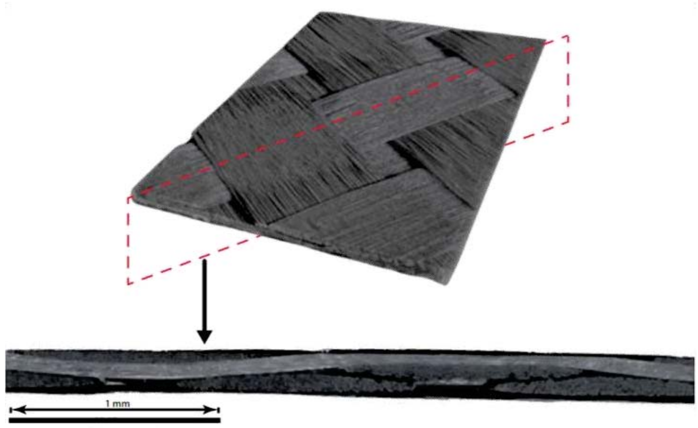

Fig. 3.3: XRCT scans of the woven composite

The model incorporates material nonlinearity due to contact-related phenomena such as tow separation and matrix-tow debonding by defining precise contact interactions. Additionally, the nonlinearity in the in-plane elastic modulus (E_{11} and E_{22}) is implemented using a modified form of Equation 3.1, adapted from Sharma et al. [28], shown below as Equation 3.5:

$$E_c = \begin{cases} E_{cC} = E_0\,(1 + \gamma_{1C}\,\varepsilon)\,V_f + E_m\big(1 - V_f\big),\ 0 < \varepsilon \\ E_{cT} = E_0\,(1 + \gamma_{1T}\,\varepsilon)\,V_f + E_m\big(1 - V_f\big),\ 0 \geq \varepsilon \end{cases} \tag{3.5}$$

The variation of E_{11} used in the study is illustrated in Fig. 3.4.

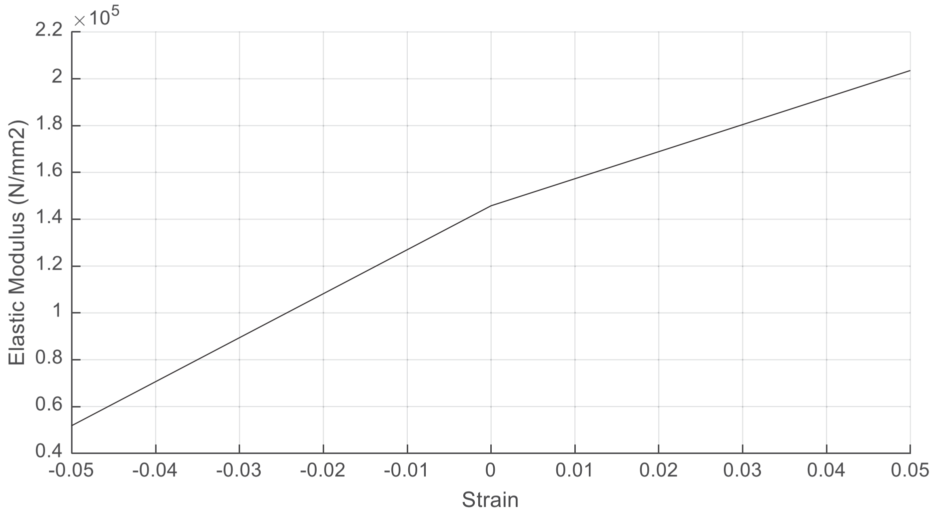

Fig. 3.4: Variation of E_{11} and E_{22} with respect to strain in a tow of the RUC model

The RUC model was validated against the CBT model by comparing the moment–curvature response, as shown in Fig. 3.5. Once validated, the RUC was used to extract the bending stiffness components, D_{11} and D_{12} across different curvature values (see Fig. 3.6). It is important to note that the $[B]$ matrix is zero due to identical fibre orientation in each ply, and for orthogonal woven composites, $D_{11} = D_{22}$.

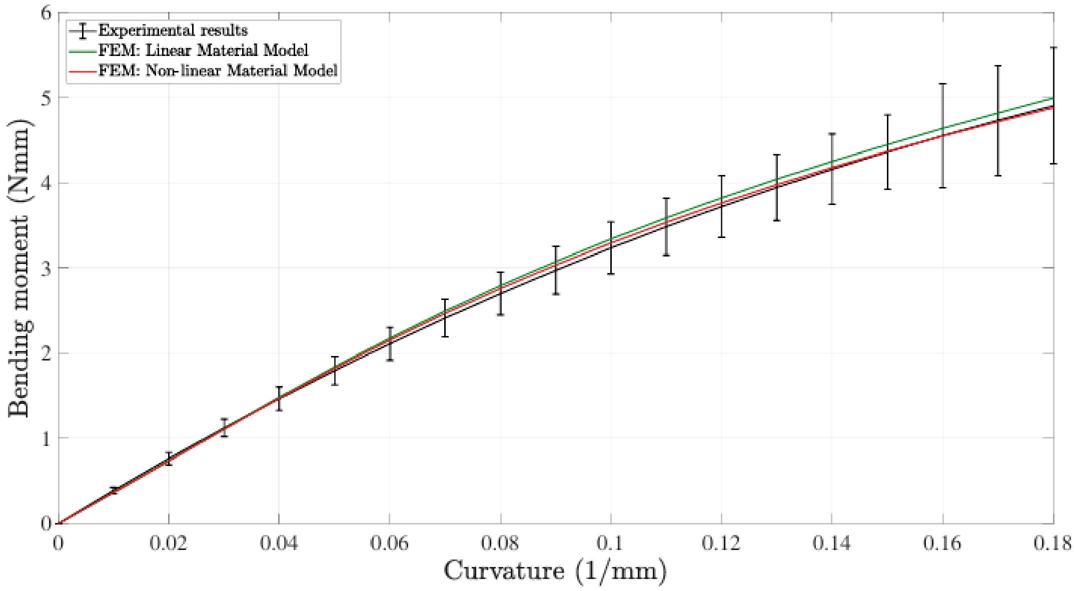

Fig. 3.5: Comparison between experimental and numerical results RUC model. Adapted from [75].

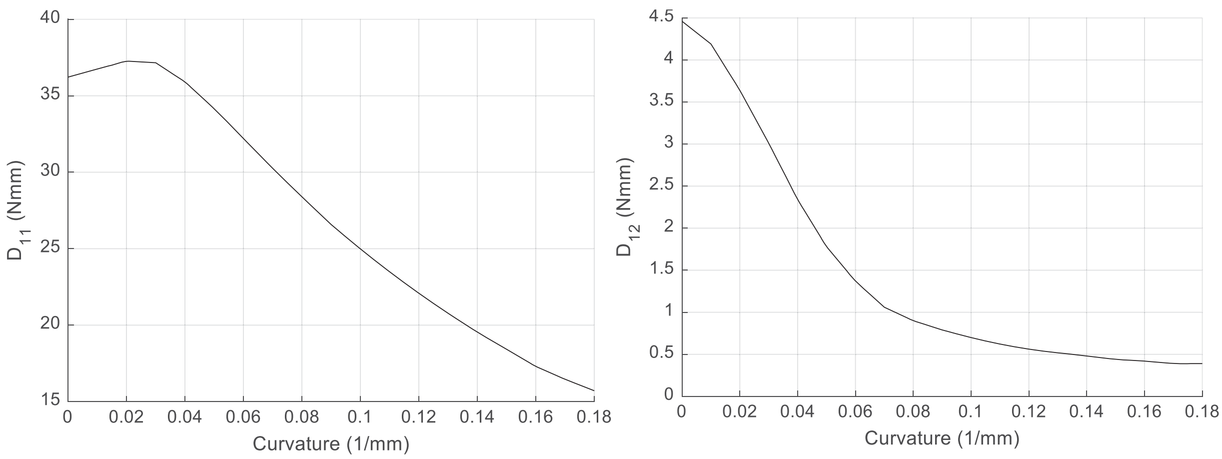

Fig. 3.6: Variation of D_{11} and D_{12} stiffnesses over the curvature obtained from validated meso-scale RUC model

3.3. Numerical Modelling of the Flat Thin Woven Carbon-fibre Composite

3.3.1. Numerical Simulation

As the next step in the multi-scale modelling framework, a macro-scale model was developed to simulate the CBT and to validate the structural behaviour at the macro-level. The same geometry as that of the CBT coupon was adopted (see Table 3.2), and the shell section was defined using the general shell stiffness formulation presented in Equation 3.6 [75]. The ABD stiffness matrix, derived from the validated meso-scale model, was used as the section input. In particular, the curvature-dependent bending stiffness components (D_{11} and D_{12}) were provided through the User-Defined General Section (UGENS) subroutine.

Table 3.2: Section properties of the shell coupon

Width ($\boldsymbol{w_s}$)	20 mm
Free length ($\boldsymbol{l_s}$)	10 mm
Density	1760 kgm^{-3} (0.279 kgm^{-2})

$$\begin{bmatrix} 8493 & 2195 & 0 & 0 & 0 & 0 \\ 2195 & 8493 & 0 & 0 & 0 & 0 \\ 0 & 0 & 370 & 0 & 0 & 0 \\ 0 & 0 & 0 & 36.5 & 4.7 & 0 \\ 0 & 0 & 0 & 4.7 & 36.5 & 0 \\ 0 & 0 & 0 & 0 & 0 & 1.8 \end{bmatrix} \tag{3.6}$$

A schematic diagram of the shell coupon model and its numerical implementation is shown in Fig. 3.7. Two reference points were defined on the top and bottom surfaces, with coupling constraints applied to all six degrees of freedom (DOFs) for the top and bottom edges, respectively. All DOFs were restrained except for rotation about the x-axis. A displacement boundary condition was applied to the top reference point in the negative *y*-direction to simulate the bending moment.

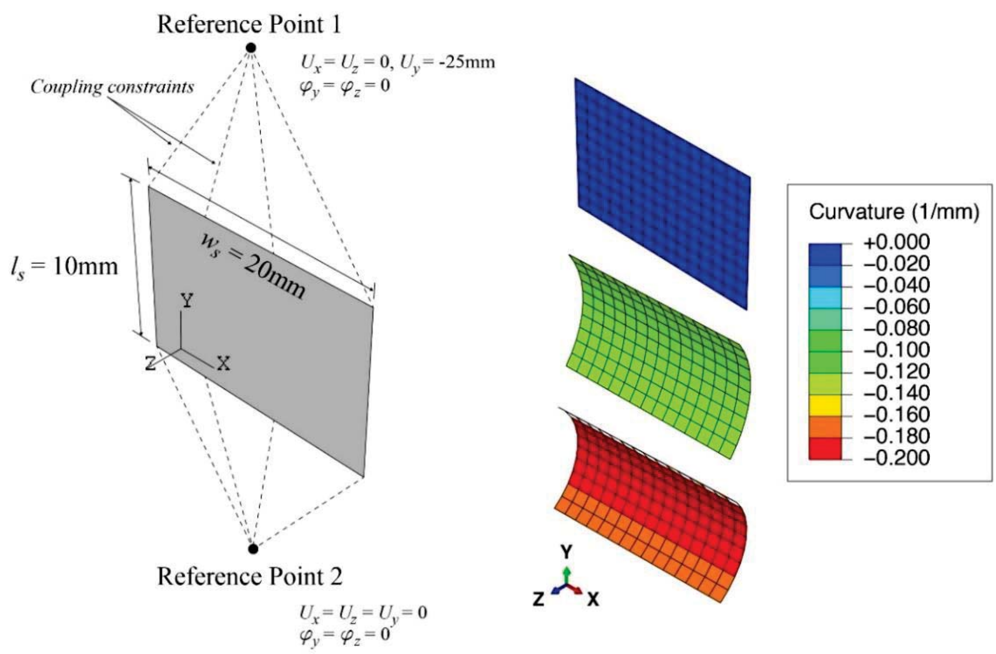

Fig. 3.7: Schematic of the flat shell coupon model and its deformation

3.3.2. Analytical Background of Macro-scale Model

The UGENS subroutine was developed based on the analytical equations proposed by Tibiei and Jiang [21]. i refers to any element of the stress or strain vector, or the constitutive stiffness tensor. n denotes the increment number. $d\{\sigma_i\}_n$ is the incremental stress and $d\{\varepsilon_i\}_n$ is the incremental strain at n^{th} increment.

The stress update equations are given by:

$$\{\sigma_i\}_n = \{\sigma_i\}_{n-1} + d\{\sigma_i\}_n \tag{3.7}$$

$$d\{\sigma_i\}_n = \{C_i\}_n \times d\{\varepsilon_i\}_n \tag{3.8}$$

$$d\{\varepsilon_i\}_n = \{\varepsilon_i\}_n - \{\varepsilon_i\}_{n-1} \tag{3.9}$$

Combining these equations, the stress at increment n is calculated as:

$$\{\sigma_i\}_n = \{\sigma_i\}_{n-1} + \{C_i\}_n \times d\{\varepsilon_i\}_n \tag{3.10}$$

Fig. 3.8 illustrates how the stress vector is updated at each increment within the finite element solver.

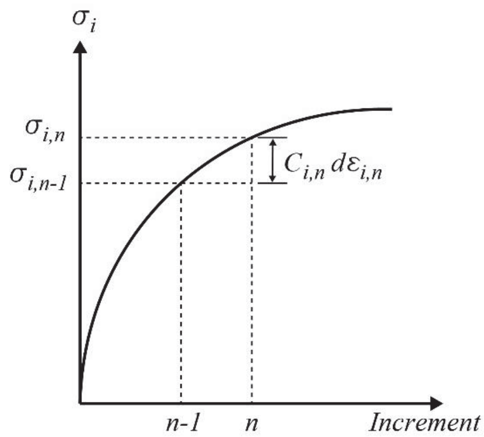

Fig. 3.8: Nonlinearity of stress vector

3.3.3. Implementation of the UGENS Subroutine

In ABAQUS/Standard, the UGENS subroutine is called at every integration point during each iteration of every increment. The subroutine receives the section state at the start of the increment, including forces, moments per unit width, and generalised strains, along with the strain increment and time increment. UGENS then updates the internal force vector and solution-dependent state variables, and returns the updated section stiffness matrix [80].

It should be noted that, the formulation of a constitutive model in Abaqus, is based on the assumption that the material response at any given point is governed solely by local effects, independent of the behaviour of surrounding points. Consequently, each spatial integration point within the finite element mesh can be evaluated and updated individually. In the implicit solver (ABAQUS/Standard), the solution procedure requires the consistent stiffness matrix to be accurately defined in order to form the Jacobian of the non-linear equilibrium equations. Therefore, updating the material state independently at each integration point does not compromise the accuracy or stability of the global numerical solution.

To activate the UGENS subroutine, the input file of the numerical model must include a *SHELL GENERAL SECTION* block. In this study, 21 stiffness properties and 52 solution-dependent state variables were defined (see Appendix – A: Section Block of the Input File Used to Call the UGENS Subroutine). The thickness must also be explicitly provided, unlike simulations without the subroutine. The shell thickness was calculated using ABAQUS's default equation [80]:

$$t = \sqrt{12\frac{D_{44} + D_{55} + D_{66}}{D_{11} + D_{22} + D_{33}}} \tag{3.11}$$

Therefore, thickness of the coupon is given as 0.227 mm.

Transverse shear stiffnesses were similarly defined based on [80]:

$$K_{11} = K_{22} = \frac{1}{6}(D_{11} + D_{22}) + \frac{1}{3}D_{33} \tag{3.12}$$

$$K_{12} = 0 \tag{3.13}$$

This yielded: $K_{11} = K_{22} = 2954.33$ Nm and $K_{12} = 0$.

3.3.4. Functionality of the UGENS Subroutine

The UGENS subroutine was programmed to update the stiffness tensor, force vector, and solution-dependent state variables after each increment. Since the primary interest in this study is the nonlinear bending-curvature response, only the bending moment components and bending stiffness terms of the ABD matrix are updated.

3.3.4.1. Implementation of Nonlinear Stiffness Variation via the UGENS Subroutine

The subroutine framework is illustrated in Fig. 3.9. For each curvature value obtained from the ABAQUS solver, the corresponding stiffness parameters $D_{11}$and D_{12} are retrieved from a precomputed dataset. To ensure a continuous variation of stiffness, an interpolation scheme for $D_{11}$and D_{12} is implemented within the UGENS subroutine. At each increment, the current curvature values are extracted from the simulation, and the nearest higher and lower curvature values in the dataset are identified. The corresponding $D_{11}$and D_{12} values are then obtained and interpolated to determine the effective stiffness for that increment. The overall procedure is illustrated in Fig. 3.10. Subsequently, the Jacobian stiffness matrix is updated using these interpolated stiffness parameters.

These updated values are then used to compute the bending moments, while updating the Jacobian matrix (ddndde), allowing the macro-scale model to exhibit the actual nonlinear bending response. It is recommended to maintain the symmetricity of the stiffness matrix for higher computational efficiency.

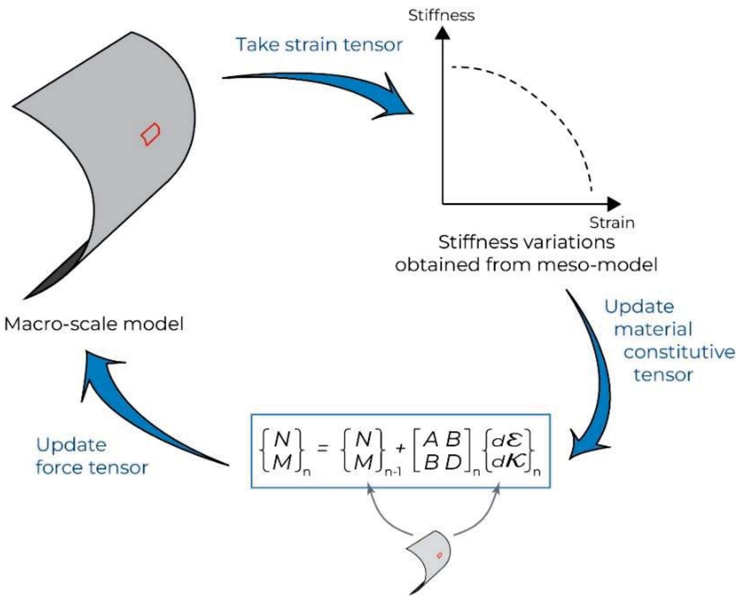

Fig. 3.9: Framework of the UGENS subroutine

The updated bending moment components per unit width are calculated using the following equations, adapted from Equation 3.10:

$$M_{1,n} = M_{1,n-1} + \{D_{11,n}\} \times d\kappa_{1,n} + \{D_{12,n}\} \times d\kappa_{2,n} \quad (3.14)$$

$$M_{2,n} = M_{2,n-1} + \{D_{11,n}\} \times d\kappa_{2,n} + \{D_{12,n}\} \times d\kappa_{1,n} \quad (3.15)$$

This approach ensures that the bending moment-curvature response of the shell model accurately reflects the nonlinear stiffness behaviour of the composite material, as defined by the meso-scale model.

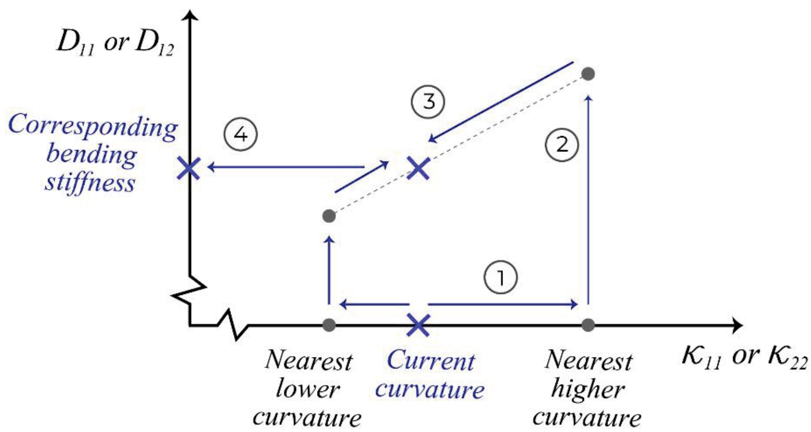

Fig. 3.10: Identification of corresponding D_{11} and D_{12} values for a given curvature

3.3.4.2. Extraction of Energy Components Using the UGENS Subroutine

When the UGENS subroutine is used in Abaqus, the program no longer employs its built-in material law or energy integration scheme. Instead, the user directly defines the element stiffness matrix and internal force vector, while Abaqus itself has no stored strain-energy potential to derive work or internal energy from. Consequently, energy quantities such as strain energy (*SSE*) and internal energy (*ALLIE*) are not automatically calculated and may appear unrealistically low even though the stiffness response and moment–curvature relationship are correct. To obtain meaningful energy outputs, the strain energy must be explicitly computed within the subroutine, typically as $SSE = 0.5\,\mathrm{F} \cdot \varepsilon$ for each element covering the entire area of the structure, so that Abaqus can include it in the overall energy balance and ensure consistency between the applied loads, internal forces, and reported energy terms.

The complete UGENS subroutine code is provided in Appendix – B: UGENS Subroutine for reference.

3.4. Numerical Results and Discussion

3.4.1. Results of Flat Shell Coupon Model (CBT)

Although both D_{11} and D_{12} components were updated in the flat shell coupon model, only uniaxial bending was applied, and the coupon width was sufficiently large such that the resulting κ_2 (curvature in the transverse direction) was negligible. Therefore, the analysis focused on comparing the numerical $M_1 - \kappa_1$ response (bending moment per unit width vs. curvature) of a mid-region element with the corresponding experimental results, as shown in Fig. 3.11.

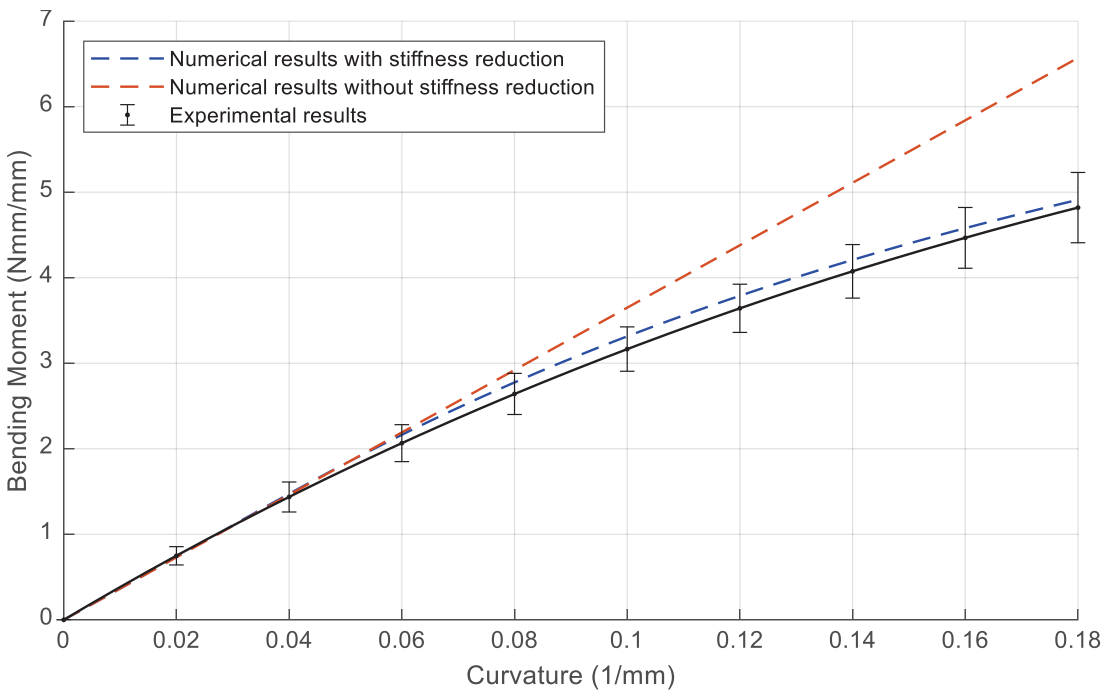

Fig. 3.11: Comparison of numerical results with experimental results

As depicted in Fig. 3.11, the proposed numerical framework incorporating the UGENS subroutine successfully reproduces the nonlinear moment–curvature response. In contrast, the model without the subroutine exhibits a purely linear behaviour, indicating that the nonlinearity is introduced by the curvature-dependent stiffness update implemented through UGENS. This confirms that the developed UGENS subroutine can apply element-wise stiffness variation as a function of curvature within the macro-scale model, as demonstrated here for a flat shell configuration.

3.4.2. Results of Long Narrow Shell Coupon Model

To further examine the impact of bending stiffness reduction, an additional narrow shell coupon was simulated with and without the use of the UGENS subroutine. The material properties were consistent with those discussed in Section Results of Flat Shell Coupon Model (CBT)3.4.1, and the section properties used in this simulation are provided in Table 3.3. The deformed shape of the model is shown in Fig. 3.12.

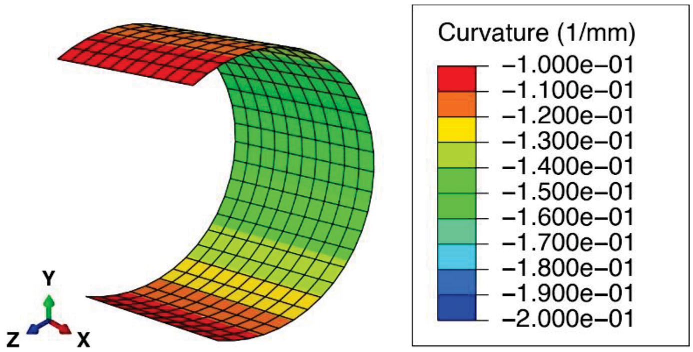

Fig. 3.12: Deformed narrow flat shell model

Table 3.3: Section properties of long narrow shell section

Width	10 mm
Free length (ls)	30 mm

As shown in Fig. 3.13, the influence of the UGENS subroutine is clearly evident. Similar to the results observed in Fig. 3.11, the model without the subroutine maintains a constant bending stiffness and fails to capture any nonlinearity. In contrast, the model with the subroutine effectively demonstrates nonlinear bending behaviour, affirming that the curvature-dependent stiffness properties embedded via UGENS are responsible for this realistic response.

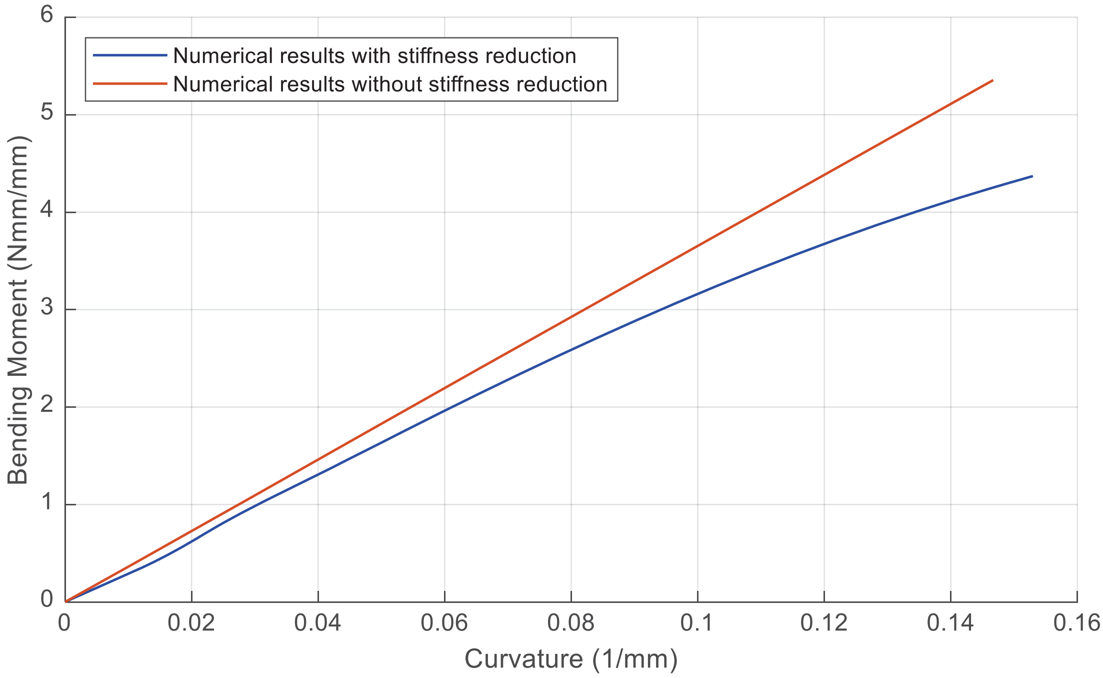

Fig. 3.13: Comparison of numerical results of narrow shell coupon with and without stiffness reduction

CHAPTER 4

4. STIFFNESS REDUCTION MODEL FOR SINGLY CURVED COMPOSITE STRUCTURES WITH BIFURCATIONS

4.1. Numerical Modelling of the Tape-spring Structures

Since the application of stiffness reduction has been validated for flat shell coupons using experimental results, this study extends the analysis to a tape-spring composite structure, which features single curvature and undergoes highly nonlinear bifurcations during snap-through events in folding and deployment. The analytical background of tape-spring mechanics has been discussed in Section Mechanics of Composite Tape-springs2.3.3. It is important to note that while nonlinear bending stiffness reduction in tape-springs has been reported in the literature [74], its influence on the overall bending behaviour during folding and deployment has not yet been quantitatively assessed.

4.1.1. Numerical Modelling Technique

A schematic diagram of the tape-spring model is presented in Fig. 4.1. For demonstration purposes, a tape-spring with a radius of 15 mm, a subtended angle of 100°, and a total length of 300 mm is considered. Two reference points (RP_1 and RP_2) are defined at either end of the tape-spring cross-section, with coupling constraints applied to all six degrees of freedom (DoFs). To ensure the application of a pure bending moment, an equation constraint (Equation 4.1) is defined between RP_1, RP_2, and a third reference point (RP_3) positioned externally to the tape-spring.

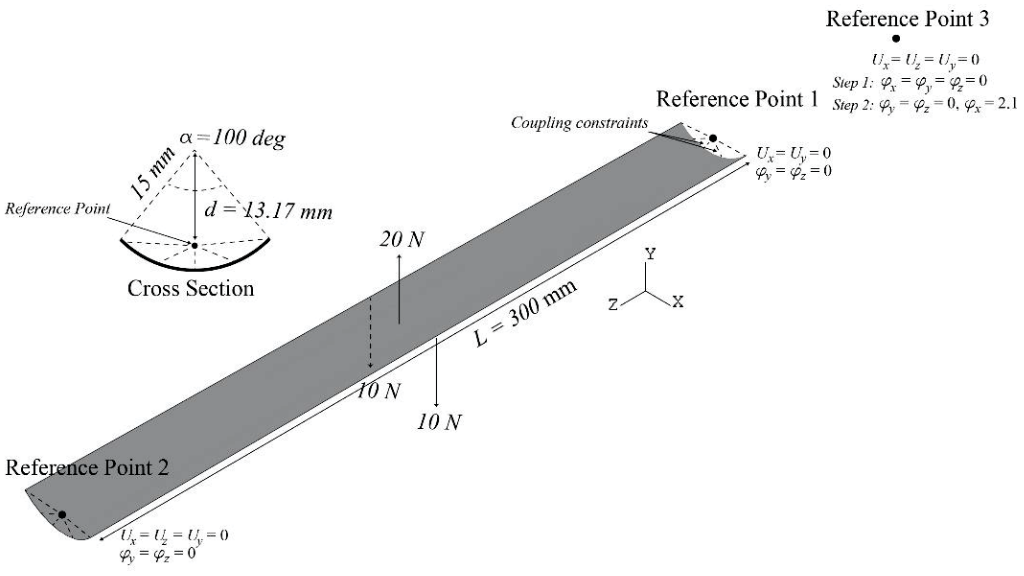

Fig. 4.1: Schematic diagram of the tape-spring model

$$\mathrm{RP}_3 = \mathrm{RP}_2 - \mathrm{RP}_1 \quad (4.1)$$

RP_1 and RP_2 are located at the centroid of the tape-spring cross-section. The perpendicular distance between the centre of curvature and each reference point is denoted by d, which is defined by Equation 4.2.

$$d = \frac{R \sin\left(\frac{\alpha}{2}\right)}{\frac{\alpha}{2}_{rad}} \quad (4.2)$$

The *dynamic-implicit* solver in ABAQUS/Standard finite element software was employed for this analysis. The general shell stiffness formulation was used to define the tape-spring section, with the same stiffness matrix previously applied to the flat shell coupon (see Equation 3.6). Various tape-spring cross-sections were considered in this study, and their section properties are listed in Table 4.1. Although the thickness is not explicitly specified, as discussed in Section 3.3.3, ABAQUS/Standard calculates it automatically using Equation 3.11, resulting in a thickness value of 0.227 mm.

Table 4.1: Section properties of tape-spring models

Transverse Radius, $\boldsymbol{R}$ (mm)	10, 12.5, 15, 17.5, 20
Length, $\boldsymbol{L}$ (mm) (20× $\boldsymbol{R}$)	200, 250, 300, 350, 400
Subtended Angle, $\boldsymbol{\alpha}$ (°)	80, 90, 100, 110, 120
Density	1760 kgm^{-3} (0.279 kgm^{-2})

The boundary conditions used in the simulation are illustrated in Fig. 4.1. RP_1 was assigned a pinned condition, while RP_2 was assigned a roller support, allowing movement along one axis. A pinching force was applied during Step 1 (0–50 s) to flatten the tape-spring, simulating the folding phase. In Step 2 (50–350 s), a rotational displacement about the x-axis was applied to initiate and control the deployment process. The complete load application setup is illustrated in Fig. 4.2, while the corresponding deformed shape of the numerical model is presented in Fig. 4.3.

4.1.2. Sensitivity Analysis

A mesh sensitivity analysis was conducted to determine the optimum element size for the numerical model of the tape-spring. The evaluation was based on the comparison between the longitudinal and transverse radii of curvature in the fully folded region. Due to the orthotropic nature of the woven composite, the bending stiffness values D_{11} and D_{22} are equal. According to Equation 2.17, this implies that the longitudinal and transverse radii of curvature should also be equal in the fully folded state. Furthermore, as the fully folded region approximates a cylindrical shape, both radii of curvature should correspond to the transverse radius of the tape-spring.

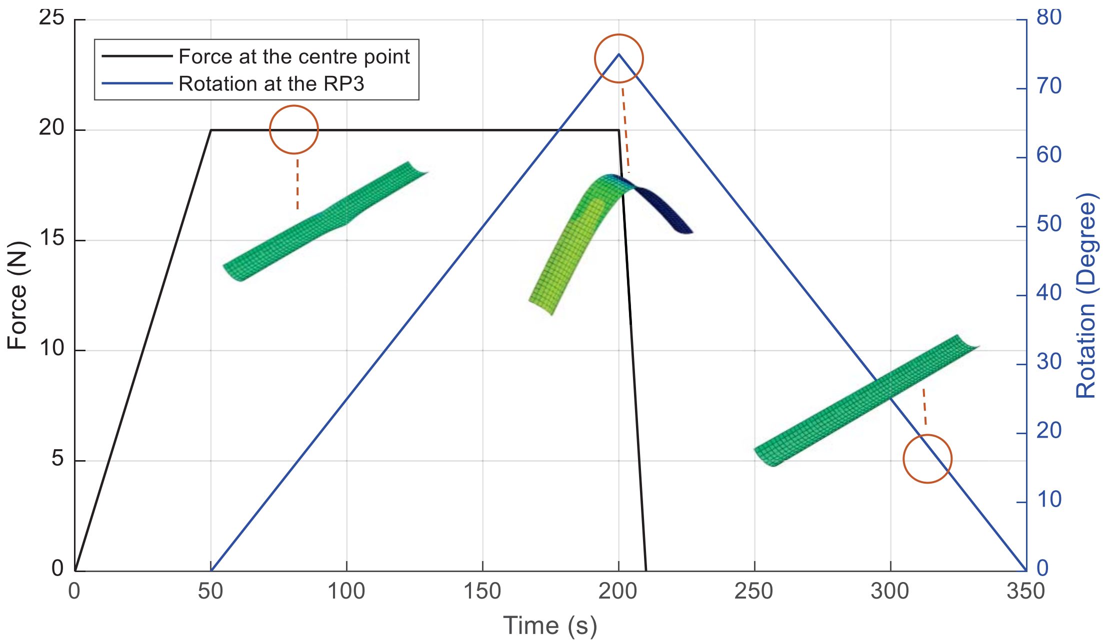

Fig. 4.2: Load arrangement of the numerical model

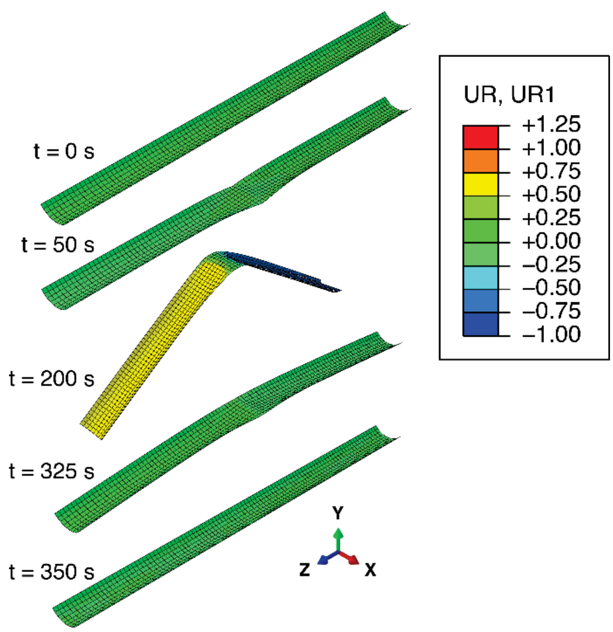

Fig. 4.3: Rotation of tape-spring for different time steps ($R = 15$ mm, $\alpha = 100°$)

For this analysis, a tape-spring model with a 15 mm radius and a subtended angle of 100° was used. Only the deployment phase of the tape-spring, from the maximum folded rotation (≈ 75°) to the snap-back rotation (≈ 35°), is considered, as a fully folded region no longer exists after the snap-back. The simulation results are shown in Fig. 4.4.

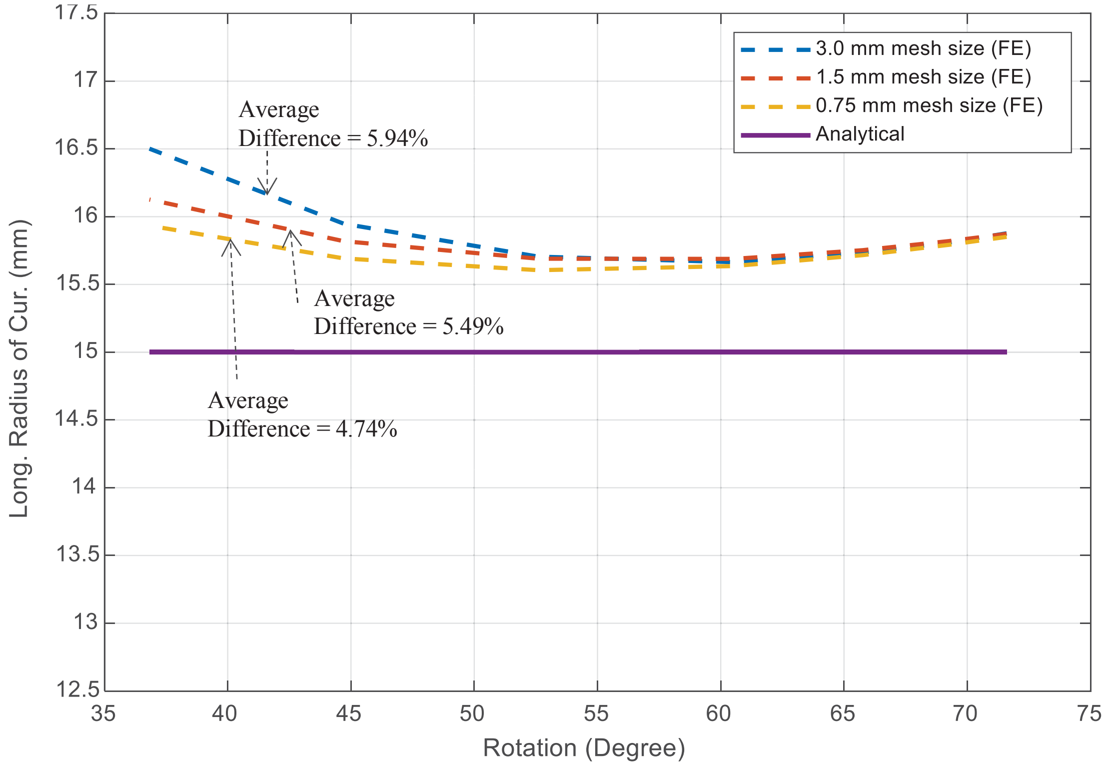

Fig. 4.4: Comparison of longitudinal radius of curvatures of different mesh sizes from the maximum folded rotation to the snap-back rotation ($R = 15$ mm, $\alpha = 100°$)

The results indicate that finer mesh sizes produce curvature values that more closely match the theoretical predictions. However, considering the balance between computational efficiency and accuracy, a mesh size of 0.75 mm was selected. This mesh size offers sufficient accuracy while significantly reducing computational cost. Notably, this corresponds to a mesh size equal to $1/20$ of the transverse radius.

4.1.3. Damping Coefficients for the Model

To minimise dynamic effects during the highly nonlinear bifurcations that occur during tape-spring deployment, Rayleigh damping coefficients were introduced into the numerical model. Since the analysis was carried out using a dynamic-implicit solver in ABAQUS/Standard, viscous damping was not available. Furthermore, the use of general shell stiffness prevented the application of conventional material damping. Therefore, Rayleigh damping, defined through the parameters α_0 (mass proportional) and β_0 (stiffness proportional), was employed to stabilise the simulation.

To determine appropriate values for α_0 and β_0, two dominant natural frequencies of the system, ω_1 and ω_2, were identified through a modal analysis performed for each tape-spring configuration. The first mode (ω_1), was selected to represent low-frequency behaviour, while a higher mode (ω_2) that captures more than 90% of the effective modal mass was chosen to represent high-frequency response. A damping ratio of 5% ($\xi_1 = \xi_2 = 0.05$) was assumed for both frequencies, which lies within the range typically reported for fibre-reinforced composite structures [81], [82]. Using the standard Rayleigh damping formulation (Equation 4.3), values for α_0 and β_0 were derived using Equations 4.4 and 4.5. The calculated natural frequencies and corresponding damping coefficients for each model are summarised in Table 4.2.

$$\xi = \frac{1}{2}\left(\frac{\alpha_0}{\omega} + \beta_0\omega\right) \tag{4.3}$$

$$\beta_0 = \frac{2(\xi_2\omega_2 - \xi_1\omega_1)}{\omega_2^2 - \omega_1^2} \tag{4.4}$$

$$\alpha_0 = 2\xi_2\omega_2 - \beta_0\omega_2^2 \tag{4.5}$$

Table 4.2: Damping coefficients used for tape-spring models

Radius (mm)	**Subtended Angle (°)**	$\boldsymbol{\omega_1(rad^{-1})}$	$\boldsymbol{\omega_2(rad^{-1})}$	$\boldsymbol{\alpha_0}$	$\boldsymbol{\beta_0}$
10	80	28.86	237.82	2.58	3.64×10^{-4}
	100	34.97	340.23	3.18	2.61×10^{-4}
	120	45.22	538.80	4.18	1.69×10^{-4}
15	80	16.28	156.98	1.48	5.65×10^{-4}
	100	21.54	322.67	2.02	2.88×10^{-4}
	120	29.17	350.77	2.70	2.60×10^{-4}
20	80	11.18	237.85	1.07	4.00×10^{-4}
	100	15.69	227.68	1.47	4.07×10^{-4}
	120	21.61	255.29	1.99	3.56×10^{-4}

To evaluate the influence of Rayleigh damping on the overall bending response, a comparative simulation was conducted for a 10 mm radius tape-spring with an 80° subtended angle, both with and without damping. This particular geometry was chosen because it is capable of demonstrating snap-through behaviour while maintaining numerical stability in the absence of damping. Models with larger radii and subtended angles failed to replicate this behaviour without introducing significant dynamic effects. The results, shown in Fig. 4.5 , indicate that Rayleigh damping has no effect on the bending moment–rotation relationship, other than reducing the oscillatory dynamic effects during deployment.

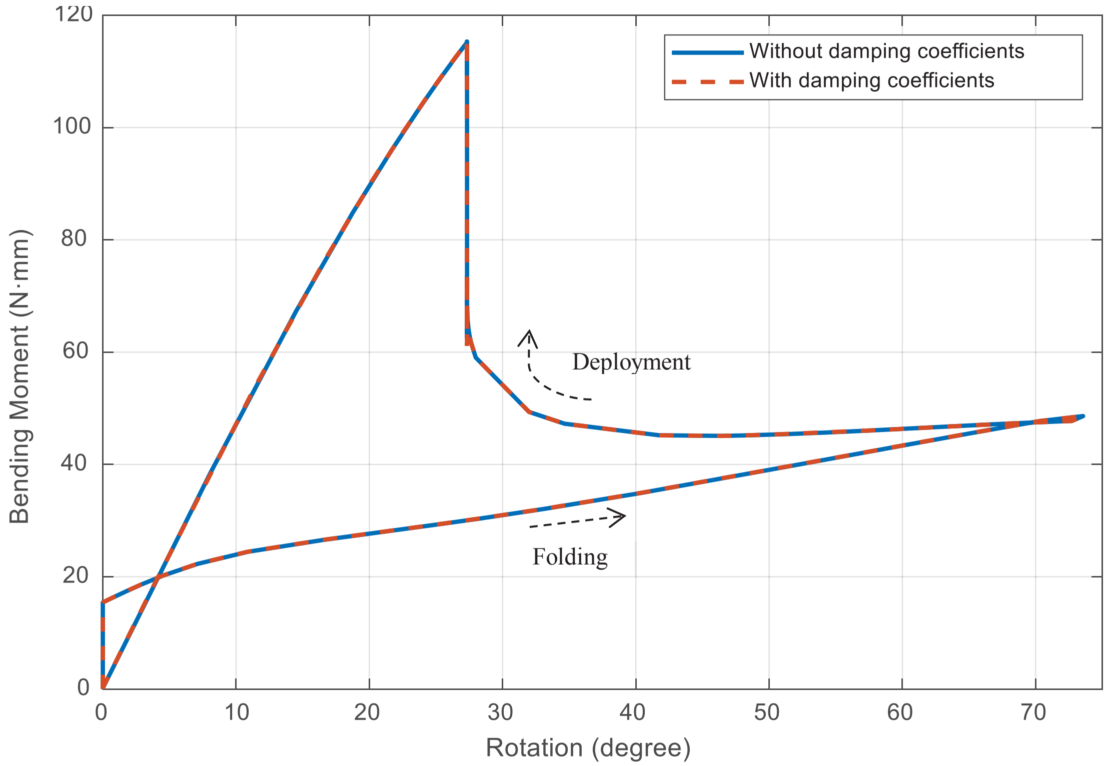

Fig. 4.5: Bending moment - rotation relationship of the tape-spring model ($R = 10$ mm, $\alpha = 80°$)

4.1.4. Effect of the Tape-spring Length

Furthermore, the impact of stiffness reduction was investigated across tape-spring models of varying lengths. The selected lengths were chosen to exceed the ploy region, the localized area where the tape's geometry changes significantly from the fully folded state to the deployed configuration [69], [73]. As shown in Fig. 4.6 and Fig. 4.7, the steady-state bending moments remain unaffected by variations in tape-spring length. However, the peak bending moments are influenced by length, demonstrating the effect of slenderness on the structural response. Interestingly, for a tape-spring length of 200 mm, the peak moment is not affected by the incorporation of bending stiffness nonlinearity, as illustrated in Fig. 4.7.

It is important to note that tape-spring length was considered in terms of a normalised length-to-radius ratio (length / transverse radius), which was kept constant across all tape-spring models. This approach ensured that the influence of slenderness on the results was minimised, allowing for a more focused evaluation of stiffness reduction effects.

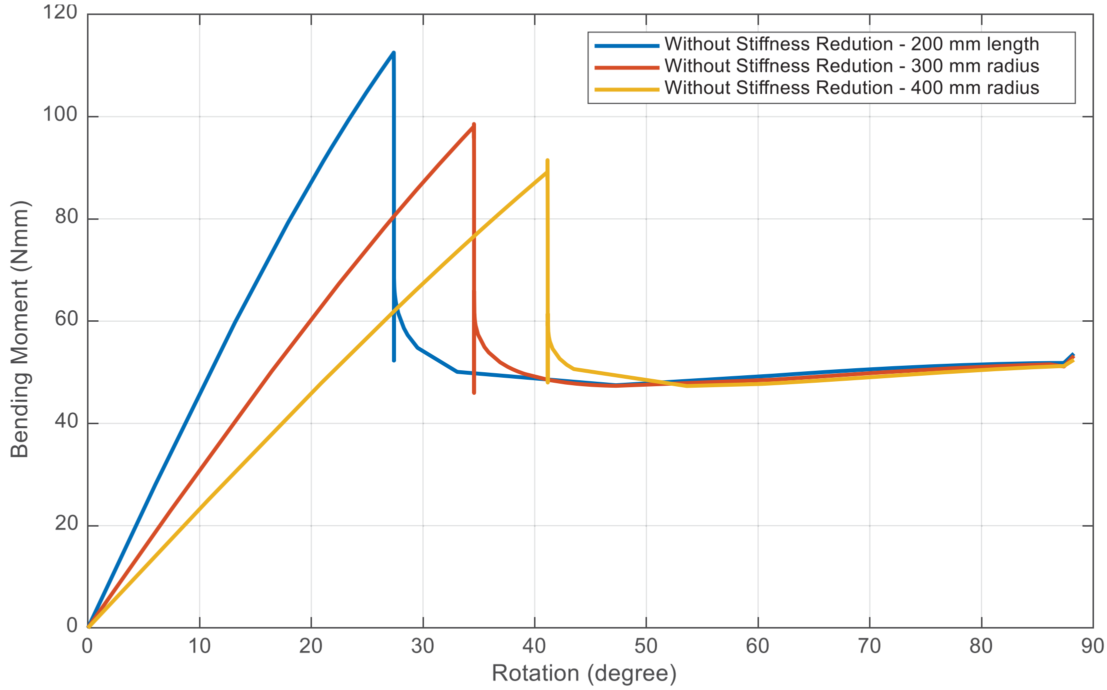

Fig. 4.6: Bending moment – rotation relationship comparison without subroutine for different tape-spring lengths ($R = 10$ mm, $\alpha = 80°$)

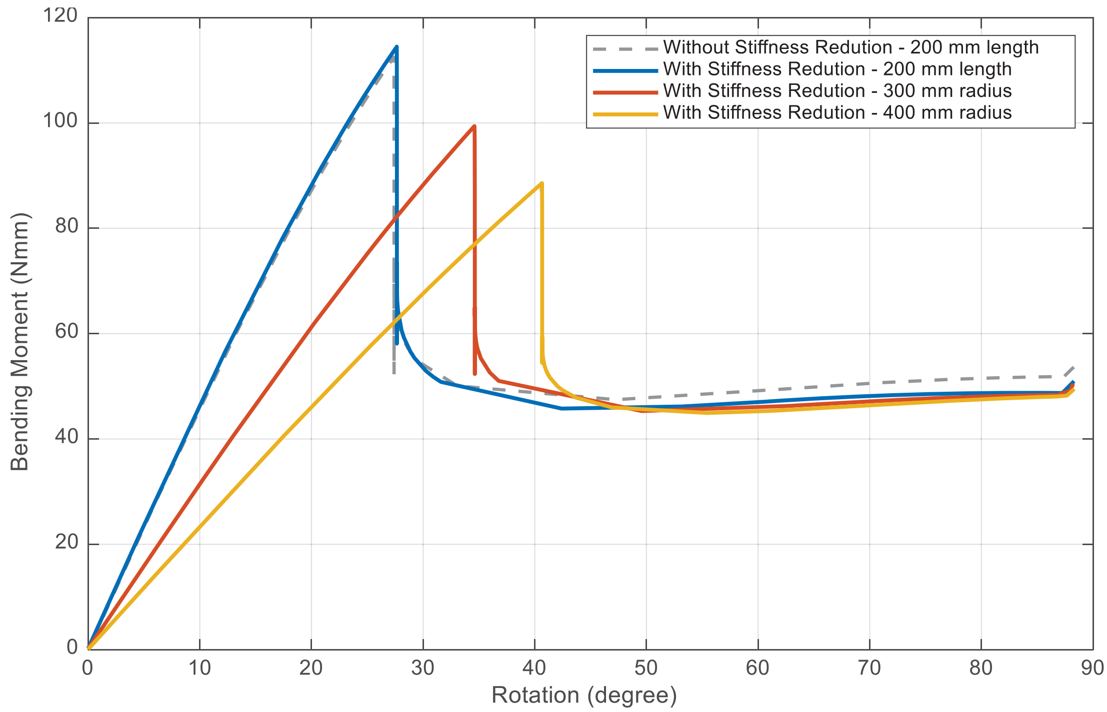

Fig. 4.7: Bending moment – rotation relationship comparison with and without subroutine for different tape-spring lengths ($R = 10$ mm, $\alpha = 80°$)

4.2. Validation of the Numerical Models against Analytical Predictions

To evaluate the impact of incorporating bending stiffness degradation, numerical simulations were conducted with and without the UGENS subroutine. This section aims to validate both versions of the numerical model, qualitatively and quantitatively, wherever applicable analytical solutions are available. However, since no experimental data could be found for the bending moment response of tape-springs made from the same material system (T300-1k/PMT-F4 woven composite), a direct one-to-one quantitative comparison was not feasible.

4.2.1. Validation of the Tape-spring Model without Stiffness Reduction

The bending moment–rotation response of the tape-spring models was analysed for different transverse radii (Fig. 4.8) and subtended angles (Fig. 4.9). The results show that the steady-state bending moment in the fully folded region is independent of the transverse radius but varies with the subtended angle, in agreement with the analytical expression given in Equation 2.20. The analytical values presented in these figures were evaluated using Equation 2.20 only for the fully folded configuration, as the expression is derived specifically for this state. Minor discrepancies between the numerical and analytical results are observed and can be attributed to complex structural behaviours, such as local instabilities and bifurcations, that are captured by the numerical models but are not represented in the simplified analytical formulation.

The variation in bending moment with subtended angle can be further interpreted using Equation 2.10. Zuo et al. [66] analytically investigated this relationship and demonstrated that the peak bending moment increases with increasing subtended angle, while snap-through occurs at a lower longitudinal radius of curvature for tape-springs with larger subtended angles (see Fig. 4.10). It should be noted that the material properties adopted by Zuo et al. [66] differ from those used in the present study; therefore, the results are not directly comparable in a quantitative sense. Nevertheless, the same analytical framework can also be used to interpret the influence of transverse radius. The variation of bending moment with transverse radius predicted by Equation 2.10 is illustrated in Fig. 4.11 and provides further validation of the trends observed in the numerical simulations.

In addition, the bending moment per unit width (moment stress resultant) as a function of longitudinal curvature was evaluated using Equation 2.18, as shown in Fig. 4.12. The numerical predictions exhibit good agreement with the analytical values corresponding to the fully folded configuration ($r = R$). The analytical results, indicated by star symbols (*), are plotted only at the fully folded state for each transverse radius, since Equation 2.18 is derived under the assumption that the transverse and longitudinal radii are equal. Consequently, a continuous analytical curve cannot be defined over the entire curvature range. In contrast, the numerical model without the subroutine exhibits a purely linear increase in sectional bending moment with curvature, as bending stiffness degradation is not accounted for.

Furthermore, because the longitudinal curvature in the folded region is given by $1/R$ (Equation 2.17), the maximum curvature experienced by the tape-spring is governed solely by its transverse radius.

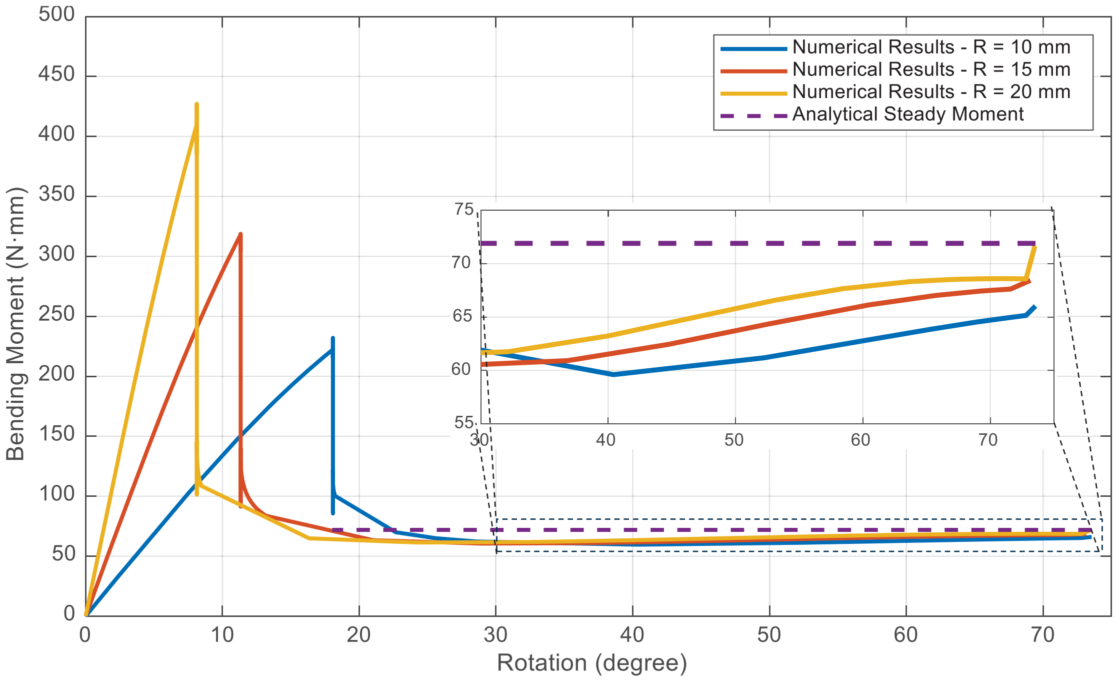

Fig. 4.8: Bending moment – rotation variation for different transverse radii without stiffness reduction ($\alpha = 100°$)

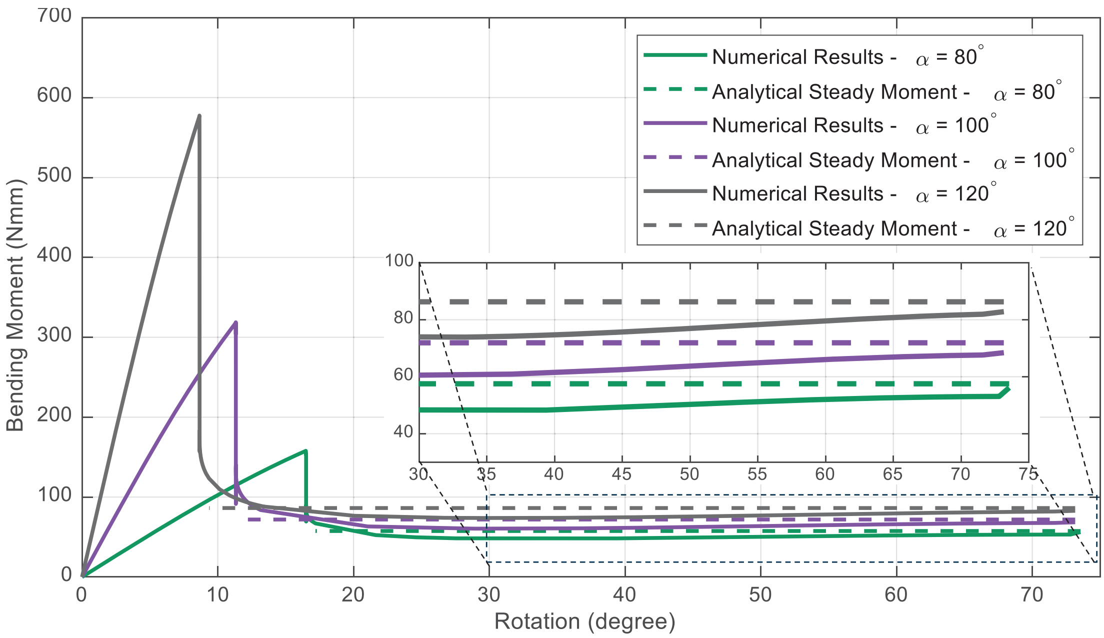

Fig. 4.9: Bending moment – rotation variation for different subtended angles without stiffness reduction ($R = 15$ mm)

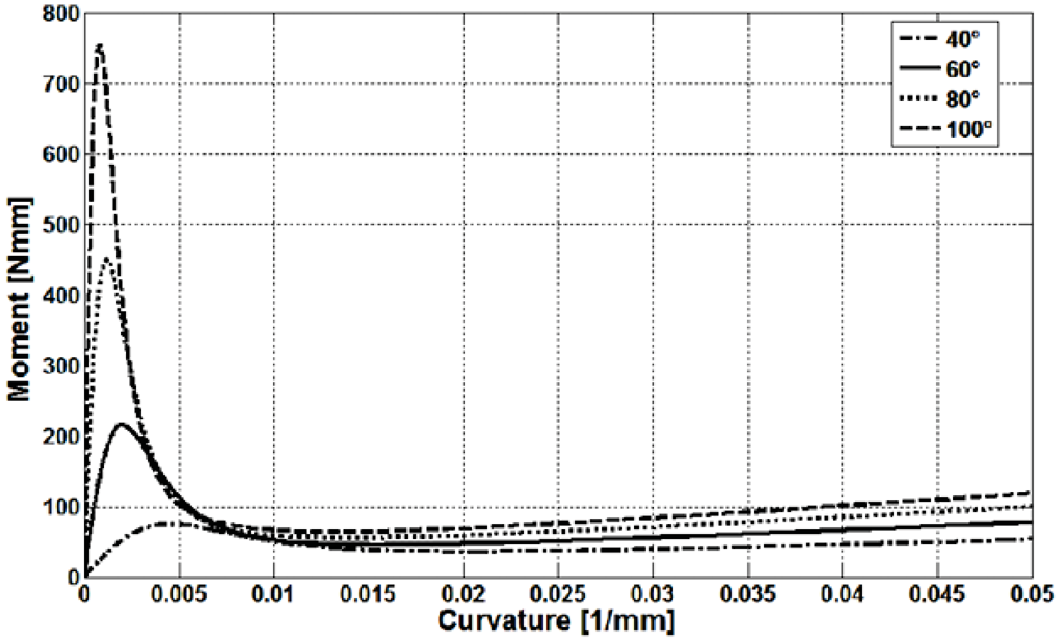

Fig. 4.10: Overall bending moment variation according to the Equation 2.10 for different subtended angles. Adapted from [66]

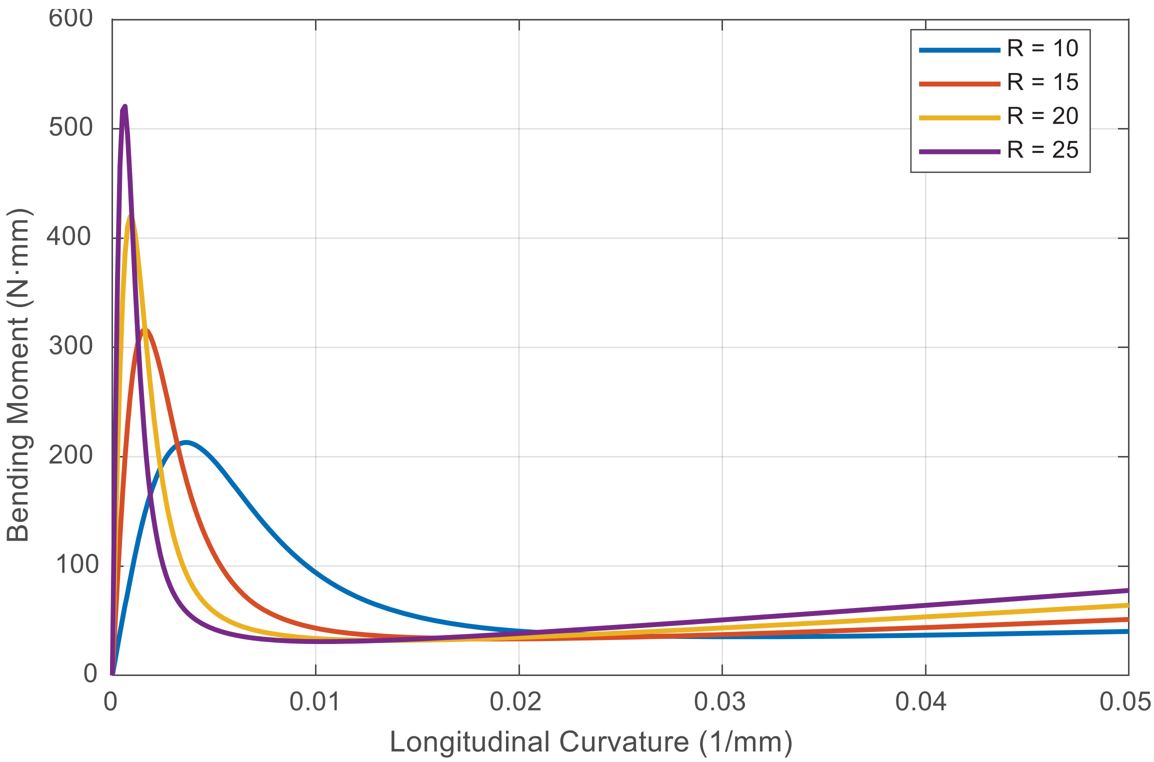

Fig. 4.11: Overall bending moment variation according to the Equation 2.10 for different transverse radii ($\alpha = 100°$)

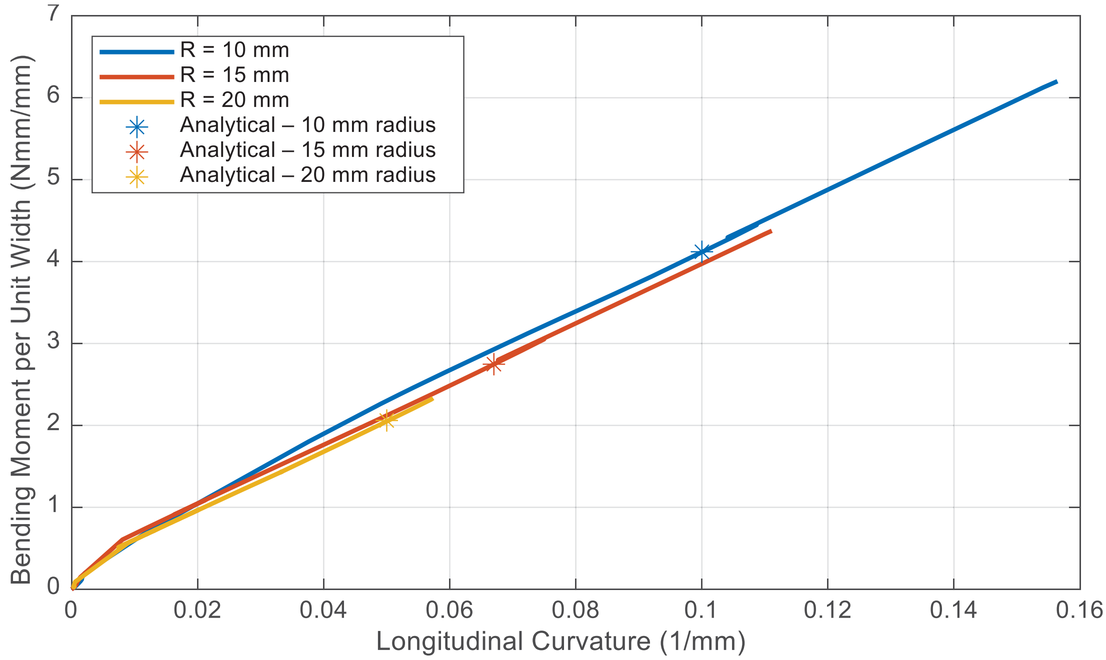

Fig. 4.12: Bending moment per unit width – longitudinal curvature relationship (without stiffness reduction) for different transverse radii along with a comparison with analytical results

4.2.2. Validation of the Tape-spring Model and Numerical Framework with Stiffness Reduction

As no specific analytical expression exists for the steady-state moment in tape-springs with varying bending stiffness, the bending moment–rotation response obtained from the model with the UGENS subroutine could not be quantitatively validated using analytical equations. However, as shown in Fig. 4.13 and Fig. 4.14, the simulated bending behaviour follows the same general trend predicted by Equations 2.18 and 2.20, in which the steady-state moment depends on the subtended angle but remains independent of the transverse radius.

The bending moment stress resultant was further evaluated for models with different transverse radii (Fig. 4.15). The results demonstrate a clear nonlinear response, particularly for models experiencing high curvature. For larger transverse radii, the maximum longitudinal curvature is lower, resulting in a less pronounced influence of stiffness degradation. In contrast, models with smaller transverse radii exhibit a significant reduction in bending moment due to the nonlinear stiffness behaviour introduced through the subroutine.

To further validate this response, the tape-spring model with a transverse radius of 10 mm was compared with results obtained using Equation 3.14, which accounts for curvature-dependent bending stiffness, unlike Equation 2.18. Very good agreement was observed. In addition, experimental results from the flat shell coupon (see Fig. 4.15) closely matched the tape-spring model predictions, further supporting the accuracy of the proposed multi-scale framework. These results confirm that the developed UGENS subroutine is capable of capturing bending stiffness nonlinearity even under complex deformation mechanisms such as bifurcation. The consistency of the results also indicates that the influence of transverse curvature (κ_2) i is minimal, likely due to the relatively small magnitude of D_{12} compared to D_{11} in the stiffness matrix.

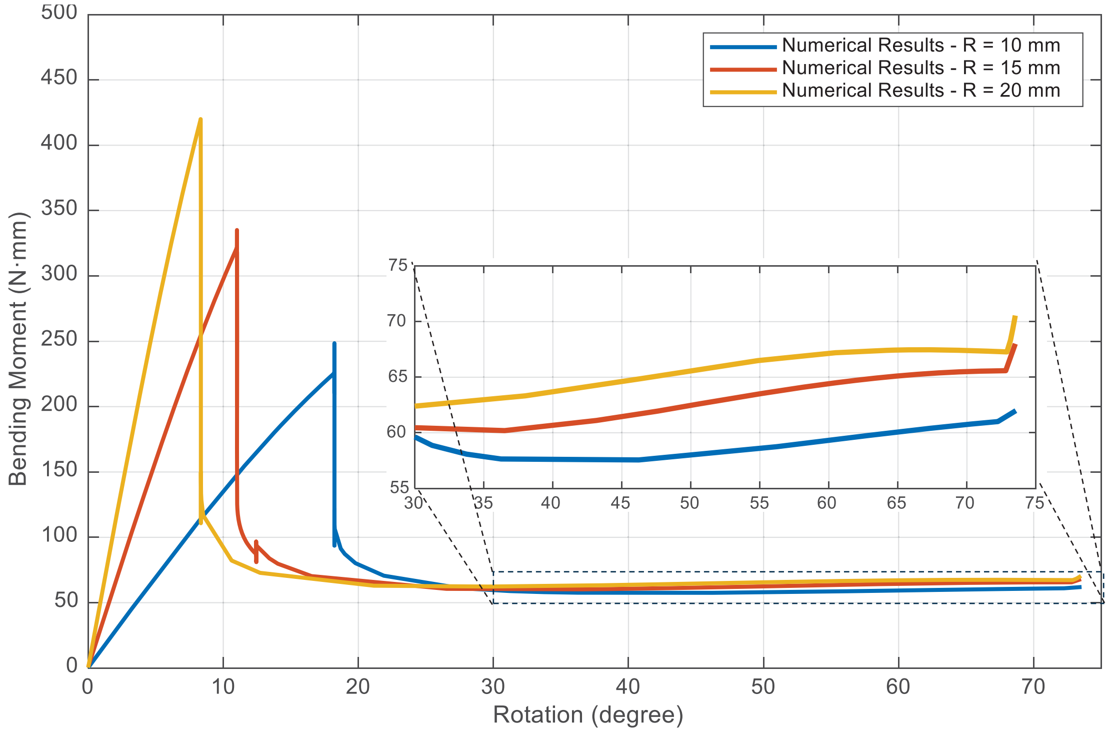

Fig. 4.13: Bending moment – rotation variation for different transverse radii with stiffness reduction ($\alpha = 100°$)

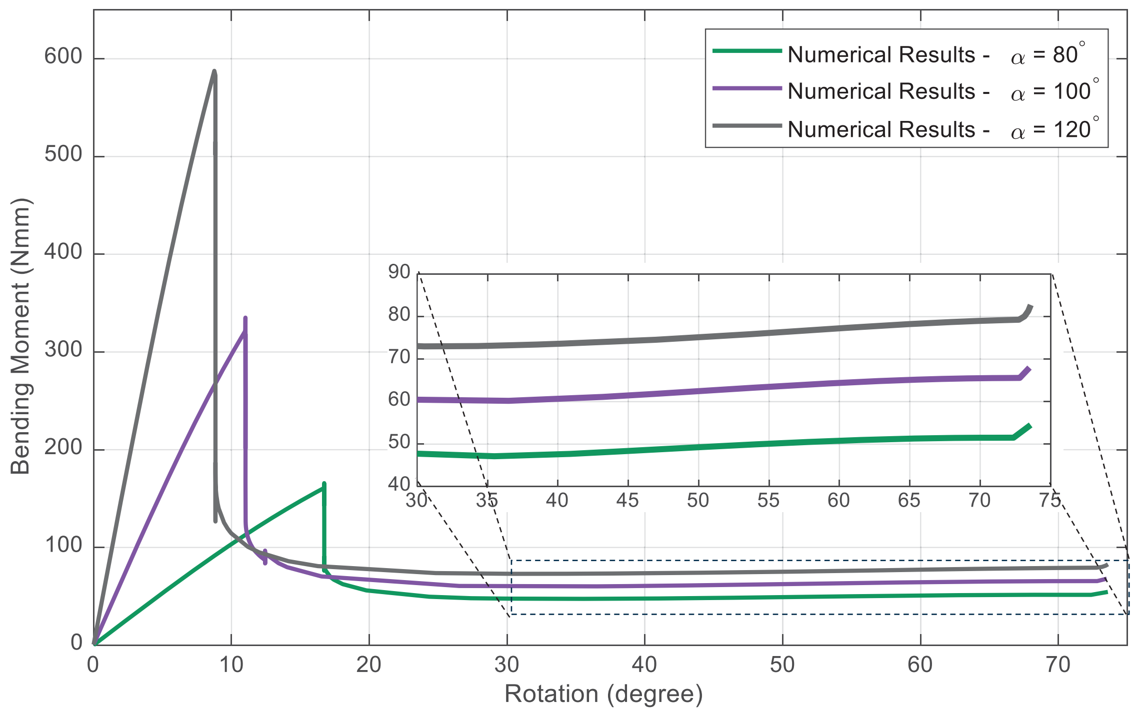

Fig. 4.14: Bending moment – rotation variation for different subtended angles without stiffness reduction ($R = 15$ mm)

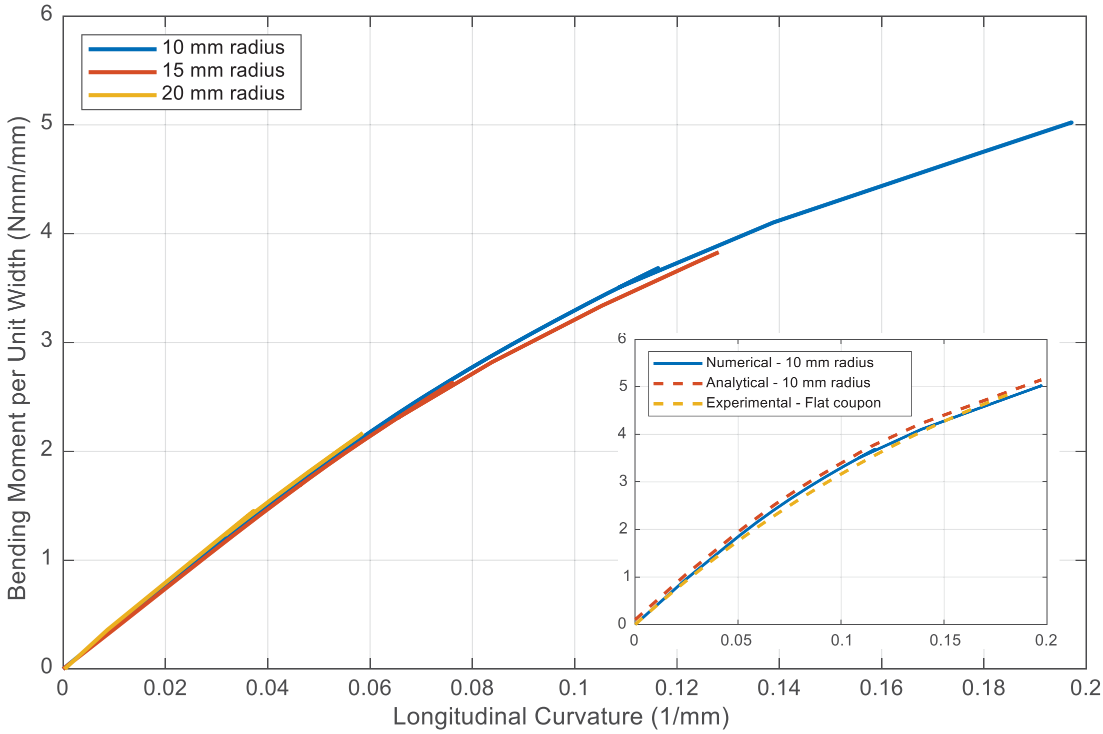

Fig. 4.15: Bending moment per unit width – longitudinal curvature relationship (with stiffness reduction) for different transverse radii along with a comparison with analytical results for 10 mm radius tape-spring model and CBT results for flat coupon

4.3. Impact of Stiffness Reduction on Moment vs Rotation Variation of Tape-springs

As illustrated in Fig. 4.15, the influence of bending stiffness nonlinearity is more pronounced in tape-springs with lower transverse radii. In contrast, the subtended angle has little effect on this behaviour, as it does not influence the maximum transverse or longitudinal curvatures experienced during folding. Therefore, to isolate the effect of transverse radius, numerical simulations were conducted with and without the UGENS subroutine for various transverse radii (see Fig. 4.16).

At low curvature levels, where the peak moment typically occurs, the effect of stiffness reduction is minimal. As a result, the peak moment values remained nearly identical across models with and without stiffness degradation. However, at higher curvature levels, particularly in the fully folded region, the steady-state moments were significantly reduced in models incorporating stiffness degradation. This is expected, as maximum curvatures arise in the folded configuration, where nonlinear behaviour becomes more dominant.

Moreover, the difference between the steady-state moments of models with and without stiffness degradation increases with decreasing transverse radius, owing to the higher maximum curvature in smaller radii. This trend is illustrated in Fig. 1.1Fig. 4.17 through a heat map showing the percentage reduction in steady-state moments relative to the non-degraded model, across various tape-spring geometries defined by transverse radii and subtended angles.

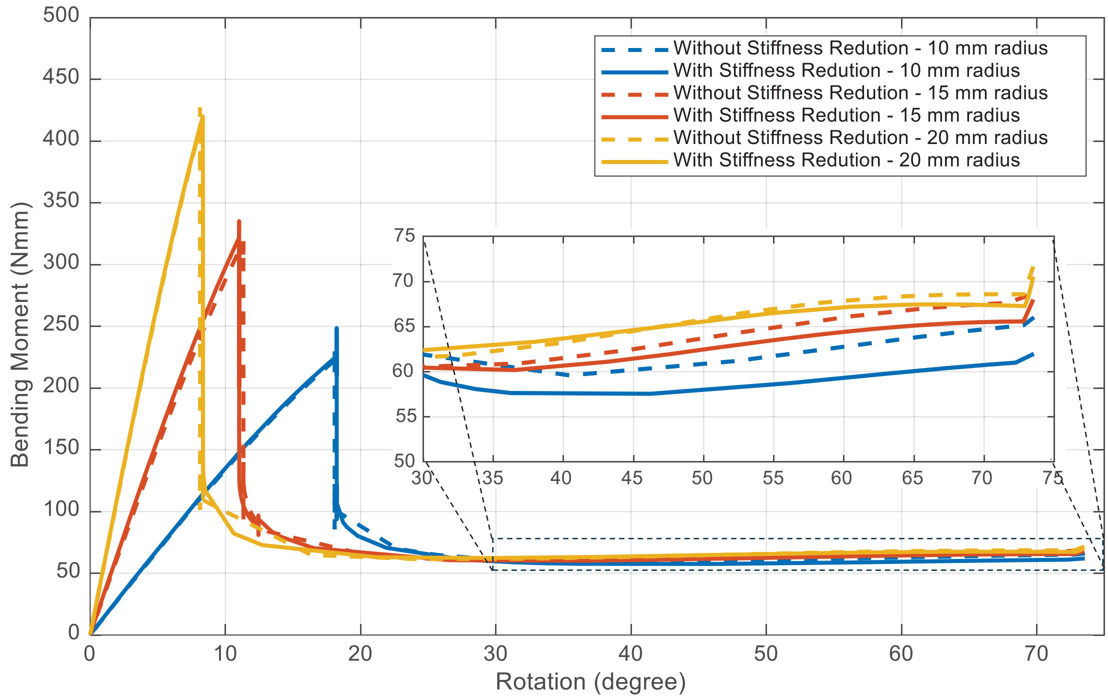

Fig. 4.16: Bending moment – rotation relationship comparison with and without subroutine for tape-spring models with different radii ($\alpha = 100°$)

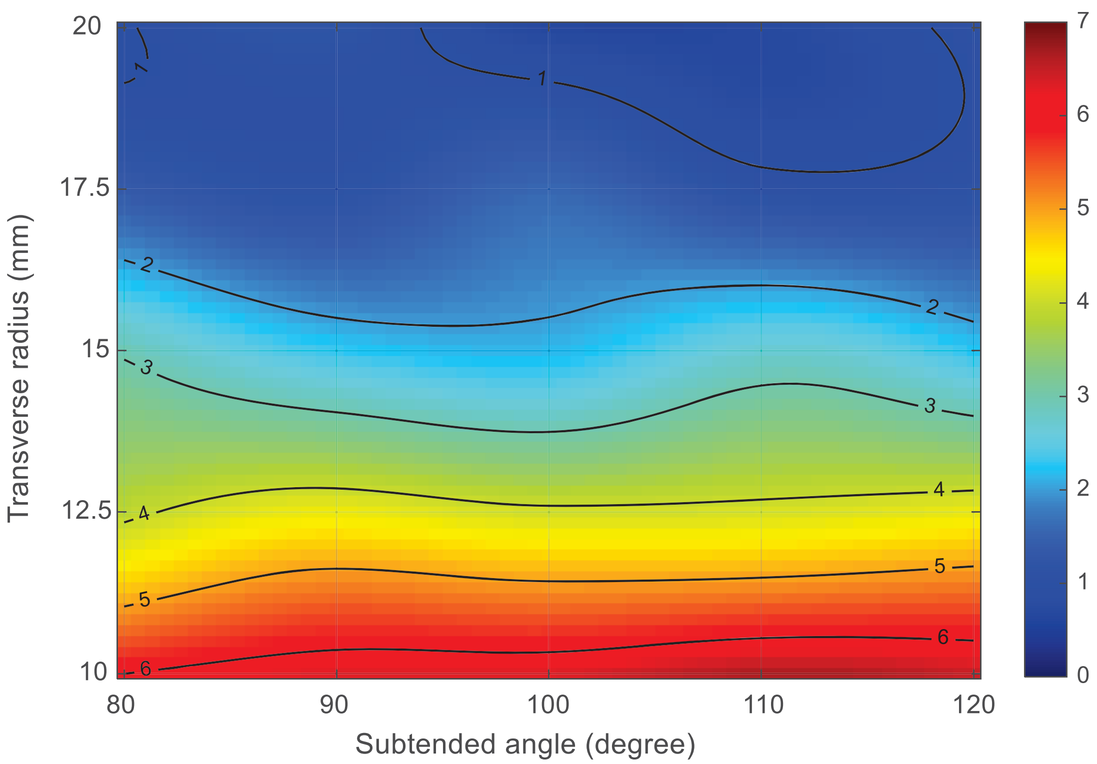

Fig. 4.17: Heat map for the disparity between with and without stiffness reduction as a percentage

Although the peak bending moment is largely unaffected by stiffness degradation, its accurate prediction alone is not sufficient to assess the performance of deployable composite tape-spring structures. In aerospace applications, peak moments typically govern initial locking, release, or latching mechanisms, which occur at relatively low curvature levels where stiffness nonlinearity is limited [63]. In contrast, the steady-state moment at high curvature, particularly in the fully folded or stowed configuration, governs the stored strain energy and deployment torque, and therefore plays a decisive role in post-deployment stability and deployment reliability. This steady-state behaviour is especially critical in tape-spring-driven systems such as deployable solar arrays, antennas, and lightweight composite booms, where deployment is controlled by the release of bending energy rather than by peak load capacity [83], [84], [85]. Neglecting curvature-dependent stiffness degradation leads to an over-estimation of steady-state moments and, consequently, the stored energy available for deployment. The implications of this over-estimation on energy terms and deployment dynamics are examined in detail in Section 4.4. Therefore, incorporating curvature-dependent stiffness degradation is essential for realistically capturing the full deployment mechanics of woven-composite tape-springs, particularly for configurations with small transverse radii where nonlinear effects are most pronounced.

4.4. Impact of Stiffness Reduction on Strain Energy of the Tape-Spring

An analytical expression was formulated to calculate the bending strain energy of the tape-spring based on Equations 2.16 and 2.17. Considering the symmetric phase angle across the mid-plane of the woven composite, it can be assumed that $D_{11} = D_{22}$ (see Equation 3.6). Therefore, from Equation 2.18, r can be considered equal to the R. Accordingly, the strain energy of the woven composite can be derived as follows:

$$U_{bending} = \frac{1}{2} \times 2\frac{(D_{11} + D_{12})}{R^2} \times R^2\theta\varphi$$

$$U_{bending} = (D_{11} + D_{12})\theta\varphi \tag{4.6}$$

Fig. 4.18 shows good agreement between the strain energy obtained from the numerical model and the analytical estimate, supporting the validity of the numerical energy-history predictions. It should be noted that the analytical value is available only for the fully folded configuration; therefore, the comparison is limited to the response up to the snap-back event, which occurs at a rotation of 28°.

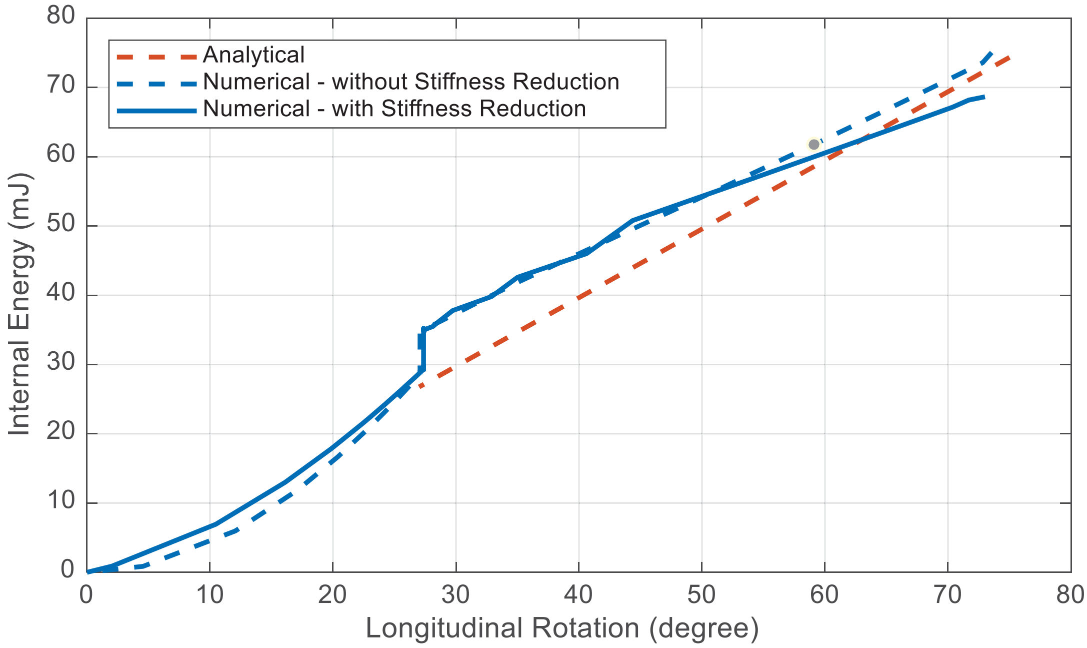

Fig. 4.18: Strain energy history from the numerical model and analytical equation ($R = 10$ mm, $\alpha = 80°$)

A sensitivity analysis was then conducted to evaluate the impact of mesh size on the computed energy histories (see Fig. 4.19). The stiffness-reduction model of the tape-spring with a 10 mm transverse radius and an 80° subtended angle was selected for this analysis, as it undergoes relatively high longitudinal and transverse curvatures, making the influence of bending stiffness reduction more pronounced. When the deployment region is considered, the effect of mesh size on the results is negligible. However, during the folding stage, a slight variation can be observed between the different mesh configurations. As the overall trend remains consistent across all mesh sizes and considering computational efficiency, a mesh size of 0.5 mm was adopted for subsequent analyses.

The energy histories of internal energy, strain energy, and kinetic energy were compared between the numerical models with and without stiffness degradation (see Fig. 4.20). It can be seen that the strain energy closely overlaps with the internal energy, while the kinetic energy remains negligible throughout the simulation. Furthermore, the model with stiffness reduction shows a lower peak strain energy during deployment than the constant-stiffness model. Overall, its internal energy is lower by 6.4×10^{-3} J, corresponding to an 8.53% reduction. Both models display a distinct drop in strain energy corresponding to the snap-back phenomenon. However, following the snap-back, the influence of stiffness reduction becomes less significant, as the corresponding curvature in this region is relatively small.

This behaviour can be attributed to the reduction in stresses developed within the elements experiencing high curvature when stiffness degradation is introduced. In such regions, particularly within the folded zone, the reduced stress (or equivalently, the lower bending moment per unit width) results in smaller strain and internal energy values compared to the model without stiffness reduction. This behaviour is clearly illustrated in Fig. 4.21, which presents the variation of internal energy with rotation, and in Fig. 4.22, which shows internal energy variation with curvature.

Additionally, the work done by the tape-springs with constant and varying stiffnesses was evaluated (see Fig. 4.23). Although the two models exhibit closely overlapping trends, a slight reduction in work done can be observed in the model incorporating stiffness degradation. This reduction directly corresponds to the decrease in internal energy, indicating that less work is required in the model with reduced stiffness.

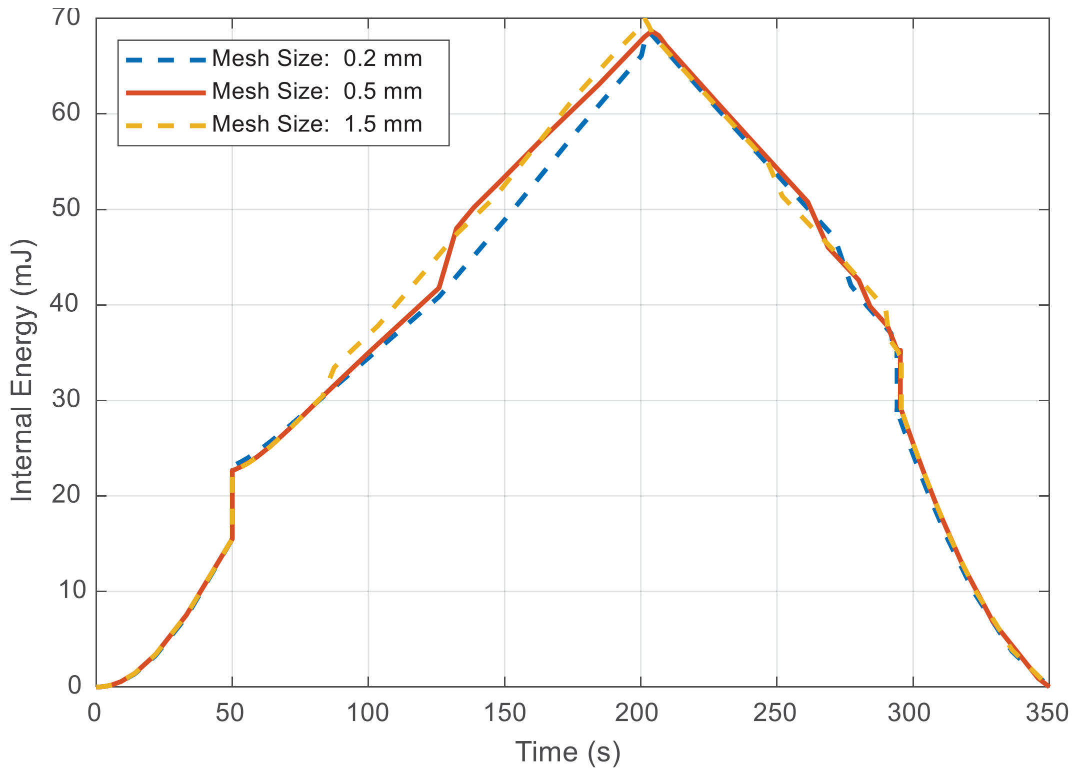

Fig. 4.19: Mesh sensitivity analysis ($R = 10$ mm, $\alpha = 80°$)

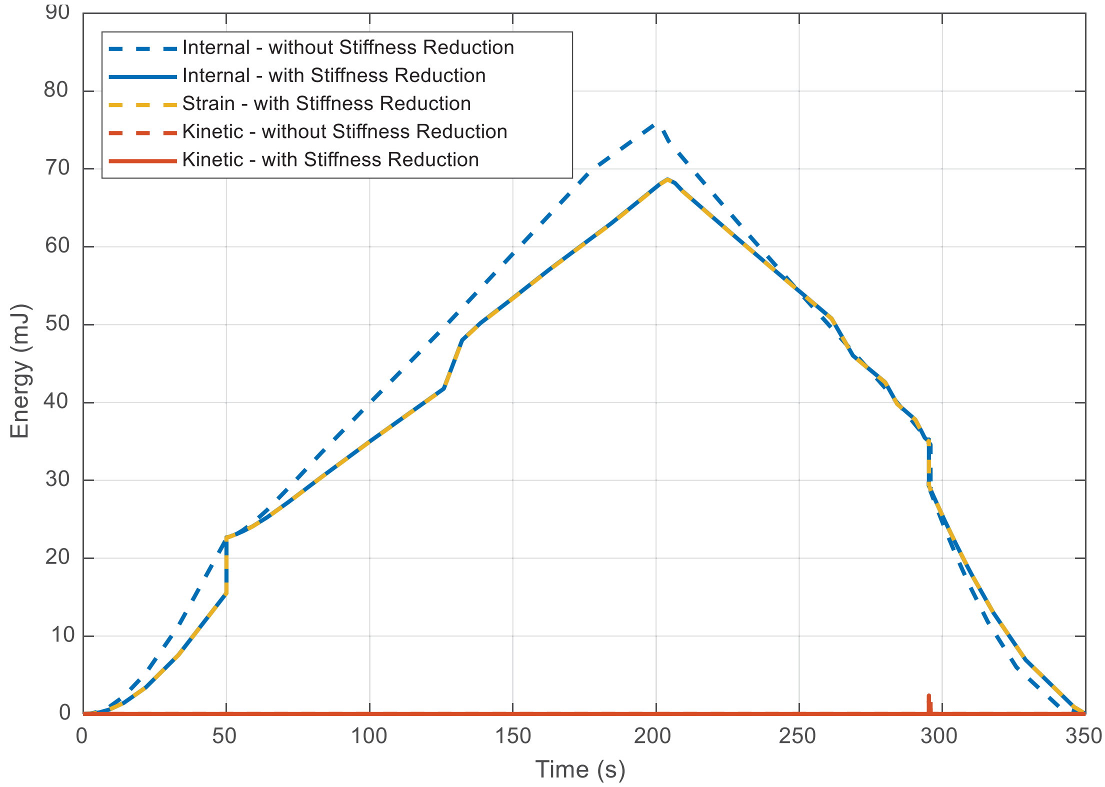

Fig. 4.20: Energy histories ($R = 10$ mm, $\alpha = 80°$)

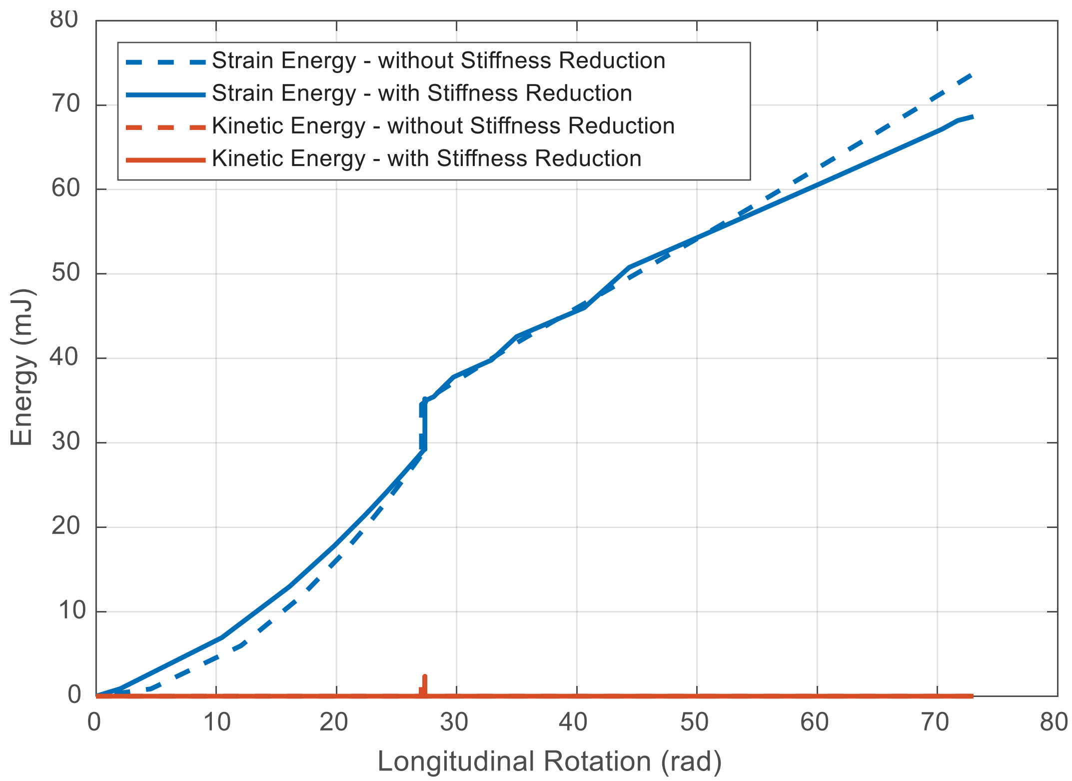

Fig. 4.21: Energy histories for the deployment ($R = 10$ mm, $\alpha = 80°$)

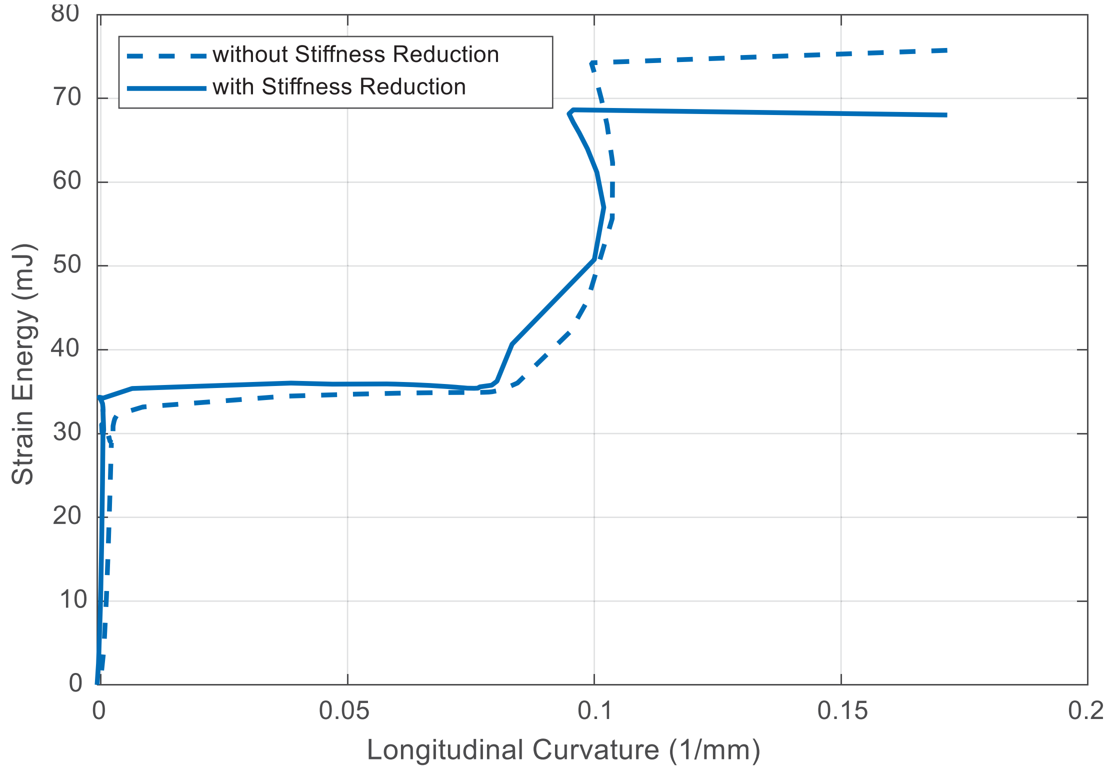

Fig. 4.22: Strain energy variation with longitudinal curvature for the deployment ($R = 10$ mm, $\alpha = 80°$)

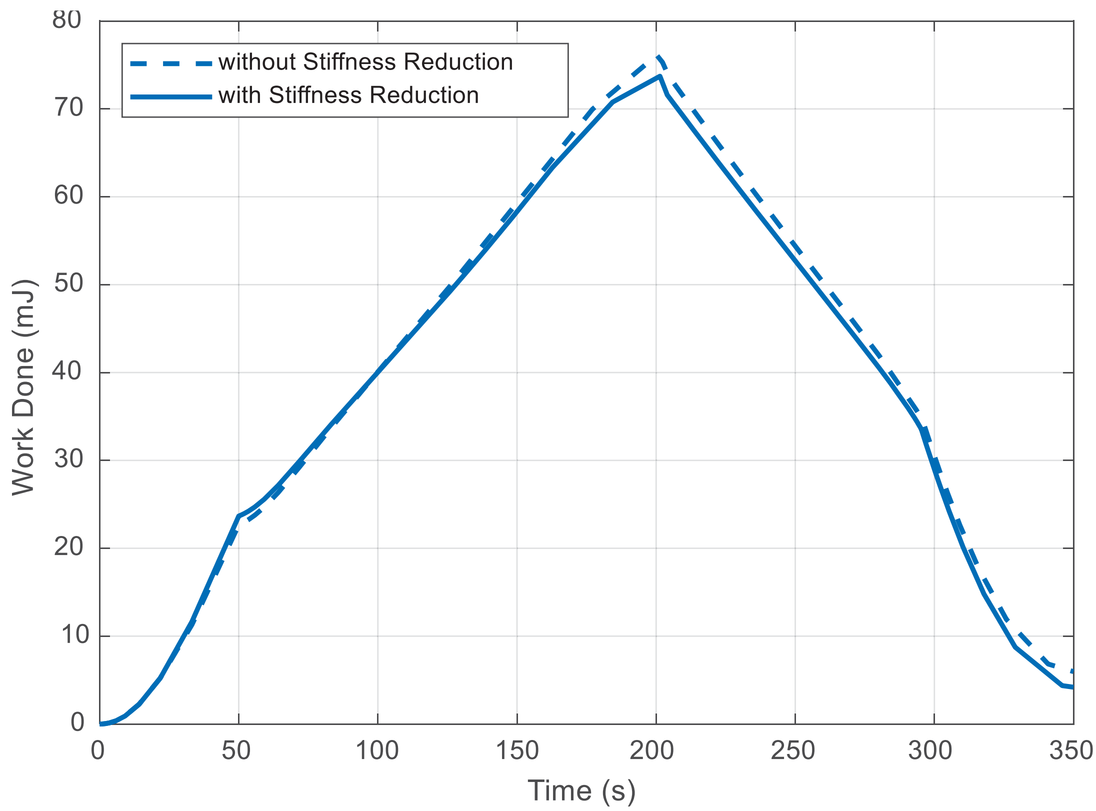

Fig. 4.23: Work done history ($R = 10$ mm, $\alpha = 80°$)

Building on the moment-based observations discussed in Section 4.3, the reduction in peak strain and internal energy observed here has important implications for the dynamic deployment of aerospace structures employing woven composite tape-spring elements. In such systems, deployment is driven by the controlled release of bending energy accumulated during compact stowage, making accurate prediction of internal and strain energy essential for reliable operation [83], [84], [85]. Over-estimating the stored energy by neglecting stiffness degradation can result in inaccurate deployment force predictions, potentially leading to incomplete deployment, asymmetric unfolding, or excessive dynamic shock during snap-through [85]. The results presented in this section demonstrate that accounting for curvature-dependent stiffness reduction yields a lower and more realistic estimate of the stored energy, particularly in the fully folded configuration where nonlinear effects dominate. This improved energy prediction is especially relevant for compactly stowed deployable assemblies with limited deployment margins and reinforces the necessity of incorporating stiffness degradation effects in numerical frameworks for woven-composite deployable aerospace structures.

CHAPTER 5

5. CONCLUSIONS AND FUTURE WORK

This research addressed the absence of a numerical framework capable of capturing the nonlinear bending response of thin carbon-fibre woven composites. In this regard, a multi-scale modelling approach was developed and implemented, enabling the integration of bending stiffness nonlinearity into numerical simulations through user-defined subroutines. At the meso-scale, a detailed finite element model was established to capture material plasticity and progressive damage mechanisms within woven composites, successfully reproducing the complete bending response when compared with experimental data. Building on this foundation, a macro-scale modelling framework was formulated using a UGENS user-defined subroutine to embed the bending stiffness variation derived from the meso-scale model into macro-scale simulations. The subroutine was validated by simulating the bending behaviour of thin woven composites under pure bending and comparing the results against literature data from CBT experiments.

The proposed multi-scale modelling framework was then applied to analyse the behaviour of space structures, particularly tape-springs, under large deformations. In this study, only opposite-sense bending of tape-springs was considered. The combined numerical framework accurately captured both the nonlinear sectional bending behaviour at the element level and the global bending response of the entire structure. Overall, the study established a reliable and versatile modelling strategy for incorporating bending stiffness degradation into the design and simulation of thin carbon-fibre composite space structures.

5.1. Key Findings

The major findings of this study can be summarised as follows:

- A custom UGENS user-defined subroutine was formulated and successfully implemented to introduce bending stiffness nonlinearity into macro-scale analyses. This integration enabled commercial finite element software (ABAQUS/Standard, in this research) to account for nonlinear stiffness variation without explicit meso-scale modelling.
- The developed framework was validated against CBT experimental datasets available in the literature. The simulations accurately reproduced the moment–curvature relationships of flat thin woven composite coupons under pure bending.
- The framework was applied to the pure bending of singly curved composite structures, specifically the opposite-sense bending of tape-springs, which undergo bifurcations such as snap-through and local buckling. The results were validated against analytical equations from the literature, confirming the

applicability of the modelling framework even under highly nonlinear behaviours.

- Numerical analyses revealed that bending stiffness degradation significantly influences the global structural behaviour of tape-springs with lower transverse radii. The influence of stiffness reduction was less pronounced in tape-springs with higher transverse radii, as they experience smaller curvatures both transversely and longitudinally.
- The peak moment during the deployment of tape-springs in opposite-sense bending showed negligible variation with stiffness reduction, as this occurred at a relatively low longitudinal curvature.
- A noticeable reduction in strain energy is observed in tape-spring models incorporating stiffness degradation compared to those without, particularly when a folded region is present. Following the snap-back phenomenon, this difference becomes insignificant. The reduction in strain energy arises from the lower stress magnitudes generated in the folding region, where elements experience large curvatures under degraded stiffness.

5.2. Limitations

While the developed approach achieved strong validation, several limitations remain:

- The meso-scale model was based on plane-stress assumptions and did not include full three-dimensional yarn geometry, which may influence out-of-plane stiffness degradation.
- The current UGENS subroutine assumes uniform stiffness reduction along the section, which may not fully represent localised damage accumulation in complex geometries.
- The framework was validated primarily for quasi-static loading conditions; dynamic or cyclic effects may introduce additional nonlinearities not captured in this study.
- The developed UGENS subroutine experienced convergence difficulties when sudden deformation changes occurred under torsional deformations as maintaining a smooth stiffness reduction under such conditions challenging.

5.3. Recommendations for Future Work

Future research can extend the present framework in several important directions:

- Enhancing the UGENS subroutine to capture large curvature variations introduced by torsional effects and ensure numerical stability under such deformations.

- At present, the UGENS subroutine updates only the bending stiffness components D_{11} and D_{12}. It can be extended to update the extensional stiffness components A_{11} and A_{12} as well.
- Extension of UGENS to dynamic and cyclic analyses, allowing the study of fatigue-induced stiffness degradation under repeated folding–deployment cycles.
- Experimental verification under realistic operational conditions, including large rotations and repeated load reversals, to strengthen model reliability and expand its applicability.

5.4. Concluding Remarks

In summary, this research provides a robust and validated methodology for capturing the nonlinear bending stiffness behaviour of thin carbon-fibre woven composites. The integration of meso-scale damage modelling with user-defined subroutines marks a significant advancement in the numerical simulation of lightweight deployable structures. The developed approach enhances both the accuracy and efficiency of structural analyses, paving the way for more reliable and optimised composite-based space systems in future engineering applications.

REFERENCES

[1] S. Daynes and P. Weaver, "Review of shape-morphing automobile structures: Concepts and outlook," *Proc. Inst. Mech. Eng. Part J. Automob. Eng.*, vol. 227, pp. 1603–1622, Nov. 2013, doi: 10.1177/0954407013496557.

[2] Y. Li and S. Pellegrino, "A Theory for the Design of Multi-Stable Morphing Structures," *J. Mech. Phys. Solids*, vol. 136, p. 103772, Mar. 2020, doi: 10.1016/j.jmps.2019.103772.

[3] M. Chandra, S. Kumar, S. Chattopadhyaya, S. Chatterjee, and P. Kumar, "A review on developments of deployable membrane-based reflector antennas," *Adv. Space Res.*, vol. 68, July 2021, doi: 10.1016/j.asr.2021.06.051.

[4] M. Schenk, A. Viquerat, K. Seffen, and S. Guest, "Review of Inflatable Booms for Deployable Space Structures: Packing and Rigidization," *AIAA J. Spacecr. Rockets*, vol. 51, May 2014, doi: 10.2514/1.A32598.

[5] Y. Cao, M. Derakhshani, Y. Fang, G. Huang, and C. Cao, "Bistable Structures for Advanced Functional Systems," *Adv. Funct. Mater.*, vol. 31, no. 45, p. 2106231, 2021, doi: 10.1002/adfm.202106231.

[6] D. Spencer, B. Betts, J. Bellardo, A. Diaz, B. Plante, and J. Mansell, "The LightSail 2 Solar Sailing Technology Demonstration," *Adv. Space Res.*, vol. 67, June 2020, doi: 10.1016/j.asr.2020.06.029.

[7] "Webb and Origami - NASA Science." Accessed: Feb. 06, 2025. [Online]. Available: https://science.nasa.gov/mission/webb/webb-and-origami/

[8] S. Yue, "A Review of Origami-Based Deployable Structures in Aerospace Engineering," *J. Phys. Conf. Ser.*, vol. 2459, no. 1, p. 012137, Mar. 2023, doi: 10.1088/1742-6596/2459/1/012137.

[9] H. M. Y. C. Mallikarachchi, "Predicting mechanical properties of thin woven carbon fiber reinforced laminates," *Thin-Walled Struct.*, vol. 135, pp. 297–305, Feb. 2019, doi: 10.1016/j.tws.2018.11.016.

[10] Y. Wang, Y. Zhou, and C. Jin, "An analytical nonlinear model for plain-woven composites under off-axis loads," *Compos. Struct.*, vol. 296, p. 115905, Sept. 2022, doi: 10.1016/j.compstruct.2022.115905.

[11] H. Alshahrani and M. Hojjati, "A new test method for the characterization of the bending behavior of textile prepregs," *Compos. Part Appl. Sci. Manuf.*, vol. 97, pp. 128–140, June 2017, doi: 10.1016/j.compositesa.2017.02.027.

[12] H. T. Hahn and S. W. Tsai, "Nonlinear Elastic Behavior of Unidirectional Composite Laminae," *J. Compos. Mater.*, vol. 7, no. 1, pp. 102–118, Jan. 1973, doi: 10.1177/002199837300700108.

[13] T. Ishikawa and T.-W. Chou, "Nonlinear Behavior of Woven Fabric Composites," *J. Compos. Mater.*, vol. 17, no. 5, pp. 399–413, Sept. 1983, doi: 10.1177/002199838301700502.

[14] G. Sanford, A. Biskner, and T. Murphey, "Large Strain Behavior of Thin Unidirectional Composite Flexures," in *51st AIAA/ASME/ASCE/AHS/ASC Structures, Structural Dynamics, and Materials Conference; 18th*

AIAA/ASME/AHS Adaptive Structures Conference, Orlando, Florida: American Institute of Aeronautics and Astronautics, 2010. doi: 10.2514/6.2010-2698.

[15] W. Tan and B. G. Falzon, “A crystal plasticity phenomenological model to capture the non-linear shear response of carbon fibre reinforced composites,” *Int. J. Lightweight Mater. Manuf.*, vol. 4, no. 1, pp. 99–109, Mar. 2021, doi: 10.1016/j.ijlmm.2020.06.004.

[16] A. Muc, “Effects of Material Nonlinearities on Design of Composite Constructions—Elasto-Plastic Behaviour,” *Materials*, vol. 13, no. 7, p. 1792, Apr. 2020, doi: 10.3390/ma13071792.

[17] A. H. Sharma, T. J. Rose, N. Bearns, T. W. Murphey, and F. López Jiménez, “Analysis of Geometric and Material Nonlinearity in the Column Bending Test,” *AIAA J.*, vol. 62, no. 4, pp. 1300–1310, Apr. 2024, doi: 10.2514/1.J063247.

[18] C. McCarthy and T. Vaughan, “14 - Micromechanical failure analysis of advanced composite materials,” in *Numerical Modelling of Failure in Advanced Composite Materials*, P. P. Camanho and S. R. Hallett, Eds., in Woodhead Publishing Series in Composites Science and Engineering. , Woodhead Publishing, 2015, pp. 379–409. doi: 10.1016/B978-0-08-100332-9.00014-1.

[19] J. Zhou *et al.*, “Exploring shear nonlinearity of plain-woven composites at various temperatures based on machine learning,” *Compos. Struct.*, vol. 346, p. 118434, Oct. 2024, doi: 10.1016/j.compstruct.2024.118434.

[20] M. Zscheyge, R. Böhm, A. Hornig, J. Gerritzen, and M. Gude, “Rate dependent non-linear mechanical behaviour of continuous fibre-reinforced thermoplastic composites – Experimental characterisation and viscoelastic-plastic damage modelling,” *Mater. Des.*, vol. 193, p. 108827, Aug. 2020, doi: 10.1016/j.matdes.2020.108827.

[21] A. Tabiei and Y. Jiang, “Woven fabric composite material model with material nonlinearity for nonlinear finite element simulation,” *Int. J. Solids Struct.*, vol. 36, no. 18, pp. 2757–2771, June 1999, doi: 10.1016/S0020-7683(98)00127-9.

[22] B. Erice and D. Thomson, “Modelling the Non-linear fibre and matrix dominated compressive behaviour in unidirectional Fibre-reinforced composites,” *Compos. Struct.*, vol. 304, p. 116396, Jan. 2023, doi: 10.1016/j.compstruct.2022.116396.

[23] A. Le, S. Nimbalkar, N. Zobeiry, and S. Malek, “An efficient multi-scale approach for viscoelastic analysis of woven composites under bending,” *Compos. Struct.*, vol. 292, p. 115698, July 2022, doi: 10.1016/j.compstruct.2022.115698.

[24] R. R. Madke and R. Chowdhury, “A multiscale continuum model for inelastic behavior of woven composite,” *Compos. Struct.*, vol. 226, p. 111267, Oct. 2019, doi: 10.1016/j.compstruct.2019.111267.

[25] T. A. Bogetti, C. P. R. Hoppel, V. M. Harik, J. F. Newill, and B. P. Burns, “Predicting the nonlinear response and progressive failure of composite laminates,” *Compos. Sci. Technol.*, vol. 64, no. 3, pp. 329–342, Mar. 2004, doi: 10.1016/S0266-3538(03)00217-3.

[26] O. Cousigné, D. Moncayo, D. Coutellier, P. Camanho, H. Naceur, and S. Hampel, “Development of a new nonlinear numerical material model for woven composite materials accounting for permanent deformation and damage,”

Compos. Struct., vol. 106, pp. 601–614, Dec. 2013, doi: 10.1016/j.compstruct.2013.07.026.

[27] A. Tabiei and I. Ivanov, "Materially and geometrically non-linear woven composite micro-mechanical model with failure for finite element simulations," *Int. J. Non-Linear Mech.*, vol. 39, no. 2, pp. 175–188, Mar. 2004, doi: 10.1016/S0020-7462(02)00067-7.

[28] T. W. Murphey, W. Francis, B. Davis, and J. M. Mejia-Ariza, "High Strain Composites," in *2nd AIAA Spacecraft Structures Conference*, in AIAA SciTech Forum. American Institute of Aeronautics and Astronautics, Jan. 2015. doi: 10.2514/6.2015-0942.

[29] J. W. Ju, Y. F. Ko, and H. N. Ruan, "Effective Elastoplastic Damage Mechanics for Fiber Reinforced Composites with Evolutionary Partial Fiber Debonding," *Int. J. Damage Mech.*, vol. 17, no. 6, pp. 493–537, Nov. 2008, doi: 10.1177/1056789507081688.

[30] A. Puck and M. Mannigel, "Physically based non-linear stress–strain relations for the inter-fibre fracture analysis of FRP laminates," *Compos. Sci. Technol.*, vol. 67, no. 9, pp. 1955–1964, July 2007, doi: 10.1016/j.compscitech.2006.10.008.

[31] Y. Wang and Z. Huang, "A Review of Analytical Micromechanics Models on Composite Elastoplastic Behaviour," *Procedia Eng.*, vol. 173, pp. 1283–1290, Jan. 2017, doi: 10.1016/j.proeng.2016.12.159.

[32] W. H. M. V. van Dreumel and J. L. M. Kamp, "Non Hookean Behaviour in the Fibre Direction of Carbon-Fibre Composites and the Influence of Fibre Waviness on the Tensile Properties," *J. Compos. Mater.*, vol. 11, no. 4, pp. 461–469, Oct. 1977, doi: 10.1177/002199837701100408.

[33] M. G. Northolt, L. H. Veldhuizen, and H. Jansen, "Tensile deformation of carbon fibers and the relationship with the modulus for shear between the basal planes," *Carbon*, vol. 29, no. 8, pp. 1267–1279, Jan. 1991, doi: 10.1016/0008-6223(91)90046-L.

[34] M. Xie and D. F. Adams, "A plasticity model for unidirectional composite materials and its applications in modeling composites testing," *Compos. Sci. Technol.*, vol. 54, no. 1, pp. 11–21, Jan. 1995, doi: 10.1016/0266-3538(95)00035-6.

[35] M. Shioya, E. Hayakawa, and A. Takaku, "Non-hookean stress-strain response and changes in crystallite orientation of carbon fibres," *J. Mater. Sci.*, vol. 31, no. 17, pp. 4521–4532, Sept. 1996, doi: 10.1007/BF00366347.

[36] G. M. Vyas, S. T. Pinho, and P. Robinson, "Constitutive modelling of fibre-reinforced composites with unidirectional plies using a plasticity-based approach," *Compos. Sci. Technol.*, vol. 71, no. 8, pp. 1068–1074, May 2011, doi: 10.1016/j.compscitech.2011.03.009.

[37] R. K. Goldberg *et al.*, "Theoretical Development of an Orthotropic Elasto-Plastic Generalized Composite Material Model," presented at the International LS-DYNA Users Conference, Dearborn, MI, June 2014. Accessed: Dec. 15, 2024. [Online]. Available: https://ntrs.nasa.gov/citations/20150002335

[38] T. W. Murphey, G. E. Sanford, and M. M. Grigoriev, "Nonlinear Elastic Constitutive Modeling of Large Strains in Thin Carbon Fiber Composite

Flexures," presented at the 16th International Conference on Composite Structures, 2011.

[39] Y. Long, O. Rique, J. M. Fernandez, A. C. Bergan, J. E. Salazar, and W. Yu, "Simulation of the column bending test using an anisotropic viscoelastic shell model," *Compos. Struct.*, vol. 288, p. 115376, May 2022, doi: 10.1016/j.compstruct.2022.115376.

[40] Z. Liu *et al.*, "A direct prediction method for 3D woven composites bending properties based on unit-cell finite element model," *Compos. Sci. Technol.*, vol. 248, p. 110474, Mar. 2024, doi: 10.1016/j.compscitech.2024.110474.

[41] H. M. Y. C. Mallikarachchi and S. Pellegrino, "Failure criterion for two-ply plain-weave CFRP laminates," *J. Compos. Mater.*, vol. 47, no. 11, pp. 1357–1375, May 2013, doi: 10.1177/0021998312447208.

[42] M. Vogler, R. Rolfes, and P. P. Camanho, "Modeling the inelastic deformation and fracture of polymer composites – Part I: Plasticity model," *Mech. Mater.*, vol. 59, pp. 50–64, Apr. 2013, doi: 10.1016/j.mechmat.2012.12.002.

[43] Y. Wu and J. Ju, "Elastoplastic damage micromechanics for continuous fiber-reinforced ductile matrix composites with progressive fiber breakage," *Int. J. Damage Mech.*, vol. 26, no. 1, pp. 4–28, Jan. 2017, doi: 10.1177/1056789516655671.

[44] Y. Chen *et al.*, "A constitutive model for elastoplastic-damage coupling effect of unidirectional fiber-reinforced polymer matrix composites," *Compos. Part Appl. Sci. Manuf.*, vol. 130, p. 105736, Mar. 2020, doi: 10.1016/j.compositesa.2019.105736.

[45] Y. Wang *et al.*, "A micromechanics based elasto-plastic damage model for unidirectional composites under off-axis tensile loads," *Sci. Rep.*, vol. 10, no. 1, p. 847, Jan. 2020, doi: 10.1038/s41598-020-57771-8.

[46] S. A. Tabatabaei, S. V. Lomov, and I. Verpoest, "Assessment of embedded element technique in meso-FE modelling of fibre reinforced composites," *Compos. Struct.*, vol. 107, pp. 436–446, Jan. 2014, doi: 10.1016/j.compstruct.2013.08.020.

[47] C. Leclerc and S. Pellegrino, "Nonlinear elastic buckling of ultra-thin coilable booms," *Int. J. Solids Struct.*, vol. 203, pp. 46–56, Oct. 2020, doi: 10.1016/j.ijsolstr.2020.06.042.

[48] G. Ernst, M. Vogler, C. Hühne, and R. Rolfes, "Multiscale progressive failure analysis of textile composites," *Compos. Sci. Technol.*, vol. 70, no. 1, pp. 61–72, Jan. 2010, doi: 10.1016/j.compscitech.2009.09.006.

[49] Z. ming Huang, "The mechanical properties of composites reinforced with woven and braided fabrics," *Compos. Sci. Technol.*, vol. 60, no. 4, pp. 479–498, Mar. 2000, doi: 10.1016/S0266-3538(99)00148-7.

[50] S. Ogihara and K. L. Reifsnider, "Characterization of Nonlinear Behavior in Woven Composite Laminates," *Appl. Compos. Mater.*, vol. 9, no. 4, pp. 249–263, July 2002, doi: 10.1023/A:1016069220255.

[51] R. Mohamadipoor, M. H. Pol, and E. Zamani, "Nonlinear analytical study of thin laminated composite plate reinforced by nanoparticles under high-velocity

impact," *Thin-Walled Struct.*, vol. 127, pp. 446–458, June 2018, doi: 10.1016/j.tws.2018.02.010.

[52] W.-G. Jiang, S. R. Hallett, and M. R. Wisnom, "Development of Domain Superposition Technique for the Modelling of Woven Fabric Composites," in *Mechanical Response of Composites*, P. P. Camanho, C. G. Dávila, S. T. Pinho, and J. J. C. Remmers, Eds., Dordrecht: Springer Netherlands, 2008, pp. 281–291. doi: 10.1007/978-1-4020-8584-0_14.

[53] N. Rasin, A. B. Kueh, M. N. Mahat, and A. Y. Mohd Yassin, "Stability of triaxially woven fabric composites employing geometrically nonlinear plate model with volume segmentation ABD constitution," *J. Compos. Mater.*, vol. 50, no. 19, pp. 2719–2735, 2015, doi: 10.1177/0021998315612538.

[54] D. Chatterjee, A. Ghosh, and D. Chakravorty, "Finite element prediction of first-ply failure loads of composite thin skewed hypar shells using nonlinear strains," *Thin-Walled Struct.*, vol. 167, p. 108159, Oct. 2021, doi: 10.1016/j.tws.2021.108159.

[55] Z. W. Xu, Y. H. Chen, W. J. Cantwell, and Z. W. Guan, "Multiscale modelling of scaling effects in the impact response of plain woven composites," *Compos. Part B Eng.*, vol. 188, p. 107885, May 2020, doi: 10.1016/j.compositesb.2020.107885.

[56] H. Alshahrani and M. Hojjati, "Bending behavior of multilayered textile composite prepregs: Experiment and finite element modeling," *Mater. Des.*, vol. 124, pp. 211–224, June 2017, doi: 10.1016/j.matdes.2017.03.077.

[57] C. Hazelton, K. Gall, E. Abrahamson, M. Lake, and R. Denis, "Development of a Prototype Elastic Memory Composite STEM for Large Space Structures," in *44th AIAA/ASME/ASCE/AHS/ASC Structures, Structural Dynamics, and Materials Conference*, American Institute of Aeronautics and Astronautics. doi: 10.2514/6.2003-1977.

[58] S. Wang, S. Xu, L. Lu, and L. Sun, "Roll-Out Deployment Process Analysis of a Fiber Reinforced Polymer (FRP) Composite Tape-Spring Boom," *Polymers*, vol. 15, no. 11, Art. no. 11, Jan. 2023, doi: 10.3390/polym15112455.

[59] D. Tortorici, M. Sabatini, and S. Laurenzi, "Numerical simulations and experimental results of the deployment of thin-walled bistable composite booms," *Compos. Struct.*, vol. 327, p. 117669, Jan. 2024, doi: 10.1016/j.compstruct.2023.117669.

[60] S. Wang, S. Xu, L. Lu, and L. Sun, "Driving Force and Blossoming Analysis of a Composite Triangular Rollable and Collapsible (TRAC) Boom Used in Aerospace Technologies," *Aerospace*, vol. 11, no. 4, Art. no. 4, Apr. 2024, doi: 10.3390/aerospace11040311.

[61] S. Wang, Y. Gao, L. Huang, and L. Sun, "Deployment and Blossoming Analysis of a Fiber Reinforced Polymer (FRP) Collapsible Tubular Mast (CTM) Boom for Aerospace Applications," *Int. J. Aeronaut. Space Sci.*, vol. 25, no. 3, pp. 966–978, July 2024, doi: 10.1007/s42405-024-00714-8.

[62] K. A. Seffen and S. Pellegrino, "Deployment dynamics of tape springs," *Proc. R. Soc. Lond. Ser. Math. Phys. Eng. Sci.*, vol. 455, no. 1983, pp. 1003–1048, Mar. 1999, doi: 10.1098/rspa.1999.0347.

[63] K. A. Seffen, “Folding and deployment of curved tape springs,” *Int. J. Mech. Sci.*, 2000.

[64] J. C. H. Yee, O. Soykasap, and S. Pellegrino, “Carbon Fibre Reinforced Plastic Tape Springs,” in *45th AIAA/ASME/ASCE/AHS/ASC Structures, Structural Dynamics & Materials Conference*, Palm Springs, California: American Institute of Aeronautics and Astronautics, Apr. 2004. doi: 10.2514/6.2004-1819.

[65] M. Silver, J. Hinkle, and L. Peterson, “Controlled Displacement Snap-Through of Tape Springs: Modeling and Experiment,” in *46th AIAA/ASME/ASCE/AHS/ASC Structures, Structural Dynamics and Materials Conference*, Austin, Texas: American Institute of Aeronautics and Astronautics, Apr. 2005. doi: 10.2514/6.2005-2314.

[66] Y. Zuo, G. Jin, and P. Xie, “Calculative and experimental study of the CFRP tape spring,” *J. Mech. Sci. Technol.*, vol. 32, no. 8, pp. 3603–3609, Aug. 2018, doi: 10.1007/s12206-018-0711-x.

[67] T.-W. Liu, J.-B. Bai, and N. Fantuzzi, “New insights into folding tape-spring,” *Compos. Struct.*, vol. 341, p. 118225, Aug. 2024, doi: 10.1016/j.compstruct.2024.118225.

[68] C. Yang, B. Wang, S. Zhong, C. Zhao, and W. Liang, “On tailoring deployable mechanism of a bistable composite tape-spring structure,” *Compos. Commun.*, vol. 32, p. 101171, June 2022, doi: 10.1016/j.coco.2022.101171.

[69] H. Chen, B. Wang, X. Lin, K. A. Seffen, and S. Zhong, “Folding mechanics of a bistable composite tape-spring for flexible mechanical hinge,” *Int. J. Mech. Sci.*, vol. 272, p. 109188, June 2024, doi: 10.1016/j.ijmecsci.2024.109188.

[70] M. Franz, B. Schleich, and S. Wartzack, “Variation Analysis of Design Parameters of Fibre-Reinforced Plastic Parts,” *Proc. Des. Soc. Int. Conf. Eng. Des.*, vol. 1, no. 1, pp. 2725–2734, July 2019, doi: 10.1017/dsi.2019.279.

[71] K. Schulgasser, “Configuration of a Bent Tape of Curved Cross-Section,” *J. Appl. Mech.*, vol. 59, no. 3, pp. 692–693, Sept. 1992, doi: 10.1115/1.2893786.

[72] B. Wang, K. A. Seffen, and S. D. Guest, “Shape of a bistable composite tape-spring in folding,” in *AIAA Scitech 2019 Forum*, San Diego, California: American Institute of Aeronautics and Astronautics, Jan. 2019. doi: 10.2514/6.2019-2276.

[73] B. Wang, K. A. Seffen, and S. D. Guest, “Folded strains of a bistable composite tape-spring,” *Int. J. Solids Struct.*, vol. 233, p. 111221, Dec. 2021, doi: 10.1016/j.ijsolstr.2021.111221.

[74] M. E. Peterson and T. W. Murphey, “Large Deformation Bending of Thin Composite Tape Spring Laminates,” in *54th AIAA/ASME/ASCE/AHS/ASC Structures, Structural Dynamics, and Materials Conference*, Boston, Massachusetts: American Institute of Aeronautics and Astronautics, Apr. 2013. doi: 10.2514/6.2013-1667.

[75] E. Gamage, L. Weerasekara, U. Weerasinghe, S. Herath, C. Mallikarachchi, and H. Wijesuriya, “High-curvature Bending Response of Ultra-thin Woven Fibre Composites,” Aug. 2025.

[76] G. J. CURTIS, J. M. MILNE, and W. N. REYNOLDS, “Non-Hookean Behaviour of Strong Carbon Fibres,” *Nature*, vol. 220, no. 5171, pp. 1024–1025, Dec. 1968, doi: 10.1038/2201024a0.

[77] K. Ubamanyu and S. Pellegrino, “Nonlinear Behavior of IM7 Carbon Fibers in Compression Leads to Bending Nonlinearity of High-Strain Composites,” in *AIAA SCITECH 2023 Forum*, National Harbor, MD & Online: American Institute of Aeronautics and Astronautics, Jan. 2023. doi: 10.2514/6.2023-0580.

[78] J. D. H. Hughes, “Strength and modulus of current carbon fibres,” *Carbon*, vol. 24, no. 5, pp. 551–556, Jan. 1986, doi: 10.1016/0008-6223(86)90144-2.

[79] M. Kant and D. Penumadu, “Dynamic mechanical characterization for nonlinear behavior of single carbon fibers,” *Compos. Part Appl. Sci. Manuf.*, vol. 66, pp. 201–208, Nov. 2014, doi: 10.1016/j.compositesa.2014.07.019.

[80] “ABAQUS Analysis User’s Manual (v6.6).” Accessed: Sept. 15, 2025. [Online]. Available: https://classes.engineering.wustl.edu/2009/spring/mase5513/abaqus/docs/v6.6/books/usb/default.htm?startat=pt06ch23s06alm19.html#usb-elm-eusingshellgensect

[81] R. D. Adams and D. G. C. Bacon, “Effect of Fibre Orientation and Laminate Geometry on the Dynamic Properties of CFRP,” *J. Compos. Mater.*, vol. 7, no. 4, pp. 402–428, Oct. 1973, doi: 10.1177/002199837300700401.

[82] D. A. Saravanos and C. C. Chamis, “Mechanics of damping for fiber composite laminates including hygro-thermal effects,” E-5034, Apr. 1989. Accessed: Jan. 02, 2026. [Online]. Available: https://ntrs.nasa.gov/citations/19900000869

[83] H. Xiao *et al.*, “Shape Memory Polymer Composite Booms with Applications in Reel-Type Solar Arrays,” *Chin. J. Mech. Eng.*, vol. 36, no. 1, p. 67, May 2023, doi: 10.1186/s10033-023-00892-8.

[84] S. Laurenzi, D. Rufo, M. Sabatini, P. Gasbarri, and G. B. Palmerini, “Characterization of deployable ultrathin composite boom for microsatellites excited by attitude maneuvers,” *Compos. Struct.*, vol. 220, pp. 502–509, July 2019, doi: 10.1016/j.compstruct.2019.04.003.

[85] F. Quadrini, L. Iorio, L. Santo, C. Circi, E. Cavallini, and R. C. Pellegrini, “Smart Composite Booms for Solar Sails,” *J. Compos. Sci.*, vol. 7, no. 12, p. 495, Dec. 2023, doi: 10.3390/jcs7120495.

APPANDICES

Appendix – A: Section Block of the Input File Used to Call the UGENS Subroutine

```
** Section: Shell General

*Shell General Section, elset=Set-1, orientation=Ori-1,
density=2.7918e-07, USER, PROPERTIES=21, VARIABLES=52

0.2274

8493., 2195., 8493., 0., 0., 370., 0., 0.

0., 36.22, 0., 0., 0., 4.46, 36.5, 0.

0., 0., 0., 0., 1.8,

*TRANSVERSE SHEAR STIFFNESS

2954.33, 2954.33, 0

*End Instance

**
```

Appendix – B: UGENS Subroutine

```
    SUBROUTINE
UGENS(ddndde,force,statev,sse,spd,pnewdt,stran,dstran
,

  &
tss,time,dtime,temp,dtemp,predef,dpred,cename,ndi,nsh
r,nsecv,

  &
nstatv,props,jprops,nprops,njprop,coords,celent,thick
,dfgrd,curv,

  & basis,noel,npt,kstep,kinc,kit,linper)


   include 'aba_param.inc'


   character*80 cename

   dimension
force(nsecv),statev(nstatv),ddndde(nsecv,nsecv),

  & stran(nsecv),dstran(nsecv),predef(*),dpred(*),

  & props(*),jprops(*),coords(3),time(2),dfgrd(3,3),

  & curv(2,2),basis(3,3),tss(*)

   dimension eD1(181)

  dimension D11STIF(181)

  dimension D12STIF(181)

   dimension STIF(181,6,6),e(181,6,6)

   integer
i,ii_4,ii_5,j,jj,kk,m,k,n,current_Id_4,current_Id_5,i
j,gg

  double precision w4,w5,dk4,dk5

   double precision D11_4,D11_5,D12_4,D12_5,D12_avg

   integer prev_Id_4, prev_Id_5
```

```
    double precision stranCurrent_4,stranCurrent_5
    double precision wstrain

! Pre-defined curvature points
      eD1=(/0.000, 0.001, 0.002, 0.003, 0.004, 0.005,
  0.006, 0.007,
  + 0.008, 0.009, 0.010, 0.011, 0.012, 0.013, 0.014,
  0.015, 0.016,
  + 0.017, 0.018, 0.019, 0.020, 0.021, 0.022, 0.023,
  0.024, 0.025,
  + 0.026, 0.027, 0.028, 0.029, 0.030, 0.031, 0.032,
  0.033, 0.034,
  + 0.035, 0.036, 0.037, 0.038, 0.039, 0.040, 0.041,
  0.042, 0.043,
  + 0.044, 0.045, 0.046, 0.047, 0.048, 0.049, 0.050,
  0.051, 0.052,
  + 0.053, 0.054, 0.055, 0.056, 0.057, 0.058, 0.059,
  0.060, 0.061,
  + 0.062, 0.063, 0.064, 0.065, 0.066, 0.067, 0.068,
  0.069, 0.070,
  + 0.071, 0.072, 0.073, 0.074, 0.075, 0.076, 0.077,
  0.078, 0.079,
  + 0.080, 0.081, 0.082, 0.083, 0.084, 0.085, 0.086,
  0.087, 0.088,
  + 0.089, 0.090, 0.091, 0.092, 0.093, 0.094, 0.095,
  0.096, 0.097,
  + 0.098, 0.099, 0.100, 0.101, 0.102, 0.103, 0.104,
  0.105, 0.106,
  + 0.107, 0.108, 0.109, 0.110, 0.111, 0.112, 0.113,
  0.114, 0.115,
  + 0.116, 0.117, 0.118, 0.119, 0.120, 0.121, 0.122,
  0.123, 0.124,
  + 0.125, 0.126, 0.127, 0.128, 0.129, 0.130, 0.131,
  0.132, 0.133,
```

```
  + 0.134, 0.135, 0.136, 0.137, 0.138, 0.139, 0.140,
0.141, 0.142,

  + 0.143, 0.144, 0.145, 0.146, 0.147, 0.148, 0.149,
0.150, 0.151,

  + 0.152, 0.153, 0.154, 0.155, 0.156, 0.157, 0.158,
0.159, 0.160,

  + 0.161, 0.162, 0.163, 0.164, 0.165, 0.166, 0.167,
0.168, 0.169,

  + 0.170, 0.171, 0.172, 0.173, 0.174, 0.175, 0.176,
0.177, 0.178,

  + 0.179, 0.180 /)



! State variable definition

   statev(1)=noel;   statev(2)=npt;   statev(3)=kstep;
statev(4)=kinc;

   statev(5)=kit;                    statev(6)=time(1);
statev(7)=dtime;statev(8)=thick;

   statev(9)=celent;                     statev(10)=temp;
statev(11)=dtemp;

   statev(12)=zero; statev(13)=zero



   k3=0

   do k1=1,3

    do k2=1,3

     statev(14+k3)=basis(k1,k2)

     statev(23+k3)=dfgrd(k1,k2)

     k3=k3+1

    end do

   end do

   statev(32)=curv(1,1);          statev(33)=curv(1,2);
statev(34)=curv(2,1)
```

```
   statev(35)=curv(2,2);            statev(36)=tss(1);
statev(37)=tss(2)

   statev(38)=coords(1);         statev(39)=coords(2);
statev(40)=coords(3)

   do k1=1,nsecv

    statev(40+k1)=stran(k1)

   end do

    istatev=40+nsecv


! Jacobian definition (ddndde means derivative)

   ddndde(1,1) = props(1)

   ddndde(1,2) = props(2)

   ddndde(2,2) = props(3)

   ddndde(1,3) = props(4)

   ddndde(2,3) = props(5)

   ddndde(3,3) = props(6)

   ddndde(1,4) = props(7)

   ddndde(2,4) = props(8)

   ddndde(3,4) = props(9)

   ddndde(4,4) = props(10)

   ddndde(1,5) = props(11)

   ddndde(2,5) = props(12)

   ddndde(3,5) = props(13)

   ddndde(4,5) = props(14)

   ddndde(5,5) = props(15)

   ddndde(1,6) = props(16)

   ddndde(2,6) = props(17)

   ddndde(3,6) = props(18)
```

```
      ddndde(4,6) = props(19)

      ddndde(5,6) = props(20)

      ddndde(6,6) = props(21)


      do i=1,nsecv

       do j=1,i

         ddndde(i,j) = ddndde(j,i)

       end do

      end do


! Initializing stiffness and strain arrays

      do ii=1,181

       do jj=1,6

        do kk=1,6

           STIF(ii,jj,kk)= 0

           e(ii,jj,kk)= 0

        end do

       end do

      end do


! Assemble stiffness 3D array

      do m=2,182

       STIF(m-1,1,1) = 8.493e+03

      STIF(m-1,1,2) = 2.195e+03

      STIF(m-1,1,3) = 0

      STIF(m-1,1,4) = 0

      STIF(m-1,1,5) = 0
```

```
STIF(m-1,1,6) = 0
STIF(m-1,2,1) = 2.195e+03
STIF(m-1,2,2) = 8.493e+03
STIF(m-1,2,3) = 0
STIF(m-1,2,4) = 0
STIF(m-1,2,5) = 0
STIF(m-1,2,6) = 0
STIF(m-1,3,1) = 0
 STIF(m-1,3,2) = 0
 STIF(m-1,3,3) = 0.370e+03
 STIF(m-1,3,4) = 0
 STIF(m-1,3,5) = 0
 STIF(m-1,3,6) = 0
 STIF(m-1,4,1) = 0
 STIF(m-1,4,2) = 0
 STIF(m-1,4,3) = 0
 STIF(m-1,4,4) = 36.220
STIF(m-1,4,5) = 4.460
 STIF(m-1,4,6) = 0
 STIF(m-1,5,1) = 0
 STIF(m-1,5,2) = 0
STIF(m-1,5,3) = 0
STIF(m-1,5,4) = 4.460
STIF(m-1,5,5) = 36.220
STIF(m-1,5,6) = 0
STIF(m-1,6,1) = 0
STIF(m-1,6,2) = 0
```

```
    STIF(m-1,6,3) = 0

    STIF(m-1,6,4) = 0

    STIF(m-1,6,5) = 0

    STIF(m-1,6,6) = 0.180e+01

   end do


!Stiffness array for D11 and D12

   D11STIF=(/ 36.220, 36.273, 36.326, 36.379, 36.432,
 36.485, 36.538, 36.591,

  &     36.644, 36.697, 36.750, 36.802, 36.854, 36.906,
 36.958, 37.010,

  &     37.062, 37.114, 37.166, 37.218, 37.270, 37.259,
 37.248, 37.237,

  &     37.226, 37.215, 37.204, 37.193, 37.182, 37.171,
 37.160, 37.035,

  &     36.910, 36.785, 36.660, 36.535, 36.410, 36.285,
 36.160, 36.035,

  &     35.910, 35.735, 35.560, 35.385, 35.210, 35.035,
 34.860, 34.685,

  &     34.510, 34.335, 34.160, 33.965, 33.770, 33.575,
 33.380, 33.185,

  &     32.990, 32.795, 32.600, 32.405, 32.210, 32.014,
 31.818, 31.622,

  &     31.426, 31.230, 31.034, 30.838, 30.642, 30.446,
 30.250, 30.064,

  &     29.878, 29.692, 29.506, 29.320, 29.134, 28.948,
 28.762, 28.576,

  &     28.390, 28.209, 28.028, 27.847, 27.666, 27.485,
 27.304, 27.123,

  &     26.942, 26.761, 26.580, 26.420, 26.260, 26.100,
 25.940, 25.780,

  &     25.620, 25.460, 25.300, 25.140, 24.980, 24.830,
 24.680, 24.530,
```

```
  &     24.380, 24.230, 24.080, 23.930, 23.780, 23.630,
23.480, 23.340,
  &     23.200, 23.060, 22.920, 22.780, 22.640, 22.500,
22.360, 22.220,
  &     22.080, 21.949, 21.818, 21.687, 21.556, 21.425,
21.294, 21.163,
  &     21.032, 20.901, 20.770, 20.647, 20.524, 20.401,
20.278, 20.155,
  &     20.032, 19.909, 19.786, 19.663, 19.540, 19.428,
19.316, 19.204,
  &     19.092, 18.980, 18.868, 18.756, 18.644, 18.532,
18.420, 18.308,
  &     18.196, 18.084, 17.972, 17.860, 17.748, 17.636,
17.524, 17.412,
  &     17.300, 17.216, 17.132, 17.048, 16.964, 16.880,
16.796, 16.712,
  &     16.628, 16.544, 16.460, 16.385, 16.310, 16.235,
16.160, 16.085,
  &      16.010, 15.935, 15.860, 15.785, 15.710 /)


  D12STIF=(/ 4.460, 4.433, 4.406, 4.379, 4.352, 4.325,
4.298, 4.271,
  &    4.244, 4.217, 4.190, 4.135, 4.080, 4.025, 3.970,
3.915,
  &    3.860, 3.805, 3.750, 3.695, 3.640, 3.577, 3.514,
3.451,
  &    3.388, 3.325, 3.262, 3.199, 3.136, 3.073, 3.010,
2.943,
  &    2.876, 2.809, 2.742, 2.675, 2.608, 2.541, 2.474,
2.407,
  &    2.340, 2.284, 2.228, 2.172, 2.116, 2.060, 2.004,
1.948,
  &    1.892, 1.836, 1.780, 1.739, 1.698, 1.657, 1.616,
1.575,
```

```
  &    1.534, 1.493, 1.452, 1.411, 1.370, 1.339, 1.308,
1.277,
  &    1.246, 1.215, 1.184, 1.153, 1.122, 1.091, 1.060,
1.044,
  &    1.028, 1.012, 0.996, 0.980, 0.964, 0.948, 0.932,
0.916,
  &    0.900, 0.889, 0.878, 0.867, 0.856, 0.845, 0.834,
0.823,
  &    0.812, 0.801, 0.790, 0.781, 0.772, 0.763, 0.754,
0.745,
  &    0.736, 0.727, 0.718, 0.709, 0.700, 0.692, 0.684,
0.676,
  &    0.668, 0.660, 0.652, 0.644, 0.636, 0.628, 0.620,
0.614,
  &    0.608, 0.602, 0.596, 0.590, 0.584, 0.578, 0.572,
0.566,
  &    0.560, 0.556, 0.552, 0.548, 0.544, 0.540, 0.536,
0.532,
  &    0.528, 0.524, 0.520, 0.516, 0.512, 0.508, 0.504,
0.500,
  &    0.496, 0.492, 0.488, 0.484, 0.480, 0.476, 0.472,
0.468,
  &    0.464, 0.460, 0.456, 0.452, 0.448, 0.444, 0.440,
0.438,
  &    0.436, 0.434, 0.432, 0.430, 0.428, 0.426, 0.424,
0.422,
  &    0.420, 0.417, 0.414, 0.411, 0.408, 0.405, 0.402,
0.399,
  &    0.396, 0.393, 0.390, 0.390, 0.390, 0.390, 0.390,
0.390,
  &     0.390, 0.390, 0.390, 0.390, 0.390 /)


! Assemble strain 3D array
```

```
    do m=2,182
     e(m-1,4,4)=eD1(m)
     e(m-1,4,5)=eD1(m)
     e(m-1,5,5)=eD1(m)
     e(m-1,5,4)=eD1(m)
    end do

!Finding the current strain IDs for K4
    stranCurrent_4 = abs(stran(4))
    ii_4 = 1
    do
        if (ii_4 <= size(e,1)) then
            if (StranCurrent_4 == 0.0) then
                current_Id_4 = 1
                exit
            elseif (StranCurrent_4 <= e(ii_4,4,4)) then
                current_Id_4 = ii_4
                exit
            else
                ii_4 = ii_4 + 1
         endif
        else
          print *, "No valid current_strain index found
 within bounds."
            current_Id_4 = size(e,1)
          exit
        endif
    end do
```

```
!Finding the current strain IDs for K5
    stranCurrent_5 = abs(stran(5))
    ii_5 = 1
    do
       if (ii_5 <= size(e,1)) then
            if (StranCurrent_5 == 0.0) then
                current_Id_5 = 1
                exit
            elseif (StranCurrent_5 <= e(ii_5,4,4)) then
                current_Id_5 = ii_5
                exit
            else
                ii_5 = ii_5 + 1
         endif
        else
          print *, "No valid current_strain index found
 within bounds."
            current_Id_5 = size(e,1)
          exit
        endif
    end do


!Guard next indices within table bounds
    if (current_Id_4 .le. 1.d0) then
       prev_Id_4 = current_Id_4
    else
```

```
   prev_Id_4 = current_Id_4 - 1
endif

if (current_Id_5 .le. 1.d0) then
   prev_Id_5 = current_Id_5
else
   prev_Id_5 = current_Id_5 - 1
endif

dk4 = eD1(current_Id_4) - eD1(prev_Id_4)
dk5 = eD1(current_Id_5) - eD1(prev_Id_5)

if (dk4 .le. 0.d0) then
   w4 = 0.d0
else
   w4 = (stranCurrent_4 - eD1(prev_Id_4)) / dk4
   if (w4 .lt. 0.d0) w4 = 0.d0 ! not really usefull
   if (w4 .gt. 1.d0) w4 = 1.d0
endif

if (dk5 .le. 0.d0) then
   w5 = 0.d0
else
   w5 = (stranCurrent_5 - eD1(prev_Id_5)) / dk5
   if (w5 .lt. 0.d0) w5 = 0.d0 ! not really usefull
   if (w5 .gt. 1.d0) w5 = 1.d0
endif
```

```
!Interpolated stiffnesses (avoid jumps)

   D11_4      =      (1.d0-w4)*D11STIF(prev_Id_4)      +
 w4*D11STIF(current_Id_4)

   D12_4      =      (1.d0-w4)*D12STIF(prev_Id_4)      +
 w4*D12STIF(current_Id_4)

   D11_5      =      (1.d0-w5)*D11STIF(prev_Id_5)      +
 w5*D11STIF(current_Id_5)

   D12_5      =      (1.d0-w5)*D12STIF(prev_Id_5)      +
 w5*D12STIF(current_Id_5)

  D12_avg = (D12_4+D12_5)/2


!Clip to small positive to avoid singular pivots

   if (D11_4 .lt. 1.d-12) D11_4 = 1.d-12 ! not really
 usefull

   if (D11_5 .lt. 1.d-12) D11_5 = 1.d-12 ! not really
 usefull


  ! M1 = [D11(K1)]*K1 + [D12(K2)]*K2

  ! M2 = [D11(K2)]*K2 + [D12(K1)]*K1


   do i=1,6

    do j=1,6

      if (i==4 .and. j==4) then

           force(i) = force(i)+D11_4*dstran(j)

         ddndde(i,j) = D11_4

      elseif (i==5 .and. j==5) then

           force(i) = force(i)+D11_5*dstran(j)

         ddndde(i,j) = D11_5
```

```
        elseif (i==4 .and. j==5) then

             force(i) = force(i)+D12_avg*dstran(j)
           ddndde(i,j) = D12_avg
        elseif (i==5 .and. j==4) then

             force(i) = force(i)+D12_avg*dstran(j)
           ddndde(i,j) = D12_avg
     else
             force(i) = force(i)+STIF(1,i,j)*dstran(j)
        endif


      end do
      statev(istatev+i) = force(i)
     end do


 !Calculations for enegry terms
    wstrain = 0.0d0
    do i = 1, nsecv
    wstrain = wstrain + 0.5d0 * force(i) * stran(i)
    end do
    sse = wstrain


     RETURN
     END
```